MOCVD Growth of III-V Compounds for Long Wavelength Optoelectronic Devices

Zhu Jingyi

School of Electrical & Electronic Engineering

A thesis submitted to the Nanyang Technological University
in fulfillment of the requirement for the degree of
Master of Engineering

2005

Statement of Originality

I hereby certify that the work embodied in this thesis is the result of original research and has not been submitted for a higher degree to any other University or Institution.

Date	Zhu Jingyi

Acknowledgements

I would like to express my deepest gratitude and heartfelt appreciation to my supervisor, Dr. Tang Xiaohong, who has given me lots of valuable guidance and encouragement throughout the project. He can easily follow the frontier in research with an excellent sense of direction. Dr. Tang is earnest and strict in academic activities, while warmhearted in life. I am very grateful to him for his continued encouragement and suggestion in the successful completion of my research project.

Many thanks to Dr Yu Guangyou, Dr Zhang Baolin, who provides expert technical support and discussion in epitaxy growth of samples and the samples' characterization.

I also acknowledge technicians in Photonics Research Center of School of Electrical and Electronic Engineering, NTU, for their hospitality and assistance. Their kindness and help contributed much to the smooth progress of the project.

Finally, I would like to thank my family especially my wife, Chen Wenjia, and my daughter, Zhu Yueming. It is because of their love, support and encouragement, I can concentrate on my research and finish the project smoothly.

I am ready to thank everyone here, who together makes a kind of environment full of friendship and kindness, which has given me a lot other than research.

Summary

Metal-Organic Chemical Vapour Deposition (MOCVD) growth of InP based III-V semiconductor materials for long-wavelength semiconductor lasers have been studied in detail. With tertiarybutylarsine (TBAs) and tertiarybutylphosphine (TBP) as group V precursors and N_2 as carrier gas, high quality InP based III-V semiconductor alloys and quantum well (QW) structures have been grown by using MOCVD technology. InP/InP, InGaAs/InP, InGaAsP/InP bulk layers and InGaAs/InP multiple quantum wells (MQW) have been successfully grown. The crystal quality and optical properties of the samples have been investigated. For an unintentionally doped InP epilayer, electron mobility of 10400 V/cm^2•s has been measured at 77 K. InP epilayers grown on Fe-doped InP substrate have been studied at different growth temperatures. The relationship between SiH_4 dopant source flow and the carrier concentration of Si-doped InP epilayer has been obtained. High Zn diffusion properties in Zn-doped InP epitaxial layer have been investigated. Lattice matched InGaAs epitaxial layer grown on InP substrate has been studied in detail. The correlation between the lattice mismatch of InGaAs to InP and the TMGa/(TMGa+TMIn) ratio in vapour phase during MOCVD growth has been explored.

Composition control of $In_{1-x}Ga_xAs_yP_{1-y}$ quaternary alloys during MOCVD growths has been investigated. The Ga composition (x) of the alloys has been found to change linearly with the TMGa/(TMGa+TMIn) source flow ratio in the MOCVD growth. The phosphorus content (1-y) of the $In_{1-x}Ga_xAs_yP_{1-y}$ alloys is related to TBAs/TBP gas phase ratio. It has demonstrated that the segregation coefficient of

As decreases with increasing TBAs/(TBAs+TBP) source flow ratio during the MOCVD growth. The energy bandgap of $In_{1-x}Ga_xAs_yP_{1-y}$ alloys is found to be mainly dependent on the TBAs/(TBAs+TBP) flow ratio, while both TMGa/(TMGa+TMIn) and TBAs/(TBAs+TBP) flow ratios affect the lattice constants of the $In_{1-x}Ga_xAs_yP_{1-y}$ quaternary alloys growth. Low dimensional InGaAs/InP MQW has been successfully grown. X-ray diffraction and photoluminescence have been employed to characterize the crystal quality and optical properties of the structure. The results show that the good quality of the structure.

Table of Contents

List of Figures

List of tables

Chapter 1 Introduction

1.1 Motivation

III-V semiconductor alloys are useful materials for both heterojunction microwave electronic devices and optoelectronic devices applications [1-5]. Their large mobility and high drift saturation velocity make them very promising in high frequency field-effect transistors (FET). The high efficiency of optical emission makes these materials very important in optical fiber communication, satellite transmission, Radar linkage, direct satellite broadcasting, super computers and high speed signal processing.

Over last 40 years, the market of compound semiconductor based devices has continued to expand and mature. Much of the commercial promise of the late 1980s for these materials has been realized. Many devices [6-9], including light emitting diodes (LED), laser diodes (LD), solar cells, high electron mobility transistors (HEMT) and heterojunction bipolar transistors (HBT), etc. have now reached the stage of significant manufacturing volumes.

Today, long wavelength (1.3μm or 1.55μm) lasers incorporating strained InGaAs or InGaAsP quantum wells in the active region have been proven to exhibit improved laser characteristics including low threshold currents, high output power and good temperature performance [10]. Quaternary alloy structures are preferable from a design point of view, because they allow varying the quantum well thickness and thus the optical confinement while maintaining a constant emission wavelength. Motivated by low fiber absorption and dispersion in the wavelength range of 1μm to 1.65 μm, InGaAsP alloy based electro-optical devices have become widely used. This drives significant researches on the epitaxy growth technology of InP and the related compounds. Metalorganic chemical vapour deposition (MOCVD) growth technique has given a new insight into the physics of materials science. It has several advantages compared to other epitaxial processes, such as LPE, VPE and MBE, etc., in growing semiconductor heterostructures. MOCVD has established itself as a unique and important epitaxial growth technique both for scientific researches and industry production. In MOCVD epitaxial growth, high quality low dimensional structures (LDS) for fundamental semiconductor physics research and useful device structures are grown by introducing metered group III alkyls and group V hydrides (or alkyls) into a quartz tube that contains a substrate placed on a lamp heated (or RF heated) graphite susceptor. This technique is attractive with its ability to grow pure uniform layers with low background doping density, sharp interface between heterojunctions, and in its high capacity and short shut-down time which are very important for commercial production. MOCVD can prepare multilayer structures with thickness as thin as few atomic layers.

In MOCVD growth, the main concern is the extremely high toxicity of the group V sources used in the process, such as arsine and phosphine (AsH_3 and PH_3). Highly toxic materials are obviously undesirable, while a high vapour pressure of arsine and phosphine increases the risk of wide spreading of the compound in case of an accidental leak. Associated with these properties are the high cost of gas sources' storage, process safety monitoring and waste treatment, along with environmental concerns. More researches have gone into investigating alternative group-V sources as substitutes for the traditional group-V precursors, arsine and phosphine (AsH_3 and PH_3).

According to several studies [11][12], the acute toxicity of As- and P-hydrides is directly linked to the number of As-H and P-H bonds in the source molecules. Substituting one H-function in the molecule by an organic alkyl (e.g. methyl, tertiarybutyl) reduces the toxicity and the vapour pressure of the compound by about one order of magnitude.

The most successful alternatives to the hydrides AsH_3 and PH_3 are tertiarybutylarsine (TBAs) and tertiarybutylphosphine (TBP). TBAs and TBP are less toxic than AsH_3 and PH_3, and both the organic precursors decompose at much lower temperatures than AsH_3 and PH_3, permitting the use of lower substrate temperatures and V/III ratios in MOCVD growth. The higher efficiency of TBAs and TBP reduces the amount of source material required, cuts the amount of As and P in the pumping system (thereby increasing reactor uptime), and also reduces the amount of waste material produced. The liquid form at room temperature makes TBAs and TBP sources easy to install and transport.

Based on above considerations, TBAs and TBP, were used as group-V sources for the MOCVD growth in this project. Nitrogen gas was used as the carrier gas instead of normally used hydrogen gas in this project to improve the safety further in MOCVD growth. With the safer and advanced configuration, MOCVD growths of InP based III-V semiconductor alloys and quantum well structures for long wavelength optoelectronic devices applications have been investigated in details.

1.2 Objectives

The objectives of this project are:

- to develop MOCVD of InP based materials by using TBAs and TBP and optimize the InP based growth conditions,
- to study the doping properties of InP bulk layer,
- to explore the relationship between the composition of InGaAs grown layer and the input vapour phase ratio TMGa/(TMGa+TMIn) in MOCVD growth,

- to study the structural and optical properties of $In_{1-x}Ga_xAs$ using X-ray diffraction (XRD), photoluminescence (PL) and Raman spectroscopy,
- to investigate the correlation of $In_{1-x}Ga_xAs_yP_{1-y}$ epitaxial layer's composition versus vapour phase input ratio of TBAs/(TBAs+TBP) and TMGa/(TMGa+TMIn) in MOCVD growth,
- to grow InGaAs/InP quantum well structure, and perform the optical and crystallographic characterization on the epitaxial structures using PL, XRD, and Scanning electron microscopy (SEM).

1.3 Major contribution of the thesis

The thesis is concerned primarily on the MOCVD growth and characterization of InP based materials for long wavelength semiconductor optoelectronic device applications. The major contributions of this thesis are outlined below:

- High quality single-layer InP/InP has been grown by using MOCVD growth with TBP as group-V precursor in nitrogen ambient. Quality of the InP epitaxial layer was characterized by photoluminescence (PL), Electrochemical CV profiling (ECV), Hall measurements, and XRD.
- Lattice-matched ternary InGaAs/InP with good quality was grown with TBAs as group V source. The Ga incorporation in the InGaAs epitaxy growth was studied in detail.
- InGaAsP/InP quaternary layers have also been grown. Relationships between the solid compositions of the epitaxy layers and input vapour source flow ratio (TBAs/(TBAs+TBP) and TMGa/(TMGa+TMIn)) in MOCVD growth have been investigated.

- Low dimensional structure InGaAs/InP MQW targeted at the emission wavelength of 1.55μm has been grown. SEM, PL and XRD characterization also shows that the MQW structure has good interface and crystal quality.

1.4 Organization of this thesis

This thesis is organized as follows: it starts with a brief survey on InP related compound and MOCVD growth in Chapter 1; Chapter 2 provides an overview of the materials and the epitaxy growth techniques used for long wavelength semiconductor optoelectronic devices fabrication; Introduction of MOCVD technology in principle together with system description and material characterization are given in Chapter 3; Chapter 4 discusses the MOCVD growth of bulk-InP alloy and the grown layer's characterization; doping in InP alloy has also been investigated. Chapter 5 describes the InGaAs ternary material and its characterization. Correlation of InGaAsP composition and the group III as well as group V source flow ratio in MOCVD growth has been explored in Chapter 6. Chapter 7 introduces MQW growth and characterization. Finally, the conclusions and some suggestions for future work in this research are given in Chapter 8.

Chapter 2 Background

2.1 Introduction

The progress in InP material based long wavelength devices is fostered by an explosive increase of the needs for telecommunications bandwidth. On the Internet and telephone highways, which are built from optical fibers, the information travels as digital data at ever-higher speeds and in ever-larger quantities, such as transmission requirement of the vocal and textural information. The technology of the light emitting and detecting semiconductor devices involves epitaxy growth on InP substrates as a critical and strategic step. As a key semiconductor for production of optoelectronic and photonic devices, InP based materials have been increasing exponentially in the past few years. In particular, InP based materials such as InGaAsP alloy have been realized as very important materials for communication in the 1.3 μm and 1.55 μm spectral regions. The applications of InP based materials have been extended to other areas including laser diodes, light emitting diodes, photodetectors, waveguides, photocathodes and solar cells.

Epitaxy growth of InP alloys on InP substrate is important in applications in [1-10]: a) discrete light emitters (long wavelength vertical cavity surface emitting lasers (VCSEL)), laser arrays, semiconductor optical amplifiers, modulators and photo-detectors for optical fiber communications, b) Ultra-high frequency (UHF) microelectronics (>20 GHz), c) optoelectronic integrated circuits (OEICs), d) photonic integrated circuits (PICs) which are generally a monolithic combination of active and passive (waveguide, filters) devices on InP. e) photocathodes, f) solar cells, and g) other transducers, etc. The list of useful epitaxial layer compositions is all InP related materials, among these, InGaAsP/InP material plays an important role in long wavelength devices in telecommunications.

2.2 InGaAsP/InP for long wavelength optoelectronics

InP is one of the oldest III-V compounds investigated. Its energy bandgap is shown as in Figure 2.1. Thiel and Koelsch synthesized it in 1910 [11]. InP single crystal substrate did not become available until after applying of the Liquid Encapsulated Czochralski (LEC) process to III-V compounds by Mullin et al in 1968[12]. With further development of growth technology, extremely high-pure InP was grown [13] and exhibited a background carrier concentration as low as 3 x 10^{13} cm^{-3} with a Hall mobility of 6000 cm^2 /Vs at 300 K and 200 000 cm^2 /Vs at 50 K.

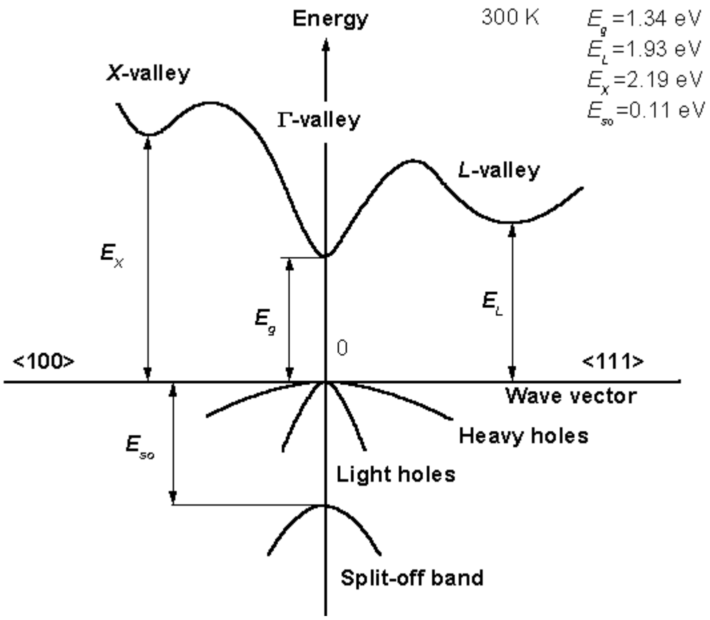

Figure 2.1: Energy bandgap of InP @ 300K

The application of single InP material in optoelectronics is limited by the constant energy bandgap (1.35eV). Fortunately, the emission wavelengths from InP based $In_{1-x}Ga_xAs$ ternary and $In_{1-x}Ga_xAs_yP_{1-y}$ quaternary alloys can be tuned by changing their compositions from 0.9 µm to 1.65 µm. Figure 2.2 shows the bandgap and lattice constants of GaAs, GaP, InAs, and InP binaries which bound the InGaAsP quaternary system. The bandgap and lattice constant of $In_{1-x}Ga_xAs_yP_{1-y}$ alloy can be adjusted independently by tuning its x and y compositions. This property allows one to grow the $In_{1-x}Ga_xAs_yP_{1-y}$ alloys with different energy bandgap while keep its lattice constant matched to InP substrate. Therefore, the one to one relationship between the energy bandgap of epitaxial layer and its lattice constant, a major obstacle to device quality crystal growth, can be avoided.

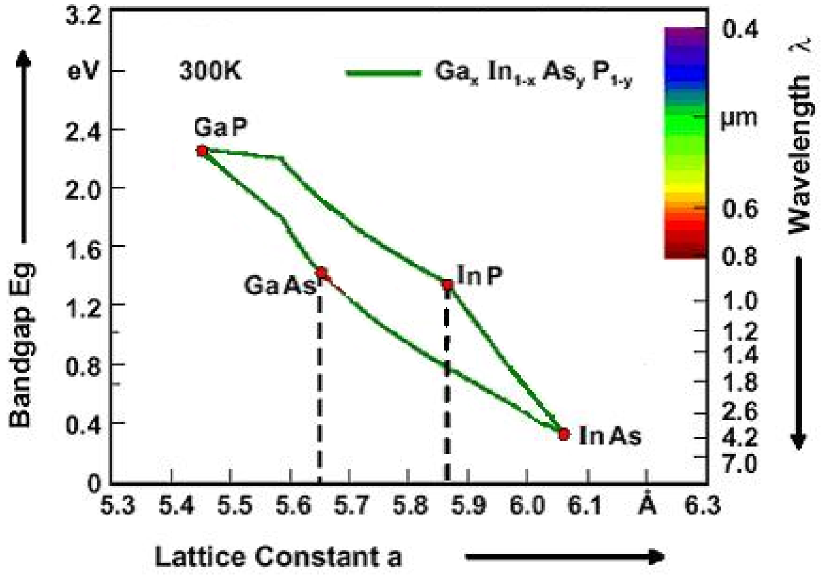

Figure 2.2: Variation of the energy bandgap as a function of lattice constant for some III-V binaries and their alloy semiconductors

With lattice constant matched to InP substrate [11], bandgap energies of $In_{1-x}Ga_xAs_yP_{1-y}$ alloy span from 0.75eV to 1.35eV, which covers the emission wavelength range needed for advanced optical communication system.

Preparation of the lattice matched InGaAsP/InP heterojunctions was reported for the first time in 1972 [14]. The first commercial device, which incorporated an InGaAsP photocathode, was introduced in 1973 [15]. In the beginning, double heterojunction (DH) structures (shown in Figure 2.3) were widely used to fabricate the light emission devices, such as laser diodes and light emitting diodes. Although the DH structure can increase the carrier confinement and improve the device performance effectively, for some special applications such devices still cannot meet the requirement.

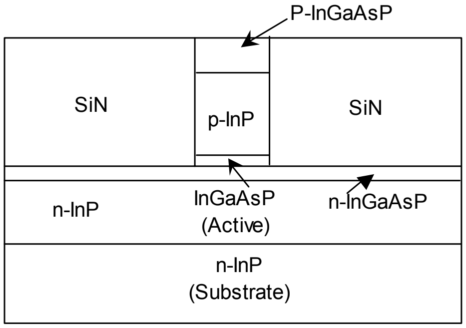

Figure 2.3: Schematic diagram of the cross section of a DH-InGaAsP laser diode.

Reduction in the dimensionality of a material system to the size of the order of Bohr radius of electron and hole pairs results in quantum size effects. For example, the band-to band transition energy of the semiconductor is increased and the density of states distribution in the structure is narrowed down from the bulk material [16]. Using low dimensional structure as the active region in a semiconductor laser diode structure will get shorter lasing wavelength, significantly lower its threshold current densities, and make the threshold current of the device less temperature-dependent. The gain distribution for lasing gets progressively narrower as the dimensionality of the active layer of a laser diode structure progress from bulk (3D) to quantum well (2D), quantum wire (1D) and quantum box (0D).

A revolution occurred in the area of III-V compound semiconductor caused by the rapid development of epitaxy growth technology, mainly molecular beam epitaxy (MBE) and MOCVD, with the ability to grow structures with very abrupt interfaces and accurate thickness, composition and doping uniformity control. Devices with complex low dimensional structures such as quantum wells can be realized by using these technologies.

2.3 Comparison of epitaxial growth techniques

2.3.1 Introduction

The word “epitaxy” is derived from the ancient Greek words “epi,” meaning “on”, and “taxis,” meaning “arrangement”. Thus, an epitaxial layer is one that takes the same crystal structure as that of the substrate it is deposited on, the same crystal symmetry and lattice constant.

There are three important epitaxy growth technologies widely used today for InP and its alloys epitaxial growth, namely liquid-phase epitaxy (LPE), molecular-beam epitaxy (MBE) and metal organic chemical vapour deposition (MOCVD). All these three techniques can produce a wide range of very high-purity semiconductor materials with excellent optical and electrical properties. This makes it possible to fabricate the devices with novel structures such as quantum wells (QW) or even quantum dots (QDs).

2.3.2 Liquid-Phase Epitaxy (LPE)

LPE is an equilibrium epitaxy growth technique, and the thermodynamics of the epitaxy process are very well understood. It utilizes simple equipment, and can achieve high purity grown films easily because of the stoichiometric control that results from the depositing from a saturated melt [17]. For InP epitaxy growth, the solution is from In-rich melt. Defects such as In vacancies and P atoms on In sites (the P antisite) are virtually nonexistent in LPE growth of InP material.

Liquid-Phase Epitaxy was used for most of early researches on InP materials. And it is still widely used to produce LEDs and lasers with simple epilayer structures. But it is not suitable for lower dimensional structure growth, such as for growing quantum well structures, because it is very difficult to obtain a sharp interface and thinner layers by using LPE growth.

2.3.3 Molecular-Beam Epitaxy (MBE)

In MBE growth, the grown material elements, e.g. Ga, In, etc, evaporate from effusion cells (ovens) in a high vacuum chamber in the form of molecular beams onto a heated substrate to get the epitaxy growth done. Since the process takes place in an ultrahigh vacuum (UHV) environment, the beams are not scattered, and the background contamination in the epitaxy film is reduced to a very low level. The most important advantage of MBE is the ability to access the growing layers with a variety of diagnostic tools, such as reflection high-energy electron diffraction (RHEED), Auger spectrum, etc. They can be used to control the growth process to define the layer thickness and composition. Another important feature is that growth rates are typically on the order of a few Å/s and the beams can be shuttered in a fraction of a second, allowing for nearly atomically abrupt transitions from one material to another.

High cost for UHV apparatus and frequent maintenance of the system make MBE technology difficult for commercial applications. Because of low growth rate, MBE is not suitable for thick layer growth.

2.3.4 Metalorganic Chemical Vapour Deposition (MOCVD)

Manasevit [18] pioneered the initial use of MOCVD in 1968 and reported the first-hand account of the early days of MOCVD. The development of MOCVD growth was primarily driven by limitations in early growth techniques, such as LPE and VPE. LPE was successfully used to fabricate many novel devices, but the problems of scaling up this technique to produce uniform films on large area substrates was never completely overcome. While chloride and hydride VPE has made many strides for Ga (As, P) device structures, there are fundamental problems in producing the AlGaAs layers needed for lasers and other heterojunction devices, because aluminum reacts vigorously with HCl, which usually act as group III carrier in VPE growth, and form aluminum chloride which are very difficult to be pyrolyzed. It was until 1977, when Dupuis and Dapkus [19] reported the achievement of room temperature lasers prepared by MOCVD, this technique was finally considered to be capable of filling its early promise.

In MOCVD process, compounds of the desired materials (metalorganics, hydrides, etc.) are transported to a heated substrate, where a chemical reaction takes place on the substrate surface and the epitaxy growth starts. MOCVD growth is usually conducted at a pressure between 20 mbar and atmospheric pressure. The equipment is generally quite simple, especially for atmospheric growth. The chemistry of MOCVD is much more complex than that in MBE growth, although reactions can be accurately controlled by the correct selection of precursors, operating conditions, and reactor design.

MOCVD is a very versatile technique and has been used to deposit materials that are difficult to grow by MBE, such as phosphides and nitrides. Due to the necessity of decomposing the precursor materials, the optimum substrate temperature during growth is normally higher than that in MBE growth. Using group V organic precursors, the growth temperature can be reduced in MOCVD growth. For example, if phosphine is used as the source of phosphorous in MOCVD growth, the optimum growth temperatures are in the range of $600^{o}C$-$650^{o}C$, while with organic phosphorous precursors (TBP ($C_4H_{11}P$)) the growth temperature can be reduced to $530^{o}C$ -$570^{o}C$ due to it's lower decompose temperature.

By precisely controlling the source flow in MOCVD, it can produce nearly atomically abrupt interfaces layer structures. The major attractions of MOCVD relative to other techniques are its versatility and the suitability for the large-scale production. In general, favorable economic epitaxy growths require large scale, high growth rates, and high yield of suitable quality (i.e., uniformity and reproducibility). MOCVD is unquestionably the leading epitaxy growth technology for the mass production of virtually all III/V and II/VI semiconductor compounds. It has also been proven to be the most economical epitaxy growth technique, particularly for the production of devices requiring large areas, such as LEDs, photocathodes, and solar cells, etc.

Traditionally, arsine (AsH_3) and phosphine (PH_3) are employed as group V sources, and hydrogen is normally used as the carrier gas in $In_{1-x}Ga_xAs_yP_{1-y}$ MOCVD growth. Because of the high toxicity of AsH_3 and PH_3 and the explosive nature of H_2, safety becomes an important issue in MOCVD growth for both research and production. Therefore, search for substitutes for the toxic AsH_3 and PH_3 sources and the explosive H_2 carrier gas for MOCVD growth has been pursued in the past ten years [20-22]. Relevant researches have shown that organic compounds of these group-V elements, such as tertiary-butyl arsine (TBAs) and tertiary-butyl phosphine (TBP), have some crucial advantages: they are liquid phase in room temperature, they are safer due to their low vapor pressure and several orders of magnitude lower in toxicity than that of AsH_3 and PH_3. The lower decomposition temperature of the organic source group-V makes it possible to lower the epitaxy growth temperature. Lower growth temperature is useful for suppressing the diffusion of dopants in device structures where an abrupt doping profile is critical to the performance of the device [20][21]. Low threshold current multiple quantum well (MQW) laser diode has been realized by MOCVD using TBAs and TBP [22]. But all these works, H_2 was still used as the carrier gas.

In this project, TBP and TBAs were used accompanied with nitrogen as a carrier gas in the MOCVD growths.

2.4 Summary

InP and the related compounds are key semiconductor materials for optoelectronic devices used in fiber optical communications in 1.3μm and 1.55μm spectral regions. Three principal techniques in widespread use today for the deposition of InP related materials, LPE, MBE and MOCVD, have been introduced in this chapter. Both MBE and MOCVD have produced a wide range of very high-purity semiconductor materials with excellent optical and electrical properties. Due to its large scale, high growth rates, and a high yield of suitable material, MOCVD is the most suitable epitaxy growth technology for the mass production of semiconductor compounds and alloys based devices. With the use of organic compounds of group V precursors, MOCVD technology is becoming more promising and competitive.

Chapter 3 MOCVD technology and characterization techniques

3.1 MOCVD technology

3.1.1 Introduction

Based on deep understanding of the fundamental growth process and properties of the precursor molecules, MOCVD technology has been greatly developed and widely used for III-V and II-VI material epitaxy growths. Success of producing state-of-the-art materials, structures and devices have driven this technology from early empirical stage to a more mature epitaxy growth process. Experiments designed to probe the growth process have revealed the detailed surface process and the complex chemical dynamics in MOCVD growth.

In this chapter, MOCVD AIX 200 system, which was used in this research, has been introduced. The chemical and physical properties of the sources will be discussed. Basic transport and surface mechanism of MOCVD growth, such as thermodynamic and kinetics as well as hydrodynamics, will also be introduced.

3.1.2 MOCVD system

As mentioned earlier, an AIXTRON AIX 200 system was used in this project for MOCVD epitaxy growths. AIXTRON AIX 200 system is a system designed mainly for scientific research in epitaxy growth, and is capable of simple, versatile and uniform deposition of III-V semiconductor alloys. It consists of five main units as shown in Figure

3.1: gas blending unit, reactor with lamp-heated susceptor, vacuum system and scrubbing system, and a Programmable Logic Controller (PLC) system.

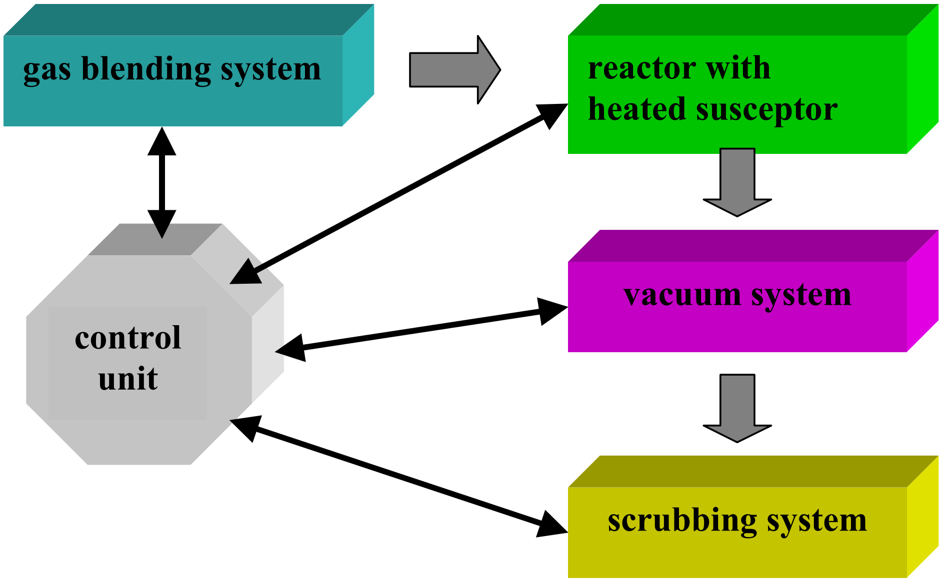

Figure 3.1: Components of low pressure MOCVD system

The gas blending system controls the incoming source gases and directs them to the entrance of the reactor through pressure regulators, mass flow controllers (MFCs), and valves. Seven metalorganic group III sources (TMGa, TMIn, TMAl, TMBi, TMSb, DEZn, TMAs) and 2 organic group V sources (TBAs and TBP) are connected to this system. All the source bubblers are placed in temperature-controlled baths to stabilize the source temperature. With an accuracy of 0.8% of setpoint for full range and 150ms settling time, AIXTRON mass flow controllers (MFC) are connected to each source handler to precisely control the source flow rate (SCCM) during epitaxy growth. Diluted silane with nitrogen at 2% concentration is connected to the system with a double wall stainless tube as the n-type doping source. For safety reason, it is stored in a specially designed cabinet. Purified nitrogen gas is used as a carrier gas in this system. It transports the source precursors from source bubbler in this reactor to the substrate for depositing the epitaxy layers, and at the same time to carry away the byproducts of the reaction during MOCVD growth.

All these flows are directed into either the reactor or a vent line, via a fast switching manifold. A separate injection system is used in the MOCVD system for pushing group V (TBAs and TBP) and group III metal organic sources (MO) into the reactor. This will minimize the pre-reactions of the sources in the gas delivery lines before they enter the deposition zone in the growth reactor. Figure 3.2 shows the horizontal reactor used in AIX 200 MOCVD system.

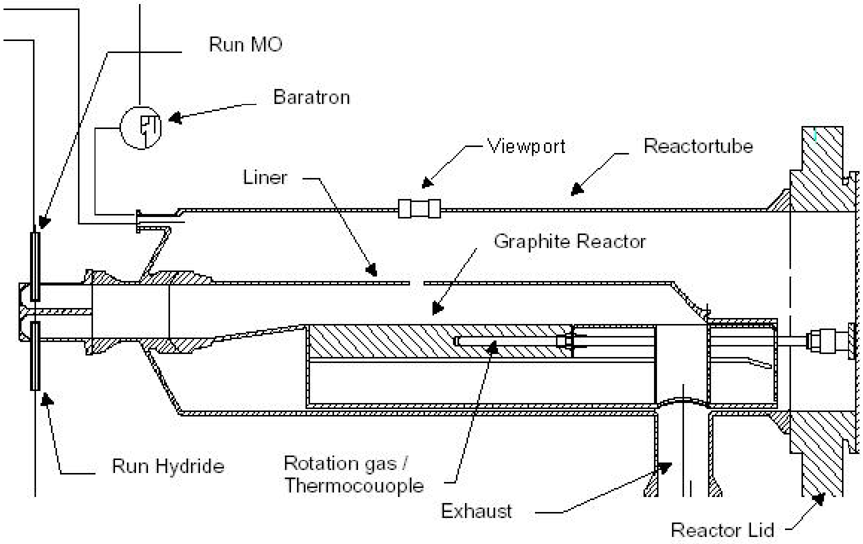

Figure 3.2: AIX 200 reactor with the monitoring viewport

MOCVD system is known as a cold wall reactor because the substrate and the susceptor in the reactor are significantly hotter than other parts of the reactor, so that the chemical deposition occurs mainly on the surface of substrate, which is fixed on the susceptor. The graphite susceptor is compatible with the precursors, and does not contaminate the growth materials. It is heated by infrared lamps parallel arranged under the graphite susceptor so as to heat the substrate uniformly. The horizontal quartz liner confines the gas source flow in a uniform way and makes the reactants flow parallel to over the wafer surface. The liner inlet region is made to taper slowly from the small inlet tube up to the final cross-section of the reactor to allow a laminar source flow pattern being formed and to avoid creation of re-circulating cells in the gas flow. To improve the uniformity of the deposited films, rotation of the substrate susceptor (satellite) is introduced in the system by using Gas Foil Rotation® mechanism.

Vacuum system in the MOCVD system maintains a constant pressure in the MOCVD reactor. With a two-stage slicing vane rotary pump and a throttle valve controlled by MKS pressure control unit, accurate process pressure can be achieved in the reactor. To prevent effluent leaving the reactor from accumulating in the vacuum system, a water-cooled exhaust filter is fixed prior to the pump to absorb the toxic particles from the waste of the deposition reactions in the reactor. Bypass lines with check valves ensure the system is in safe operation. The vent vacuum valve connects or separates the vent line and vacuum system for reactor. When the vent vacuum valve is open, the vent line will be held at the same pressure level as that in the reactor chamber. As a result, pressure fluctuations do not occur when the run/vent valves are switched.

A glove box filled with N_2 gas is connected to the end of the reactor to prevent exposing the reactor and substrate holder from contaminant in the environment during loading, unloading wafers and cleaning the reactor tube.

Scrubbing system provides safety for the environment. The effluent leaving the reactor consists of hot reaction gases, vapours, and particles. It contains the toxic materials of source flow which are not incorporated into the deposited films. The exhaust system trap or condition these reaction wastes before exposing them to the atmosphere. A specially designed two-stage scrubber with showering solution is connected to the MOCVD exhaust to absorb these undesired output materials.

Another safety consideration is the efficient exhaust ventilation system to ensure the environment in safe condition.

Computer control system in AIX 200 is operated by a combination of following systems:

a) PLC-5 (Programmable Logic Controller) of Allen Bradley for controlling the system to make all digital switches respond fast and reliable.

b) SLC 500 (Small Logic Controller) of Allen Bradley for the input and output the analog parameters to ensure precise control of the reactor temperature and source flow rate.

c) Safety system (SCS Safety Control System) of AIXTRON makes the system in safe status in case any possible process incident happens.

d) The CACE PC with a graphical interface for communication with the AIX 200 is installed. With a friendly interface, operator can easily modify and control the epitaxy process even as growth is in progress.

In-situ monitoring system (Filmetrics) is installed in AIX 200 system to measure the deposition rate and film thickness of the epilayer growth. To measure the growth rate, light from an optical fiber is directed to the surface of wafer on the susceptor via a viewport on top of the reactor. The reflected light from the wafer surface is detected and analyzed by computer to get the deposited film thickness while the surface morphology of the film can also be monitored by the reflected light intensity at the same time. With a separate Pyrometer, the accurate temperature on the wafer surface during MOCVD growth can be measured. As the receiver is Si based short wavelength detector (500nm-1000nm), it is not suitable for monitoring InGaAsP film growth.

3.1.3 Starting materials

MOCVD is distinguished by the chemical nature of the precursors used. In MOCVD processes, following desirable features are needed for MO precursors [7]:

a) Liquid form at room temperature is preferred to ensure reproducible transport of material into the reactor.
b) Precursors must be stable at room temperature, or it will not decompose at storage temperature awaiting use in the reactor.
c) Precursor molecule must be pyrolytic at the desired temperatures, which are different for the various materials being deposited.
d) Low oxygen and other dopants contamination preferred.
e) The precursor combination should not engage in parasitic reactions that the materials from the desired epitaxial layer onto walls, and so forth. Because the parasitic reactions not only reduce the reaction efficiency but also lead to inhomogeneities in the resultant epitaxial layers and irreproducible growth.
f) Hazard associated with use of the source molecule is as low as possible.

Based on the desired features of metalorganic source mentioned above, proper precursors were chosen for this MOCVD system.

3.1.3.1 Group III precursors

Trimethyl compounds (TMGa and TMIn) are used in our AIX 200 system as group III Gallium and Indium sources. Due to their higher vapour pressures and greater stability, they can be stored for very long periods at room temperature prior to use and are less likely to be involved in parasitic reactions. Solid trimethylindium (TMIn) is the precursor of choice for the vast majority of MOCVD applications. However, constant “pick up” has been a problem under normal operating conditions. Solution TMIn (TMIn suspended in a high boiling point amine adducted to TMIn) [1] was chosen as Indium precursor in this project. It has been proved that it has more consistent "pick up" and lower oxygen application [2].

3.1.3.2 Group V Sources

Despite their toxicity, the hydrides continue to be the most widely used Group V precursors in MOCVD growth in industry. In last decade, group V sources for traditional III-V MOCVD epitaxy growth were arsine (AsH_3) and phosphine (PH_3). Their widespread use is due to their combination of relatively low cost and high purity. The convenience of receiving a gaseous source of AsH_3 and PH_3 is also a reason. But their high toxicity, the high cost of storage, process safety monitoring and waste treatment, along with environmental concerns are considered during this system setup.

The organic materials tertiarybutylarsine (TBAs (AsC_4H_{11})) and tertiarybutylphosphine (TBP (PC_4H_{11})) are thus chosen in this system. The molecule structures of TBAs and TBP are similar to those of arsine and phosphine hydrides, except that one H atom is replaced with a bulky tertiarybutyl group. This makes TBAs and TBP much less toxic than their hydrides counterparts. And even better, they are in liquid form at room temperature, which significantly reduces the risk of widespread contamination in the event of a leak. Furthermore, TBAs and TBP decompose at much lower temperatures than that of AsH_3 and PH_3, permitting the use of lower substrate temperatures and V/III ratios during epitaxy growth. The higher incorporation efficiency of TBAs and TBP reduces the amount of source materials required in epitaxy growth, cuts the amount of As and P in the pumping system, and also reduces preventive maintenance time.

3.1.3.3 Dopants

The group II metal organic sources are fairly high vapour pressure liquids at room temperature. Dimethylzinc (DMZn) and diethylzinc (DEZn) are the most common p-type dopants for III-V material MOCVD growth. Both methyl and ethyl alkyls pyrolyze at relatively low temperature. For proper doping control, DEZn was chosen as p-type dopant in this system due to its lower vapour pressure.

Silane (SiH_4) is a mature material used in silicon industry. Small diffusion coefficient of Si makes it commonly used as an n-type dopant in MOCVD growth. Since silane is a flammable gas, safety is always considered in storing and using. In this system, silane is diluted with nitrogen to 2% (nitrogen is used as a carrier gas in this system) and the cylinder is kept in special gas cabinet.

3.1.4 Basic mechanism in MOCVD growth

3.1.4.1 Basic principles

MOCVD growth is believed to occur as follows [4,5,6,7]:

(a) The gas source molecules are carried to the reactor by the source flow and diffuse across the boundary layer of the source flow to the substrate surface.

(b) At the hot substrate surface, the metal alkyls and hydrides (or organic group V) of the source materials are decomposed, producing the group III and group V elemental species.

(c) The elemental species move on the hot substrate surface until they find available lattice sites and are attached there so that the epitaxy growth occurs.

Figure 3.3 schematically shows the epitaxy processes. Any of above three processes (a), (b), or (c) can limit the growth rate. But in LP-MOCVD, the epitaxy growth process often takes place under the conditions where process (a), species diffuse across the boundary layer, is the rate-limiting step. If it is the process (b) or (c) limits the growth, the growth rate will be strongly temperature-dependent, because the reaction coefficients are exponentially dependent on temperature. However, in diffusion-limited case (a), the growth rate is virtually independent of temperature and is controlled simply by the rate of arrival of the growing species from source flow onto the solid-vapour interface.

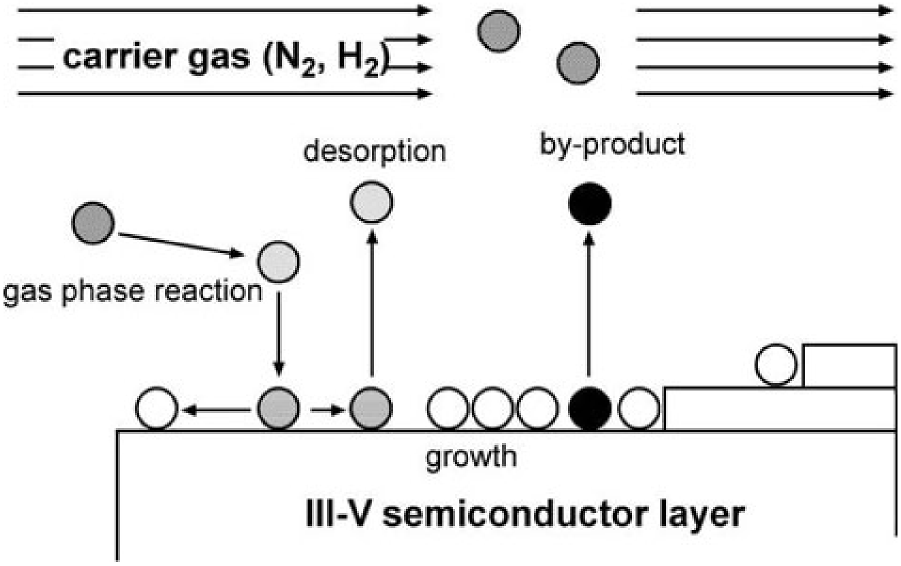

Figure 3.3: Principle of MOCVD process

The above explanation of MOCVD growth can be described by three major mechanisms: thermodynamics, kinetics, and hydrodynamics.

3.1.4.2 Thermodynamics and kinetics

Thermodynamics in MOCVD growth determines the driving force for the overall epitaxy growth processes, while kinetics defines the growth rates at which the various steps occur in epitaxy growth.

As MOCVD is an exothermic process, the maximum possible growth rate will be limited by thermodynamic forces which try to restore the equilibrium of the phase system in the growth chamber, the growth rate will decrease as the temperature of the reaction site (i.e., the heated substrate) increases. On the other hand, if kinetics dominates the growth rate, the reaction rates will limit the growth rate and it will increase as the temperature increases. Last, if the growth rate is limited by the mass transport of reactants to the substrate surface, the process is relatively temperature-independent. These three regimes typically lead to the "inverted bathtub" curve of growth rate vs. temperature as shown in Figure 3.4.

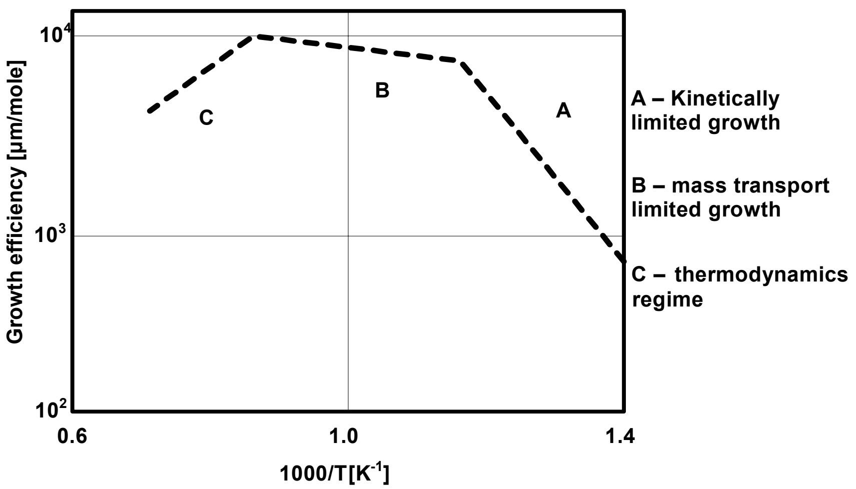

Figure 3.4: InP growth efficiency vs. growth temperature (after AIXTRON training)

This has been confirmed by experiment with the mass transport limited region occurring between 550°C and 700°C for InP MOCVD growth [3] (Most MOCVD processes are operated in this regime so that the growth rate may be reproducibly controlled by the flow rates of the reactants, and not by temperature critical or area sensitive processes.)

Considering the growth rate, the TMIn decomposition rate increases proportionally to the TMIn concentration.

$$r = k[TMIn] \tag{3.1}$$

where k is reaction rate constant. The linear relationship between k and TBP concentration [7] suggests the mixture of first-order and second-order kinetics:

$$k = k' + k''[TBP], \tag{3.2}$$

$$r = (k' + k''[TBP])[TMIn]. \tag{3.3}$$

As for the surface reaction of TMIn in the presence of TBP, it seems reasonable to assume that the surface decomposition of TMIn obeys pseudo-first-order kinetics rather than second-order kinetics, because the surface concentration of TBP, which is supplied in excess with respect to TMIn, seems to be saturated. Thus the decomposition of TMIn at InP surfaces is treated as a first-order reaction.

Above analysis leads to the reaction model for InP growth is being described in Figure 3.5. The model includes two gas-phase reactions (G1) and (G2), and two surface reactions, (S1) and (S2). The formulation of each reaction rate is described in the Figure 3.5. K_d is the mass-transfer coefficient of the intermediate.

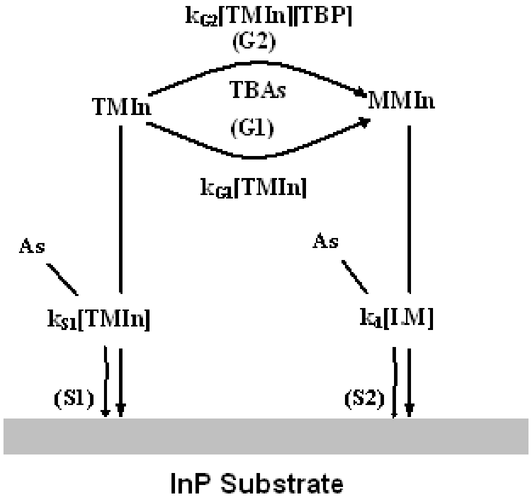

Figure 3.5: Reaction model for InP growth (adapted from [7])

For the MOCVD growth of InP, TBP is supplied in excess with respect to group III source, TMIn, by a factor of more than 10. Therefore, the InP growth rate is considered to be limited by the supply of Indium containing the intermediate. The gas-phase decomposition of TMIn includes both a first-order reaction (G1) and a second-order reaction (G2). The intermediate is assumed to be monomethylindium (MMIn)[6][7]. TMIn can also form InP directly through surface decomposition (reaction S1). MMIn diffuses to the InP surface and is converted to InP film through the surface reaction (reaction S2). It is assumed that the intermediate is highly reactive and thus InP formation is assumed to be limited by gas-phase diffusion. Therefore, we assume that the intermediate sticking coefficient is unity. The mass-transfer coefficient of MMIn is denoted as K_d. the reaction rate of S1 is much smaller than that of S2, so the major part of InP is generated from MMIn. The S1 reaction rate may depend on the surface condition such as the surface roughness of deposited InP.

3.1.4.3 Hydrodynamics and mass transport

Hydrodynamics concerns with the boundary layer of source gas flow in the reactor, re-circulation flows, mass transport processes and rates (diffusion), convection, nutrients to interface (products away from interface), the reactor wall effects, etc. Hydrodynamics and mass transport, which are intimately linked, determine the transport rate of material from the gas flow to the growing solid/vapour interface.

The concept of boundary layer is useful in understanding the gas flow kinetics [4] in MOCVD reactor. The fluid velocity of source gas flow inside the reactor must be zero at the substrate or a constraining wall, while the main fluid velocity is uniform. According to hydrodynamics calculation [5], the boundary layer thickness (as shown in Figure 3.6), defined here as the distance from the interface at which the velocity component parallel to the wall become 99% of its free-stream value, υ_0, is

$$\delta(x) = A\sqrt{\frac{\eta x}{\rho \upsilon_0}} = \frac{Ax}{\sqrt{\rho \upsilon_0 x / \mu}} = \frac{Ax}{\sqrt{R_e}} \qquad (R_e = \rho \upsilon_0 x / \mu) \qquad (3.4)$$

where $R_e = \rho \upsilon_0 x / \mu$ is Reynold number, A is a constant, υ_0 is free stream velocity, $\rho =$ gas density, μ is gas viscosity, it expresses the inertial forces dominated over viscous force. The thickness of the boundary layer is different when the carrier gas is different, as the viscosity is different for different gas flow. The higher the gas flow velocity, the thinner will be the boundary layer.

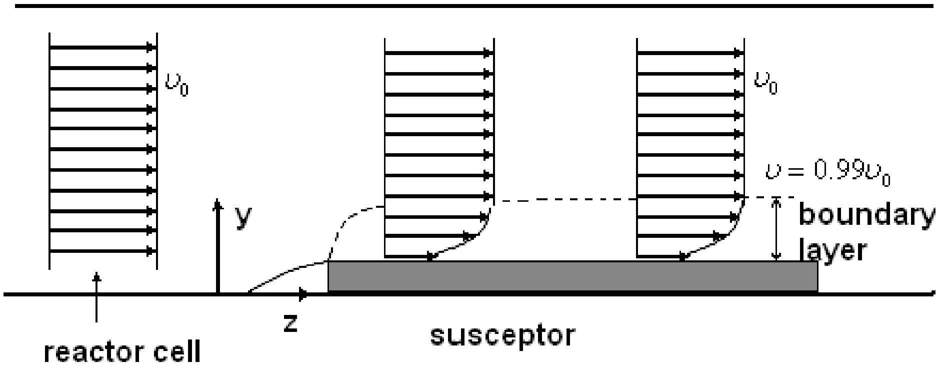

Figure 3.6: Development of boundary layer for parallel flow over a flat plate

From the R_e expression (3.4), it can be predicted that use of nitrogen as the carrier gas, the thickness of boundary layer becomes thicker. The diffusion of growth species in nitrogen gas will be slower than that in hydrogen gas because nitrogen gas has higher viscosity μ. Therefore, to reach the same growth rate, with identical consumption of metal organics, the total nitrogen flow rate will be higher than that by using hydrogen as carrier gas in order to get comparable growth rates.

The most widely used model for the calculation of the growth rate in the mass-transport-limited regime for all vapour phase epitaxial growth systems is the boundary-layer model. This model takes the velocity boundary layer described-earlier as a truly stagnant layer through which mass transport occurs only by diffusion. The idea originated in early experiment of Everstyn et al. [5] in which the flow pattern was imaged using smoke particles. A clear region near the heated substrate was observed that was interpreted as being due to the boundary layer. The thickness of the clear layer was observed to decrease in thickness with increasing flow velocities.

In the mass-transport-limited regime, growth rate is linear dependence on group III flow rate suggests that group III molecule is completely depleted at the solid/vapor interface. In simple case of diffusion through a mass-transport boundary layer, the group III flux, would be [10]

$$J = \frac{D(p^* - p^i)}{RT\delta_0} \tag{3.5}$$

where D is the diffusion coefficient, p^* is the input partial pressure of the group III source, p^i is the group III partial pressure at the interface, and δ_0 is the thickness of boundary layer. In the typical case where $p_V^* >> p_{III}^*$, growth rate is independent of group V flow rate. The group III flux, hence the growth rate, is proportional to p^* only if $p^i << p^*$. This is an accurate representation of an experimental observation for the MOCVD growth of essentially all III/V system. Equally clear is that the ratio of the concentrations of A and B for alloys with mixing in the group III sublattice, $A_xB_{1-x}C$ will be the same as the ratio p_A^* / p_B^*, assuming the diffusion coefficients for A and B species nearly equal.

3.1.5 Summary

AIX 200 MOCVD system was described in details. With advanced automation technology and enhanced mechanical design, MOCVD has more versatile and possesses higher capacity than other epitaxy techniques due to mass production application ability. High purity of metalorganic sources ensures the high quality of grown material. Application of organic group V and N_2 makes MOCVD process safer. With better understanding of basic mechanisms in MOCVD growth, good quality material can be achieved and better controlled.

3.2 Characterization techniques

3.2.1 Introduction

Material characterization techniques used in III-V semiconductor material epitaxial growth have been developed parallel to the epitaxial deposition techniques. They are very important for optimizing the growth conditions to obtain good quality epitaxial alloys and structures.

Common techniques used in characterizing crystal quality, material compositions, electrical and optical properties of epitaxial films and structures include: high-resolution X-ray diffraction (HRXRD), electrochemical C-V profiling, photoluminescence (PL), Hall effect measurement, microscopy, Raman scattering, etc.

In this section, principles and applications of characterizing techniques, e.g. XRD, PL, will be introduced. By using characterization techniques, correlations between the structure design and optical/electrical properties of epilayer can be revealed, and ultimately, the operational characteristics of the device can be achieved.

3.2.2 High-resolution X-ray diffraction (HRXRD)

X-ray diffraction technique is indispensable for the non-destructive evaluation of crystalline materials. This technique has been successfully employed for the crystal structural characterization of thin crystalline layers, multi-layers and superlattices. The determination of geometrical dimensions, such as the thickness of single layers, the vertical period in superlattice structures, the lateral period of gratings, and the mean crystalline properties (mean lattice parameters of a grown layer) are today's routine tasks in any x-ray laboratory attached to an epitaxy-growth group.

The relation between the solid composition of a grown film and its lattice parameter forms the basis of XRD measurement. The lattice constant of single crystal alloys gradually changes with the alloy compositions. It can be approximated by a linear interpolation of the lattice parameters of the binary end members. This relationship is known as Vegards's rule. For the ternary compound $A_xB_{1-x}C$, Vegard's rule for the lattice parameter reads:

$$a_{A_xB_{1-x}C} = x \cdot a_{(AC)} + (1-x) \cdot a_{(BC)}, \qquad (3.6)$$

where a is lattice constant.

When X-ray shines on a single crystal, diffraction of the X-ray will occur as shown in Figure 3.7.

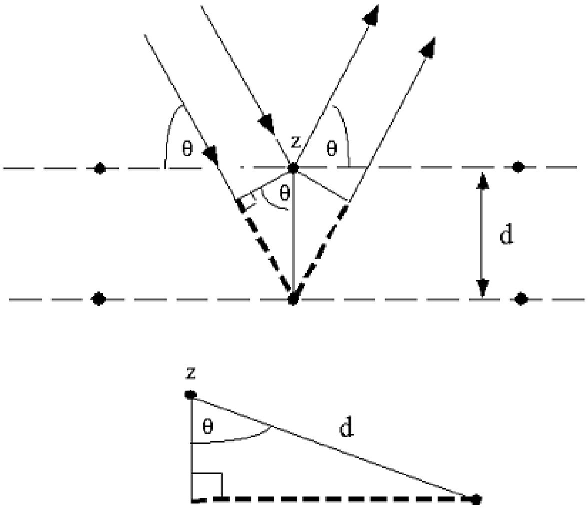

Figure 3.7: Bragg reflection on crystal plane

The diffracted X-ray beam is composed of many X-ray waves that have been scattered by the atoms in a crystal. The diffracted X-ray waves show maximum only at certain angles, called Bragg angles, where the Bragg angles satisfy

$$n\lambda = 2d\sin\theta, \tag{3.7}$$

where λ is the wavelength of the X-ray, d is the distance of diffraction plane (lattice constant), and θ is diffraction angle.

For optoelectronic devices, compound semiconductors are not used as homogeneous bulk material but usually come in the form of layered heterostructures. Whereas in homogeneous bulk materials the lattice parameter is measured by an absolute measurement, in layered systems the difference of the lattice parameters of the layer with respect to the substrate can be measured. For these relative measurements, a rocking curve is measured assuming that the lattice parameter of the substrate is known.

Using X-ray diffraction technology in analyzing grown InGaAsP/InP epitaxial structures, two conditions have to be satisfied:

a) High resolution of the XRD system is needed for lattice mismatch measurement to get accurate material composition.

b) High intensity X-ray is needed in the XRD system, as the X-ray intensity of the diffracted beam is much smaller than that of the incident X-ray intensity. To get accurate measurement, strong X-ray source in the XRD system is necessary.

To meet these requirements, a high-resolution diffractometer is needed in a XRD system. Usually, a (+n, -n) double crystal or (+n, -n, -n, +n, m) five crystal arrangements are used to improve the measurement accuracy. Resolution of a double crystal arrangement in XRD measurement is the best if the Bragg angles of the monochromator and that of the sample crystal are the same. But the resolution of measurement becomes worse when the difference of the Bragg angles increases. This drawback can be eliminated in a five-crystal diffractometer (as shown in Figure 3.8).

A five-crystal diffractometer is with a (+n, -n, -n, +n) four reflection monochromators. When X-ray passes through the four crystals at a proper angle, only K_α

line can pass through while K_β line will be absorbed. Narrower bandwidth X-ray makes high resolution applicable. To increase the intensity of incident X-ray, Girber mirror (coating with Germanium crystal film) is used to focus the X-ray beam. Using such a five-crystal arrangement, resolution and intensity requirements can be fulfilled for any refection, and the resolution of the diffractometer does not depend on the choice of the sample material and the Bragg reflection. The XRD system, Philips MRD, used in this project is based on above considerations.

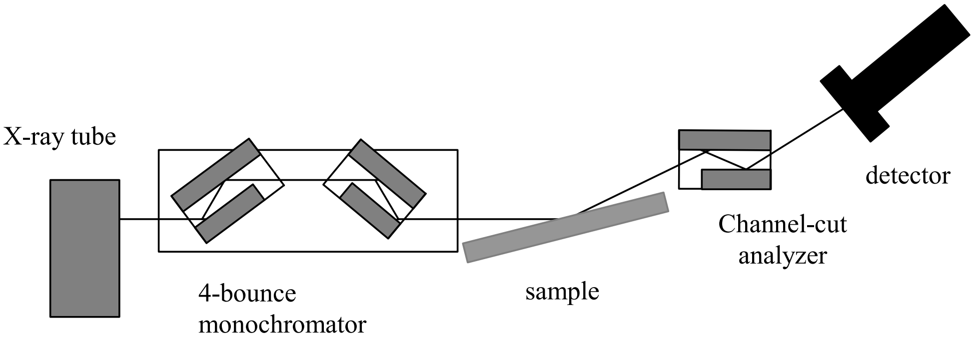

Figure 3.8: Schematic setup of a high-resolution X-ray diffractometer using 4-bounce monochromator

In measurement, the diffracted X-ray is bounced off an analyzer crystal to the detector. The X-ray then travels through a Beryllium window and strikes the NaI, sodium iodine, and scintillation crystal. There the X-ray is turned into a photon and enters the phototube which ends in the signal amplifier. Through the phototube, the pulse of the photon is transported to the pulse height analyzer and the output computer. The data collected are converted into raw data file for analysis. With the help of simulation software, we can obtain structural information of the sample, such as mismatch, composition (with the input of RT PL data for quaternary alloy), thickness, etc.

XRD measurement can also be used to calculate the strain and thickness of the epitaxy layer.

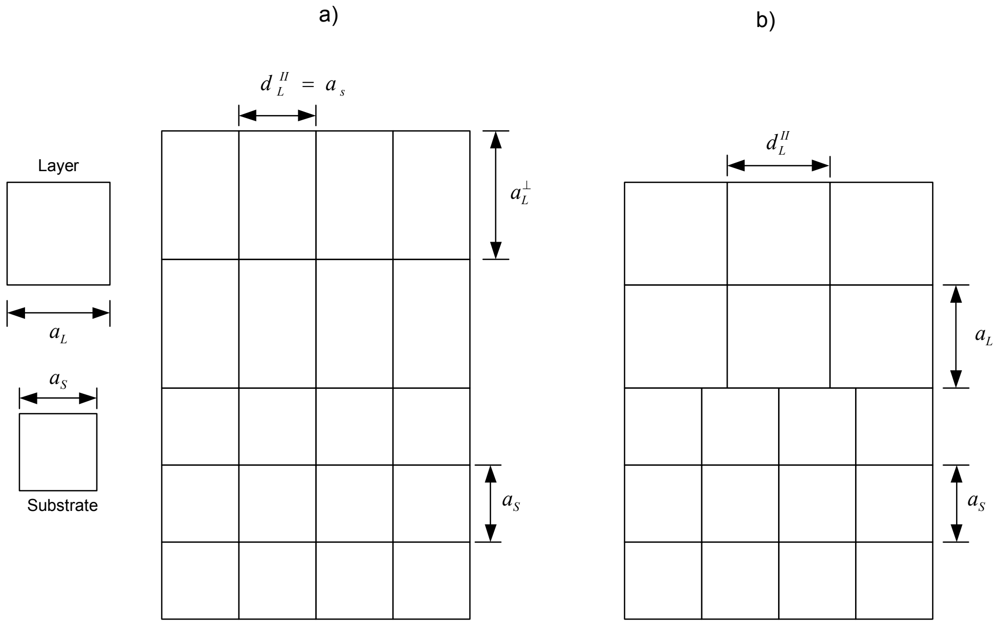

Figure 3.9: Epitaxial Heterostructures. a) pseudomorphic layer, b) partially relaxed layer.

In heteroepitaxial systems the lattice parameters of the layer a_L and the substrate a_S usually differ slightly. If the so-called relaxed lattice mismatch,

$$\frac{\Delta a}{a} = \frac{a_L - a_S}{a_S} \qquad (3.8)$$

is not too high, the unit cell of the layer will conform laterally to the lattice of the substrate (Figure. 3.9a). Under the influence of the elastic stress, the unit cell of the layer undergoes a tetragonal distortion. With increasing layer thickness the stress relaxes by dislocations (Figure. 3.9b).

During the XRD measurement, when the peaks within a reflection profile have been assigned, the lattice mismatch can easily be determined. It is necessary, however, to distinguish between pseudomophic layers and (partially) relaxed layers. For the crystal layer growth, most cases are concentrated on psuedomorphic layers. This type of layer exists if the so-called relaxed lattice mismatch or the layer thickness is not beyond the critical value's *t*, given by following equation [8],

$$\left(\frac{\Delta a}{a}\right)_{crit.} = \frac{(1-v/4)}{2\sqrt{2}(t/a_s)(1+v)}\left[\ln(\sqrt{2}(t/a_s))+1\right], \tag{3.9}$$

where v is Poisson number and is given by $v = (C_{11} + C_{12}) \approx 1/3$.

For determining the lattice mismatch, in this case, it is sufficient to measure the rocking curve of a single symmetric reflection, usually the (004) reflection. The angle difference $\Delta\theta$ between the substrate and layer reflection is used to calculate the lattice mismatch. As is shown in Figure 3.10. For the evaluation of small lattice mismatches the differentiated Bragg equation is used:

$$\frac{\Delta a}{a} = -\Delta\theta \cot\theta_B \tag{3.10}$$

where $\Delta\theta$ in rad, θ_B is Bragg angle.

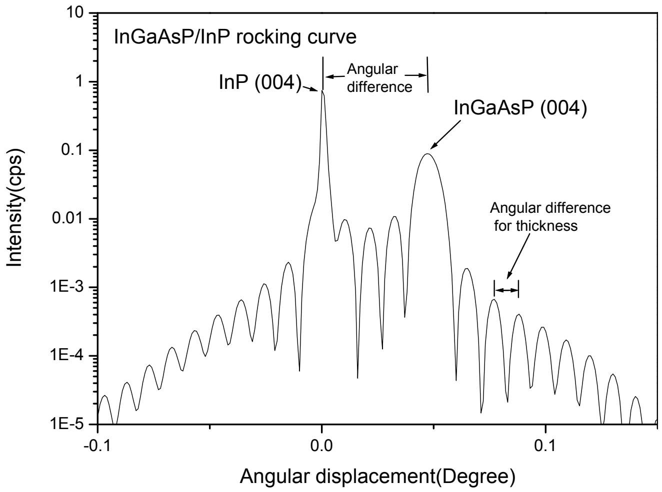

Figure 3.10 XRD (004) rocking curve on InGaAsP/InP

Apart from giving the lattice mismatches, the rocking curve also yield information about the layer thickness. It can be calculated from fringes of the rocking curve. The interference effect is similar to the interference of a simple slit in optics. The maximum of the thickness fringes has double the width of the side maxima. From the angular width of the side maxima, for symmetric reflex, the layer thickness is derived by [8]

$$t = \frac{\lambda}{2\Delta\theta} \qquad (3.11)$$

where $\Delta\theta$ in rad.

In addition, the thickness of the repeat unit of a superlattice also could be determined from the satellite distance. The thickness fringe peaks are caused by interference between X-ray waves with different refractive indices. The following equation for the calculation of the layer thickness is used [8]:

$$t = \frac{\lambda \sin \omega_e^0}{\sin 2\theta_B |\eta_1 - \eta_2|};\ \omega_e^0 = \theta_B + (\pi/2 - \varphi)\,. \qquad (3.12)$$

Here ω_e^0 is the exit angle of the beam; λ is the wavelength of X-ray, $\eta_{1,2}$ are the deviation parameters for the 1st and 2nd fringes respectively. These values are obtained from the corresponding angular deviations $\Delta\omega_{1,2}$ relative to the 0-order peak for the layer under consideration.

3.2.3 Photoluminescence (PL)

Photoluminescence spectroscopy is a contactless, nondestructive method of probing the electronic structure and optical properties of materials and structures. It is widely used to measure the energy bandgap of semiconductors and then to decide the compositions of semiconductor alloys. It can also be used to study the energy states of low-dimensional semiconductor structures.

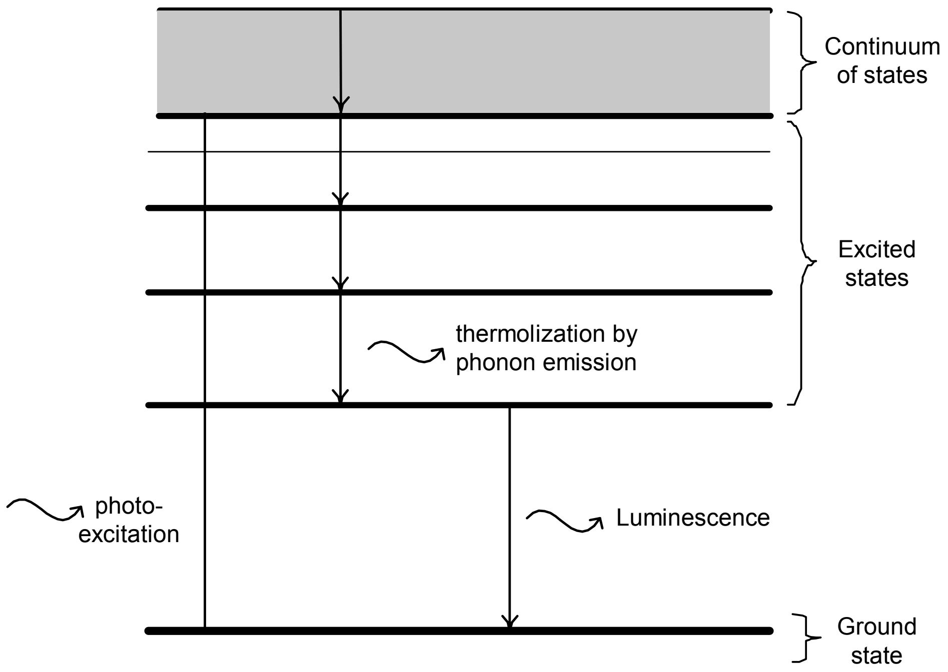

Figure 3.11: An simplified energy diagrams of photoluminescence

Figure 3.11 shows a simplified mechanism of photoluminescence. Light is directed onto a sample, where it is absorbed by the material and excites electrons from lower energy level to the permissible excited energy levels called "photo-excitation". When these electrons return to their equilibrium states, the excess energy is released and may include the emission of light (a radiative process) or no emission (a nonradiative process). The energy of the emitted light (or photoluminescence) is related to the difference in energy levels between the two electron states involved in the transition, that is, between the excited state and the equilibrium state. The quantity of the emitted light is related to the relative contribution of the radiative process. This luminescence is called "photoluminescence”. The intensity and spectral content of this photoluminescence is a direct measuring of various important material properties.

The most common radiative transition in semiconductors occurs between the minimum conduction band and the maximum valence band, with the energy difference known as the bandgap, E_g, of the semiconductor. As each kind of semiconductor material has a certain bandgap, PL is the direct measurement of the bandgap. People use PL as one of the methods to determine the composition of the material. For the element, binary compound, PL result can tell what the material is and the composition of the ternary compound. For quaternary alloys, PL measurement combined with the XRD measurement can determine their composition. Also, radiative transitions in semiconductors involve localized defect levels (impurity levels) as shown in Figure 3.12. The photoluminescence energy associated with these levels can be used to identify specific defects in the semiconductor, and the intensity of photoluminescence can be used to determine their concentration.

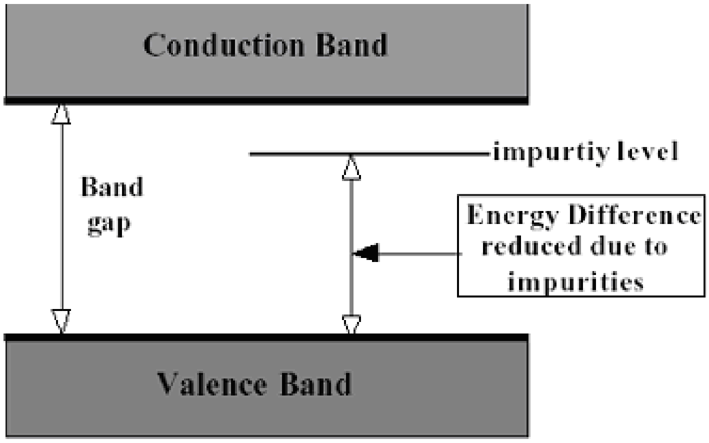

Figure 3.12: Energy difference reduced due to impurities

In general, nonradiative processes are associated with localized defect levels, whose presence is detrimental to material quality and subsequently the device's performance. Thus, material quality can be measured by quantifying the amount of radiative recombination.

Figure 3.13 shows schematically the experimental set-up of the PL measurement used in this project. The excitation source is a CW YAG laser with a maximum output power of 400mW and peak wavelength at 1064nm. This 1064nm laser source is used for long wavelength (1100-2000nm) materials' (InGaAs and InGaAsP) PL measurement, while the excitation source for short wavelength (550-1000nm) materials' PL measurement (InP) is a CW Ar^+ laser with maximum output power of 100 mW and peak wavelength at 514.5 nm.

The exciting laser beam is focused onto one of a 3 dB fiber coupler's inputs using an objective lens. A mechanical chopper is used to modulate the laser beam to provide a reference frequency signal to the lock-in amplifier for its phase sensitive detection amplification.

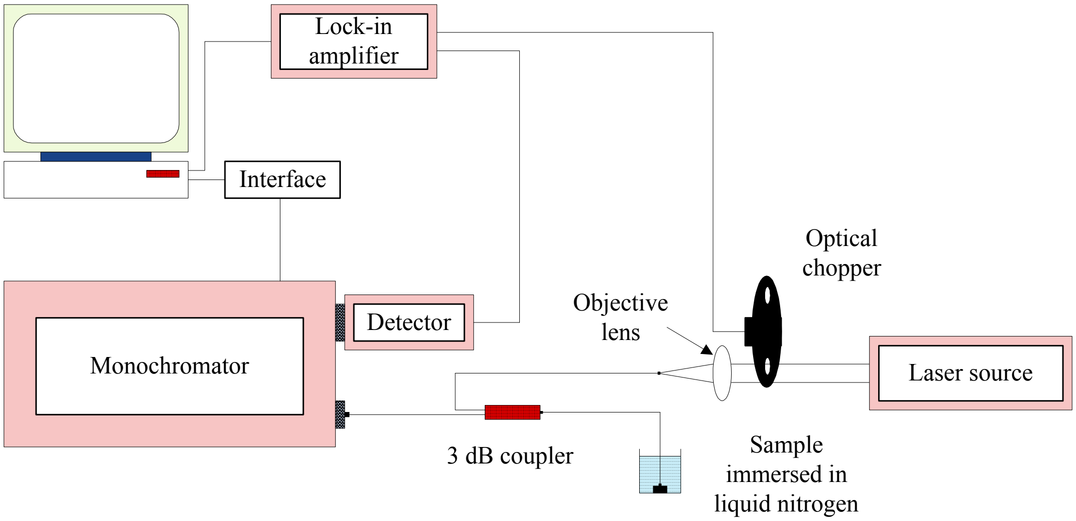

Figure 3.13: Schematic diagram of the PL experimental set-up

The sample to be measured is attached to the output end of the 3dB fiber coupler. For low temperature measurement, immerse the sample together with the input of the fiber coupler into a liquid nitrogen container. The excitation laser beam shines on the sample through the input of the 3 dB coupler, while the PL signal from the sample together with the reflected exciting light are collected by the same output end of the 3 dB coupler and are then guided into a monochromator through the other output of the coupler. The PL spectrum of the sample is decomposed by an optical grating equipped in the Oriel monochromator and is detected by either a TE cooled InGaAs photo-detector (for long wavelength) or a TE cooled Si-detector (for short wavelength). A SR-830 lock-in amplifier is used to amplify the signal collected from the photodetector and then the amplified signal is sent to a computer to process the measured results.

3.2.4 Summary

PL and HRXRD measurements are very important for characterizing compound semiconductor epitaxial layers. PL measurement provides information of both alloy compositions and, indirectly, the crystal quality of epitaxial films. High-resolution X-ray diffraction is used to measure the alloy composition, layer thickness, and lattice-match conditions of heteroepitaxial grown layers. With the correlations between the structural properties and optical-electrical properties of grown samples, the epitaxy growth conditions can be optimized, and ultimately, the operational characteristics of the device can be made.

Other characterization techniques, such as Electrochemical C-V (EC-V) profiling, Hall bar measurements and Raman spectroscopy, are introduced in Appendix C.

Chapter 4 MOCVD growth of InP bulk materials

4.1 Introduction

III-V semiconductor material Indium Phosphide (InP) has a bandgap energy of 1.35eV. Like many III-V semiconductors, InP is direct bandgap semiconductor, which can be employed to fabricate fast absorption modulators and photo-detectors, as well as optical amplifiers. When the photon energy is close to the bandgap, electro-optical effects are relatively strong. InP has a very important potential application for fabrication of Photonic Integrated Circuits, in which active optical components such as lasers, amplifiers, and optical switches are combined with passive elements such as (de)multiplexers, splitters and couplers on a single chip.

In this chapter, the growth conditions of InP epitaxial film are developed and optimized based on an AIX 200 MOCVD reactor. Using XRD and PL measurement, crystal quality and optical properties of the InP grown films were characterized, while the electronic property of the films was studied with help of Hall measurement. Detailed investigations on Si and Zn doping in InP films were also carried out by means of ECV.

4.2 MOCVD growth of InP bulk layer

4.2.1 InP bulk layer growth optimizing

To optimize the growth conditions, thick InP bulk layers were grown in the MOCVD system. Fe-doped semi-insulating (100) oriented InP wafers were used as substrates. TBP (tertiabutylphosphine) and TMIn (trimethylindium) were used in the InP layer growth as group V and group III sources, respectively. N_2 was used as the carrier gas. The reactor pressure was set at 100 mbar for all the growths.

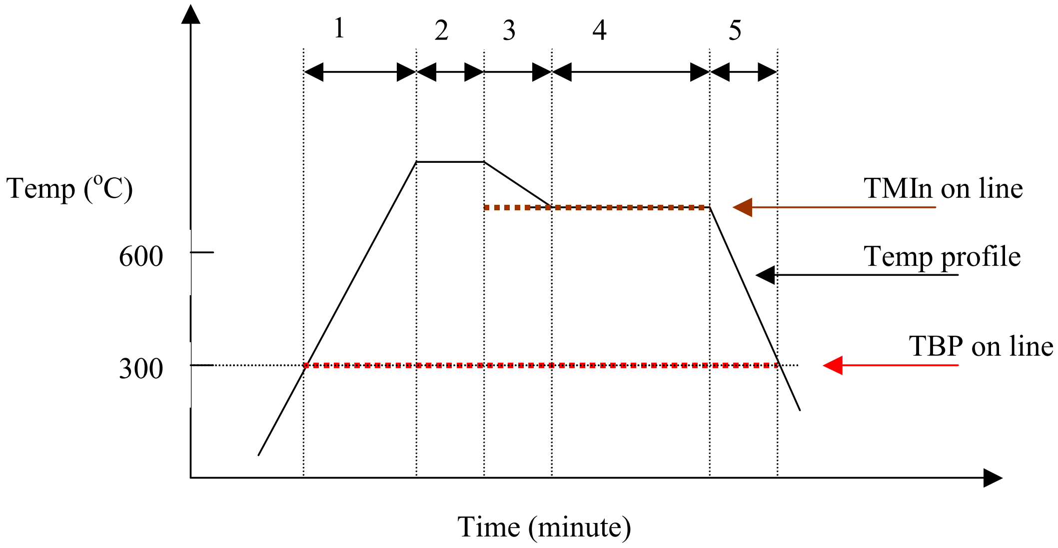

Figure 4.1: Temperature profile for the InP/InP growth

Figure 4.1 shows the heating up sequence of the epitaxy growth procedure. TBP was injected into the reactor to avoid surface degradation of InP substrate when the temperature reached 300°C (zone 1), then continued to heat up the substrate to 680°C. Keeping at that temperature for 5 minutes to remove the possible oxide layer on substrate (zone 2) before starting the epitaxial growth. TMIn was then introduced in the reactor to start the InP buffer layer growth (zone 3). At the same time, temperature was ramping down to 630°C during the buffer layer epitaxy growth to reduce the density of defects and prevent propagation of the dislocation from the substrate. Following the buffer layer, an InP layer was grown at 630°C to the estimated thickness (zone 4). To prevent surface decomposition during cooling down, TBP source flow was kept until the substrate temperature was lowered to 300°C (zone 5).

To optimize InP growth conditions, two parameters were taken into consideration.

a) Total flow effect:

From the geometry design of AIX 200 horizontal reactor, the depletion profile of the growth rate at the deposition zone along the source flow direction is shown as in Figure 4.2.

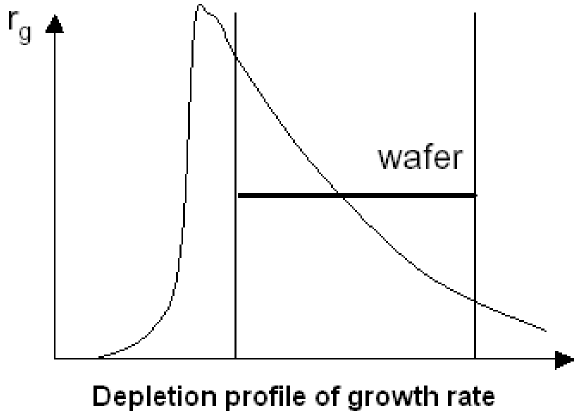

Figure 4.2: Lateral gas depletion profile of the growth rate for AIX 200 system (After AIXTRON training)

From this growth rate profile, the gas-phase depletion of the reactants along the flow direction leads to a decrease of available reactants concentration to the growing film from the leading to tailing edge of the susceptor (along the gas flow direction). Different diffusivities and/or incorporation rates of the Group III and V species can, therefore, make the mole fraction different. In InP growth, as the V/III ratio was much larger than 1, TMIn depletion in growth zone is more important in the epitaxy growth.

The depletion along the susceptor is dependent on the velocity of the reactants gas stream flow. Along the gas flow direction, there is variation of thickness distribution. With the rotation of the substrate, this variation can be improved. But the symmetric side-to-side non-uniformity produced by the lateral variation in the gas velocity combined with gas-phase depletion can not be eliminated with the wafer rotation.

As TMGa and TMIn have similar diffusion coefficients and thermal diffusion factors [1], parameters for TMGa were used as the reference for TMIn. According to Fick's law with a TMIn diffusion coefficient [2] of

$$D(T) = 0.378(\frac{T}{300K})^{1.88} \text{ cm}^2\text{/s} \tag{4.1}$$

the TMIn flux arriving on top surface of the substrate in MOCVD reactor can be written as [2]:

$$J(z) = 0.89DC_0(\frac{Dhz}{\upsilon_0})^{-\frac{1}{3}}, \tag{4.2}$$

where C_0 is the input concentration of the source material, h is the height from substrate surface to the ceiling of the reactor and υ_0 is the average velocity of the source flow in the reactor.

Theoretically, $J(z)$ changes with the total flow rate υ_0, and the profile of the flow pattern becomes flatter compared with that at low total flow rate.

Based on Eq. (4.2), the growth rate changes with the flow rate if we assume that In incorporation changes linearly with TMIn flux. This was checked in growth of InP epilayer. In the experiment, the view hole on top of the liner was covered with a quartz plate to get rid of the influence of the liner purge flow on the epitaxy growth. Other growth conditions were kept same except for the total flow rate. A thin InGaAs etch stop layer was grown between the InP buffer layer and the InP epitaxial bulk layer to provide an interface for the InP layer thickness measurement. To measure the epilayer thickness, the wafer was cleaved and stained with a mixture of H_3PO_4: H_2O_2: H_2O =1 : 1: 100. By both SEM and microscope, thickness of the InP epilayer was measured. Table 4.1 gives the thickness measurement results of the samples grown with different flow rates. The relationship of thickness uniformity and total flow rate is plotted in Figure 4.3.

Table 4.1 Measurement results of InP epilayer thickness varies with the total flow rate (growth time=2 hours)

Run No	Total flowrate (SCCM)	Total III Input (mol/min)	Edge +5mm	Edge +10mm	Edge +15mm	Edge +20mm	Center	Average g-rate (um/hr)
R7	3200	3.52E-05	1.680	1.710	1.730	1.760	1.800	0.820
R12	3800	3.52E-05	1.941	1.920	1.900	1.865	1.825	0.950
R13	3500	3.52E-05	1.810	1.810	1.810	1.810	1.810	0.900

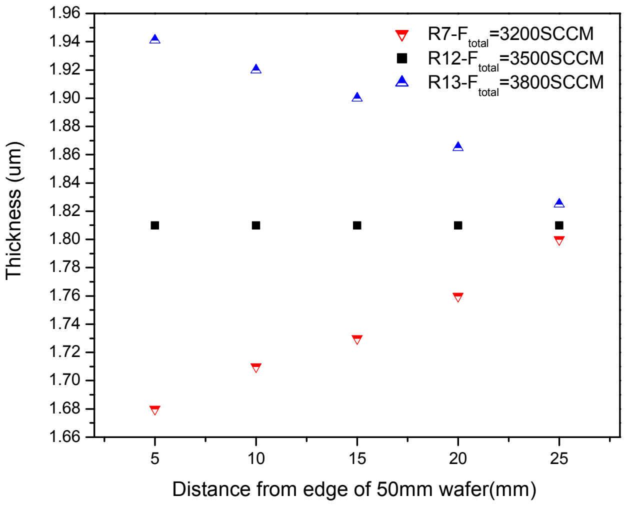

Figure 4.3: Thickness uniformity of epilayer on a 50mm diameter wafer varies with different total flow rates during the MOCVD growth.

From the measurement results, with the gas foil rotated substrate, very good thickness uniformity has been achieved with the total source flow of 3500 SCCM, which is related to the overall hydrodynamic design of the reactor.

The experimental results also show that the growth rate (average growth rate) increases with increasing the total flow rate. This is mainly due to the decrease of the boundary layer thickness of the source flow when the total flow rate increases, which enhances the diffusion coefficiency as described in Chapter 3. The analysis shows that at the growth temperature of 630°C, at which source mass transport dominates the epitaxial growth, the growth rate still changes with the total flow rate, even the TMIn flow was kept constant. The only reason for this phenomenon is that the boundary layer thickness varies when the total flow rate changes.

b) Liner purge flow rate effects:

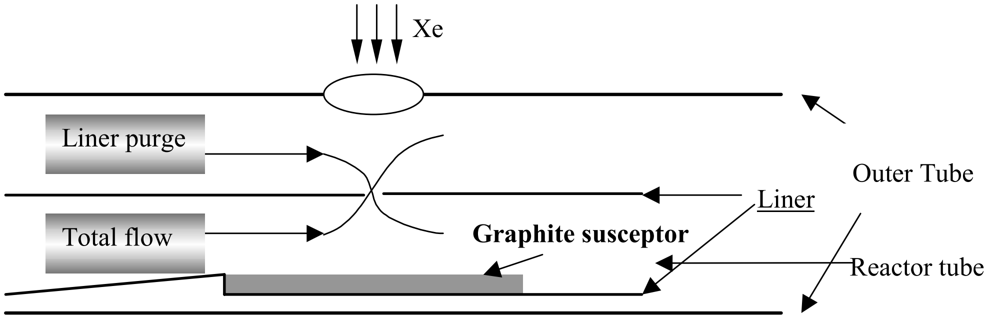

Figure 4.4: Demonstration scheme of liner hole affection with total flow rate and liner purge flow rate

Figure 4.4 shows the reactor scheme structure of AIX 200 reactor. It is equipped with a filmetrics system for in-situ monitoring of the growth rate and surface morphology. For this purpose, the light of Xe lamp passes through a view port of reactor and the open hole on top of liner, shines on the surface of the wafer. The growth rate and surface of the wafer is monitored by measuring the reflectance through the same view hole. N_2 purge gas passes through the outside of liner to prevent the deposition on the inner wall of outer tube. This configuration will, of course, affects the gas flow pattern which flows over the substrate inside the reactor tube if the flow rate and pressure are not balanced between inside and outside of the liner.

To balance the pressure and flow rate, experiments were carried out by changing the liner purge flow rate while the total flow rate inside the liner was fixed. Table 4.2 shows the experimental results of the epilayer's top surface morphology with different liner purge flow rates.

Table 4.2 Relation between liner purge flow rate and wafer quality

Run No	Liner purge flow rate (SCCM) (SCCM)	Total flow rate in liner (SCCM)	Deposition on inside reactor	Pattern appears on Wafer Y.N?	Microscope observation
R1	2000	3500	No	Y	Polycrystal
R2	1500	3500	No	Y	Polycrystal
R19	3100	3500	No	Y	Polycrystal
R20	3500	3500	No	Y	Polycrystal
R149	400	3500	Yes	Y	Single crystal
R150	500	3500	No	N	Single crystal

It shows that for the liner purge flow rate >2000 SCCM, a circle pattern appears at the center part of the wafer surface, as shown in Figure 4.5. Under microscope observation, the pattern area surface is polycrystal while the surface outside the center pattern area is very smooth.

Increasing the liner purge flow rate will affect the flow pattern inside the reactor, and thus affect the growth deposition. The liner purge gas flow through the hole will disturb the laminar flow in the growth zone to cause turbulent flow. So there is no uniform boundary layer for the reactant source flow. While the liner purge flow rate is too low (<400SCCM), the reactant materials will go out from the reactor tube through the hole on top of liner, and the pyrolized reactants will deposit on the inner wall of outer tube. According to experiment, the balanced liner purge rate and total flow rate is

500SCCM/3500SCCM for this reactor configuration. By using this flow rate, no circle pattern is observed. A mirror shining surface is received as shown in Figure 4.6.

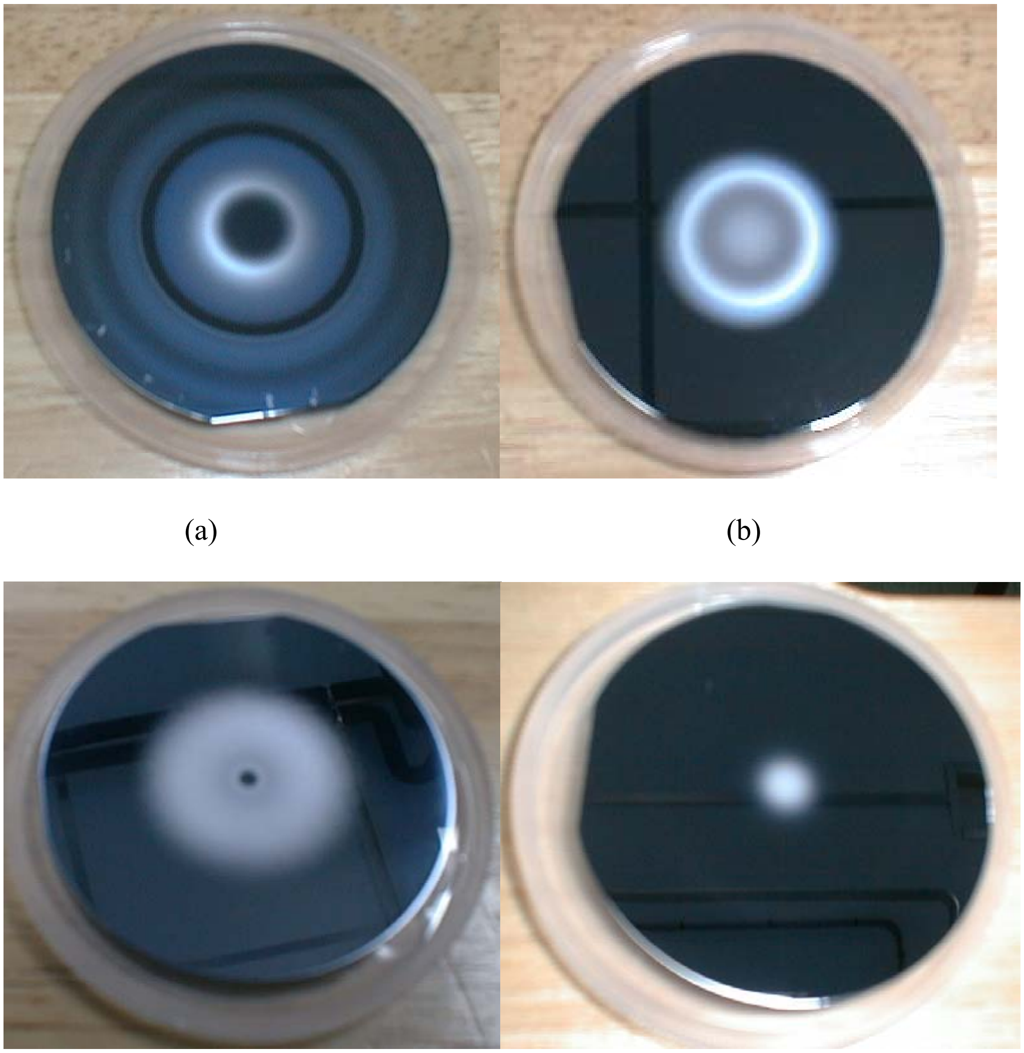

(a) (b)

(c) (d)

Figure 4.5: Photograph of surface pattern in InP/InP growth varies liner purge flow rate: (a) 3500SCCM (b) 3100SCCM (c) 2000SCCM (d) 1500 SCCM

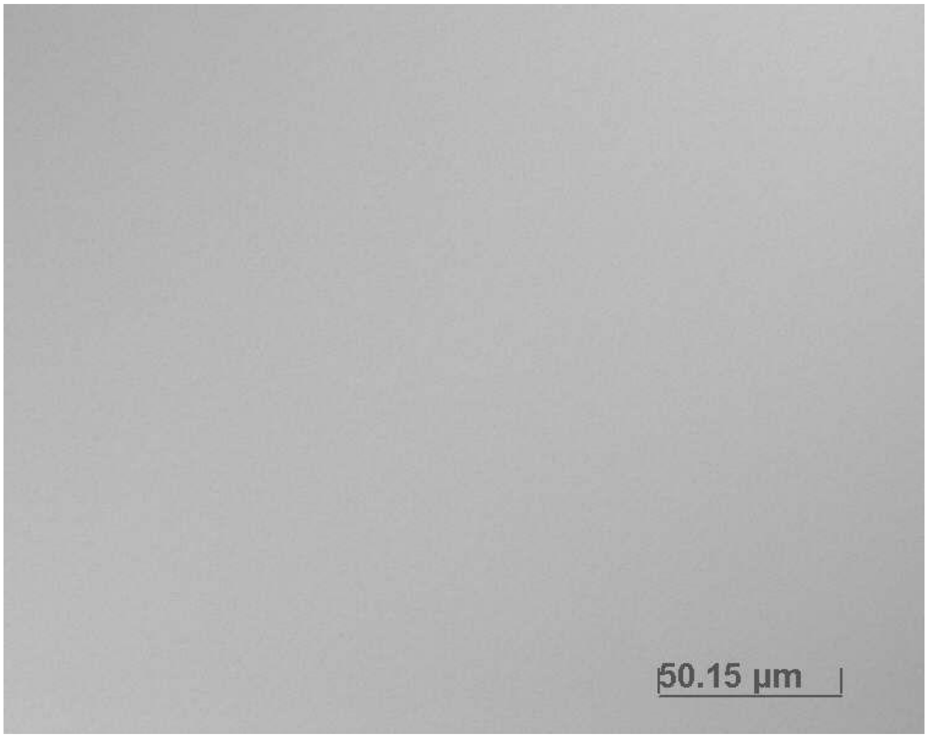

Figure 4.6: Surface morphology of InP epilayer grown under optimized growth condition

With the optimized total flow rate and liner purge flow rate, the InP epilayers with very good uniformity has been grown as shown in Figure 4.3 (sample R12).

4.3 InP epilayer characterization

As shown in above section, under the optimized growth conditions, mirror-like InP epitaxial layers were grown. Photoluminescence measurements of the samples were performed at 300 K using CW Ar^+ 514.5 nm laser as the excitation source. Figure 4.7 shows the comparison of PL results of the grown InP epilayer and a Fe doped InP substrate.

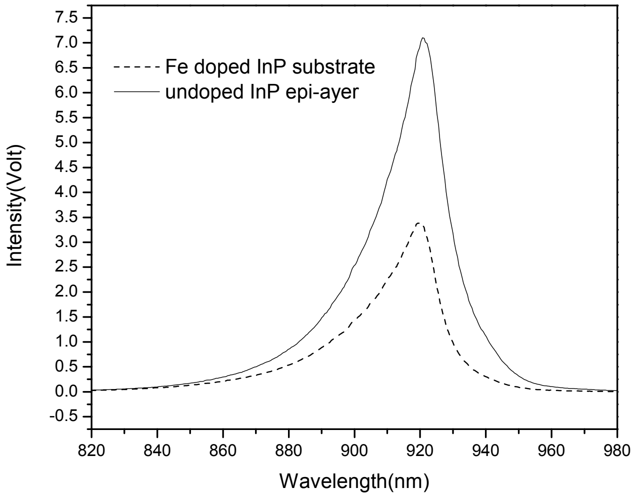

Figure 4.7: Comparison of room temperature PL spectra from an undoped InP epilayer and Fe-doped InP substrate

The PL intensity of the InP epilayer is 2 times stronger than that of the substrate (Fe doped). The full width at half maximum (FWHM) linewidth of the epilayer PL spectrum (22nm) is same as that of PL spectrum of the Fe-doped InP substrate. The lower PL intensity from the InP substrate is because of the Fe dopant. The Fe ions give rise to deep energy level traps in InP material. When electron and hole carriers are generated by photon excitation, Fe will trap some of them through non-radiative recombination. This causes lower PL emission intensity from the Fe-doped InP substrate.

To check the crystalline quality of the InP epitaxial layer, XRD (004) Bragg reflection measurement was carried on the InP grown epilayer sample and a Fe doped InP substrate for comparison. Figure 4.8 shows the results of XRD rocking curves.

Since the FWHM of epilayer and substrate is compatible, we can assume that the epilayer has same crystal quality as substrate.

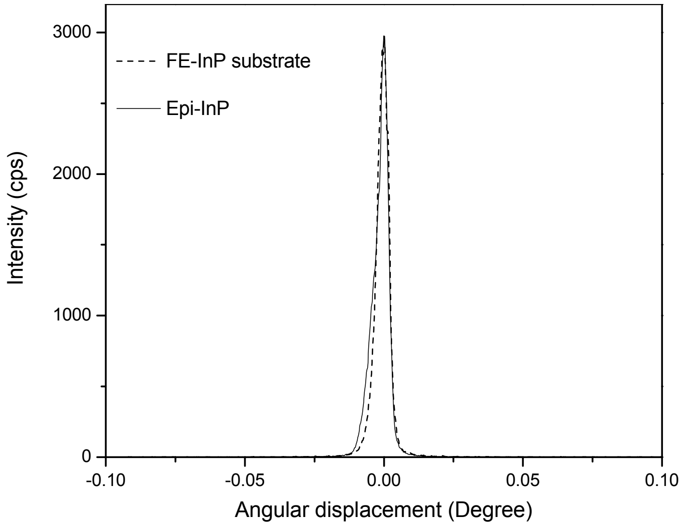

Figure 4.8: Comparison of XRD rocking curves on undoped InP epilayer and Fe doped InP substrate in MOCVD growth

The background doping of the InP epilayers grown by MOCVD has been investigated as a function of the V/III ratio during the growth. The Hall mobility and carrier concentration of the samples have been measured by Hall measurement. The InP epilayers grown with different V/III ratios were cut into 10mm×10mm squares, and Ohm contacts were made at four corners of the squares by using In-Sn alloy. The squares were then annealed for 5 minutes at 350 ^{o}C to improve their Ohm contacts. Nitrogen was introduced in alloy furnace during the annealing to prevent oxidization of the samples and metal contacts. The Hall measurement was carried out at room temperature and 77 K in liquid nitrogen.

Figure 4.9 shows the relationship between the measured Hall mobility of the InP epilayers grown versus the V/III ratios during the MOCVD growth. With increasing the V/III ratio during the MOCVD growth, the Hall mobility of the InP epilayers increases monotonically. Because MOCVD is not equilibrium epitaxial growth technique, stoichiometric control is based on the V/III ratio. Group-V vacancies are considered as the origin of deep levels. When the V/III ratio increases, the concentration of group-V vacancies decrease, therefore, the crystal quality is improved accordingly, and Hall mobility of the films increases. From the higher mobility data obtained, it seems autodoping (Dopant incorporated during the growth of an epitaxial layer from sources other than the dopant intentionally added to the vapor phase) does not play the major role.

Table 4.3 Hall measurement results of the InP epilayers grown with different V/III ratio

Sample ID	V/III	300 K		77 K	
		μ_H ($cm^{-2}V^{-1}s^{-1}$)	n (cm^{-3})*	μ_H ($cm^{-2}V^{-1}s^{-1}$)	n (cm^{-3})*
R20	49	2650	-1.51E+15	12400	-6.73E+14
R21	40	1400	-2.70E+15	1400	-3.18E+14
R23	64	4350	-1.10E+15	104000	-5.14E+14

* “-” indicate n-type concentration

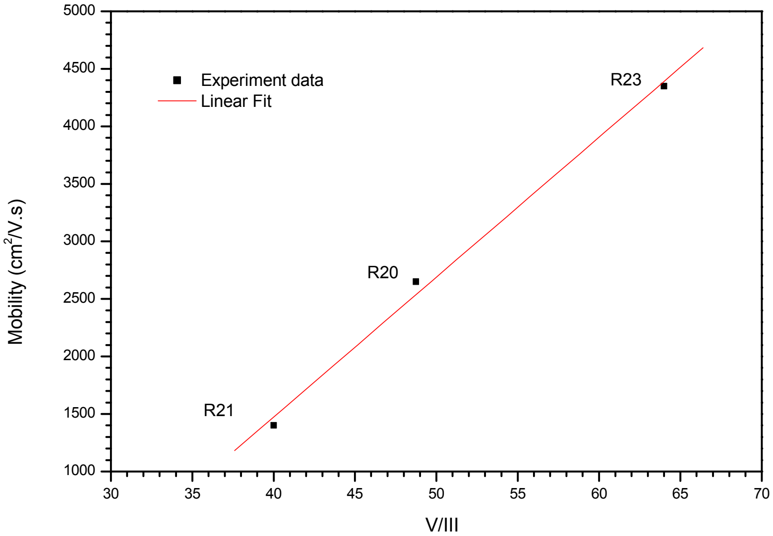

Figure 4.9: Measured room temperature Hall mobility of the undoped InP epilayer versus V/III ratio during the MOCVD growth.

The relationship between the growth rate of InP epilayer and the input of TMIn and TBP sources' flow during MOCVD growth has been investigated.

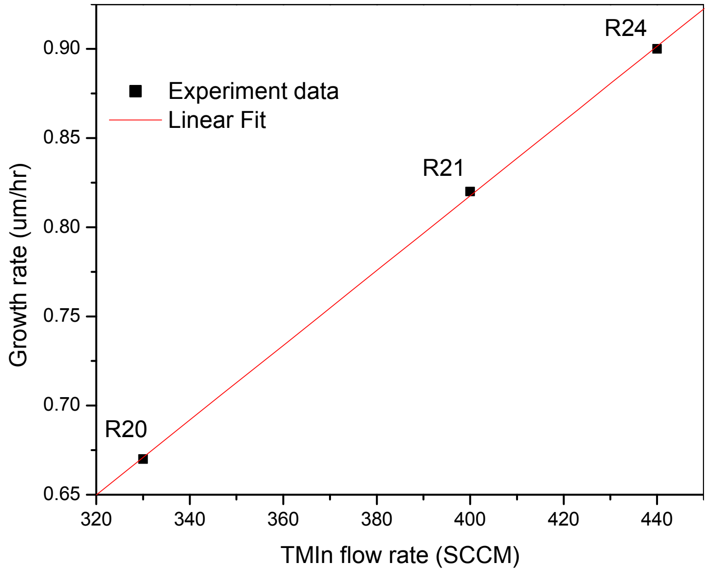

Figure 4.10: Variation of growth rate of InP with TMIn flow (TBP flow rate = 125 SCCM)

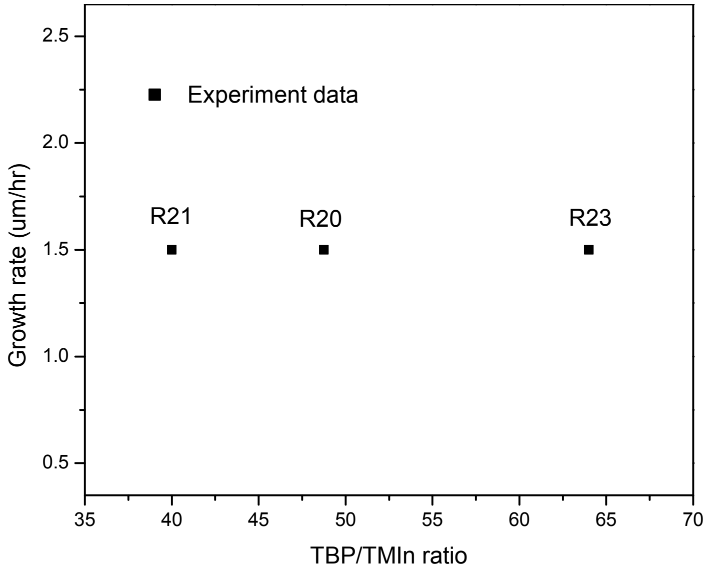

Figure 4.11: Variation of growth rate of InP with TBP flow rate (TMIn flow rate = 330 SCCM)

Figure 4.10 and Figure 4.11 show the growth rates versus the TMIn and TBP source flow, respectively. The substrate temperature of all the growth was set as 630 ^{o}C, the reactor pressure was kept at 100 mbar and the total gas flow in the reactor was set as 3500 SCCM.

As shown in Figure 4.10, the growth rate of InP epilayer increases linearly with the TMIn flow rate. However, the growth rate is independent on the flow rate of TBP. This suggests that the InP epitaxial growth rate is controlled by the mass transport of the group III species under these MOCVD growth conditions, which agrees with the published results [2].

4.4 Doping in InP epitaxial layer

Si and Zn are the common donor and acceptor dopants in MOCVD growth of III-V semiconductors, respectively. But due to smaller covalent radius of Si and Zn atoms compared with those of In and P, highly Si and Zn doped in InP epilayer may cause the InP epilayer lattice distortion. In this section, Si- and Zn-doped InP grown by MOCVD were investigated by using of ECV profiler. The doping effect on crystallographic and optical properties of InP epitaxial layers is studied using XRD and PL measurements.

4.4.1 N-type doping in InP growth

As mentioned earlier, Si is usually used as the N-type dopant in InP layers grown by MOCVD. In this project, N_2 diluted SiH_4 (2%) was employed to generate as the Si dopants. As SiH_4 has higher pyrolysis temperature, SiH_4 will be not completely decomposed at lower growth temperature. In order to get more efficient N-type doping in InP growth, the growth temperature was firstly set as 650^{o}C in this study. However, it was found that the surface of the samples became hazy even with lower SiH_4 flow rate. The growth temperature was then lowered to 630°C, the surface became smooth and mirror like. This may due to the homogeneous reaction between TBP and SiH_4 in gas phase before they are incorporated into the film. It is known that TBP starts to decompose at 350°C, and more than 90% of the TBP decomposed when the temperature is above 550°C [3]. Nearly 100% of input TBP should decompose when temperature is above 600°C. At high growth temperature, as long as SiH_4 is introduced into the reactor, extra-activated P will react with undecomposed SiH_4 to form adducts (which P atom is surrounded by SiH_4 molecules with weak bonds) in vapor phase. When these adducts diffuse through the boundary layer onto the sample surface, they will block happening of the further nuclei reaction. As a result, polycrystalline will be grown, and the surface of sample will thus be degraded.

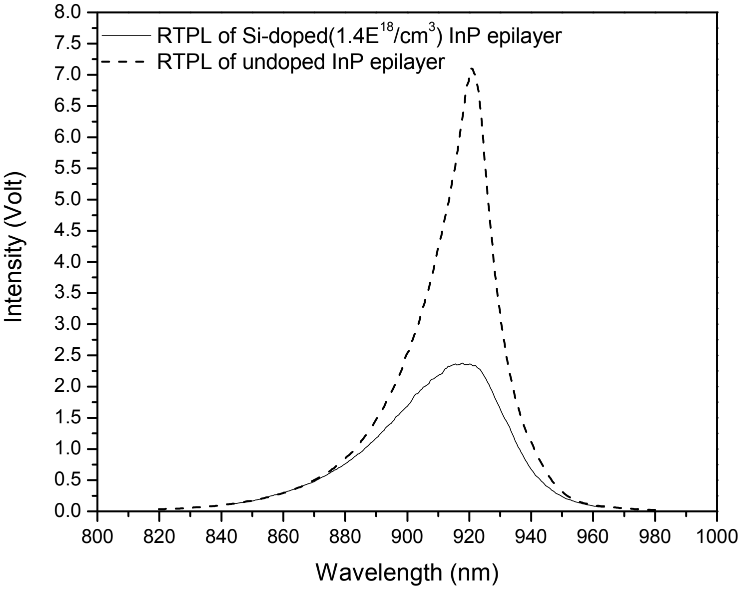

Figure 4.12: Comparison of room temperature PL spectrum on Si-doped InP epilayer and undoped InP epilayer

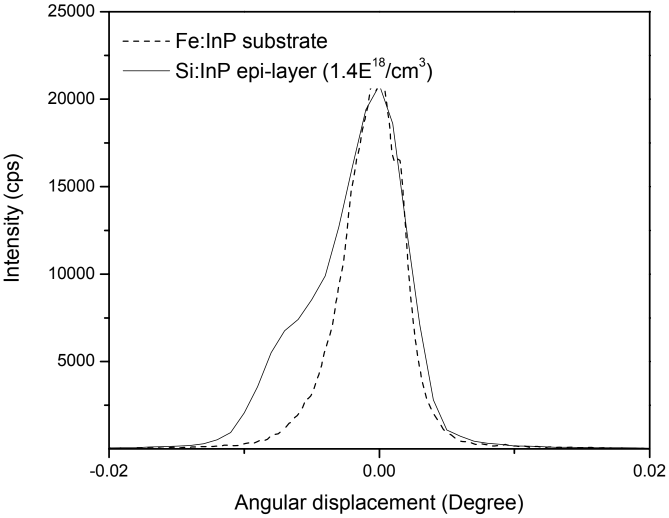

Figure 4.13: Comparison of XRD rocking curve on Si-doped InP epilayer and Fe-doped InP substrate

The PL and XRD measurement results of the n-type doped InP epilayers are shown in Figure 4.12 and Figure 4.13, respectively. Compared with that of the undoped InP epilayer, FWHM of the PL spectrum from the n-type doped InP sample is much broader (44nm). The reasons of this broadening may be attributed to: a) the band-to-donor transitions, b) composition fluctuation in the high Si-doped InP film. Lower intensity of the PL signal may due to free carrier absorption and the crystalline quality degradation with the Si doing.

In the XRD rocking curve of the Si-doped InP, there is a shoulder near the InP substrate peak, which means the lattice constant of the InP film is changed when highly doped with Si. It is known that high Si concentration incorporated into the InP epilayer may cause the lattice distortion in the InP epilayer. As Si has smaller atomic diameter than In and P atom, the crystal lattice constant of the InP layer should shrink when Si incorporates into InP layer as a substituent. Therefore, a XRD peak should be observed at larger angle side (right hand side). However, our observation is contrary to this prediction. The mechanism needs a further study.

To find out the relationship between the electron carrier concentration of Si-doped InP epilayer and the input vapor sources ratio (SiH_4/TMIn) used in MOCVD growth, a special Si-doped InP sample was grown. The sample consists of three layers with different doping concentrations. To grow this sample, different SiH_4 flow rates were set during MOCVD growth of the different layers, while TMIn and TBP sources flow rate and the growth temperature were kept unchanged. ECV measurement was carried out on to measure the carrier concentrations of each layer of the sample.

Figure 4.14 shows the measured doping profile of the sample. Good interfaces have been formed between the different layers as shown in Figure 4.14. Table 4.4 lists the SiH_4 dopant source flow ratio and measured electron carrier concentration for each layer.

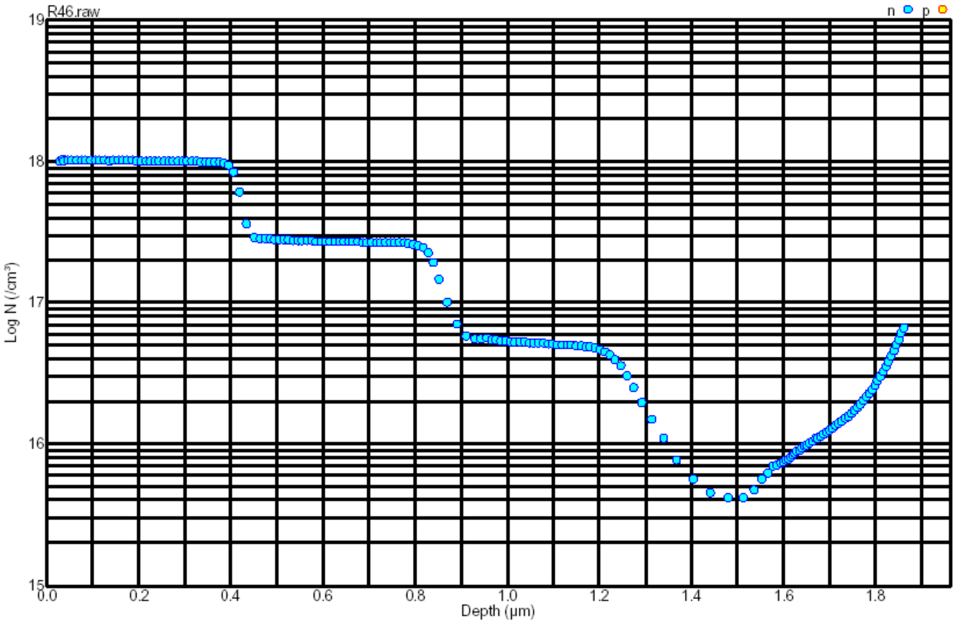

Figure 4.14: ECV profile of Si-doped InP epilayer

Table 4.4 Si dopant source flow ratio and measured carrier concentration of the InP MOCVD grown sample

Sample ID	Dopant/III	Dopant/V	Carrier Concentration (cm^{-3})
R46	8.75E-04	1.70E-05	5.20E+16
	6.19E-03	1.20E-04	2.70E+17
	5.57E-02	1.08E-03	1.00E+18

The measured electron carrier concentration in the MOCVD grown Si-doped InP eiplayer versus SiH_4/TMIn input source flow ratio is plotted in Figure 4.15. It shows that the electron carrier concentration seems to superlinearlly increase with the SiH_4 dopant source flow in MOCVD growth. This phenomena is due to the Si incorporation saturation at higher doping level.

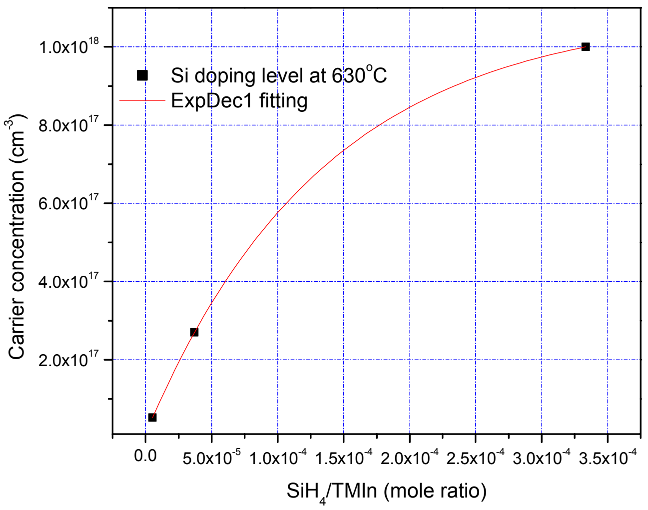

Figure 4.15: Correlation of Si doping level in InP growth between vapor ratio of SiH_4/TMIn

From Table 4.4, it can be seen that to reach the carrier concentration of $1x10^{18}$ cm^{-3}, SiH_4/III dopant source flow ratio was near 6%, this means that the doping incorporation efficiency (or Si activation) in the MOCVD growth was very low. The low cracking rate of SiH_4 is believed to be one reason causing the low doping efficiency. Another reason maybe due to the amphoteric nature of Si, auto-compensation effect may occur, because there is possibility that Si replaces P atom position instead of Indium position during the growth which reduces the N-doping efficiency. In this case, to reach higher Si doping level in InP epilayer, one way is to increase the growth temperature. At higher temperature, SiH_4 decomposition ratio will increase. However, if the growth temperature is too high, it will degrade the crystalline quality of the InP epilayer as mentioned before. The other way to increase the doping level is to reduce the growth rate of InP to improve the Si incorporation in the epilayer [5].

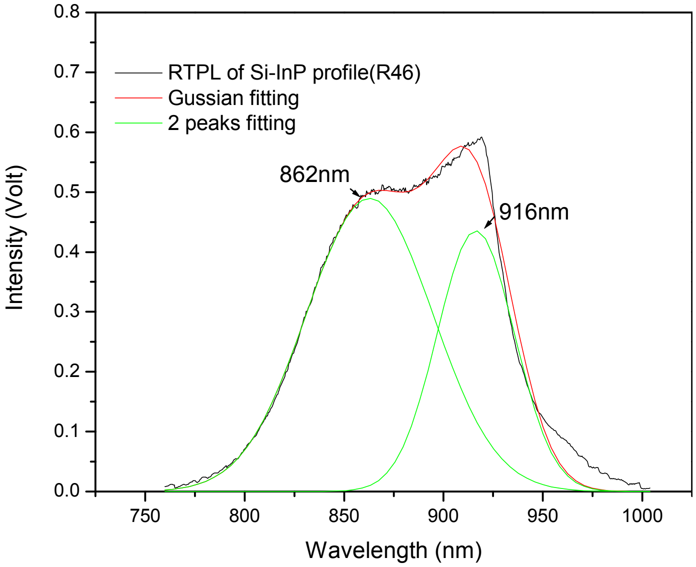

Figure 4.16: Room temperature PL spectrum of InP epilayer with profiled Si doping

Figure 4.16 and Figure 4.17 show the PL and XRD measurement results of the Si-doped InP epitaxial sample, respectively. A very broad PL spectrum is observed. Based on Guassian fitting analysis, 2 peaks appear at 916nm and 862nm. We may say that peak for 916nm comes from InP emission, while the possible source for 862nm emission is the high Si concentration in the sample. As mentioned above, high Si doping level in InP may change the composition of the alloy. And the Si has broader bandgap than that of InP, this may cause shorter PL emission wavelength.

The XRD measurement also shows a broad rocking curve. Lattice constant may changed by higher Si incorporation, so the XRD rocking curve is caused broader than substrate.

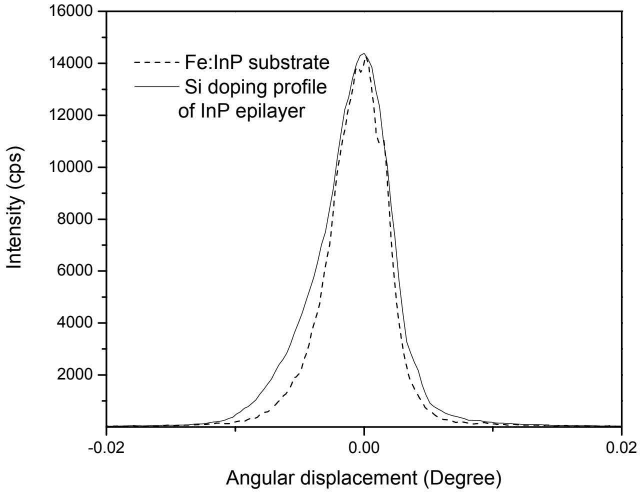

Figure 4.17: Comparison of XRD rocking curve on profiled-Si doped:InP epilayer and Fe: InP substrate

4.4.2 P-type doping in InP growth

Zn is usually used as the p-type dopant in MOCVD growth of InP epitaxial layers. In this project, diethylzinc (DEZn) was used to produce the Zn dopant source. It is known Zn has the disadvantage that it may diffuse at high doping level [4]. Since the Zn diffusion is critical to laser and other optoelectronic devices fabrications, a precise control of Zn-doping profile in device structure grown in MOCVD is important.

Zn diffusion in III-V materials affects the doping profile in the device structure, which has been studied by several groups [4-6]. During InP related material growth with Zn doping, interstitial Zn atoms move in the crystal and incorporate either on group III vacancies or in the site of an In atom due to existence of gradient Zn concentration. At an interface between Zn-doped and undoped layers, the Zn diffusion causes an intermixing on the Zn atom and group III sublattice there. Because of this interface mixing, it's very difficult to produce a sharp doping profile at the interface between a high level Zn-doped layer and an undoped InP layer. In this case, sharp interfaces between different doping levels in one sample can not be achieved.

Zn-doping profile in InP has been investigated in this project by growing Zn-doped InP epilayers with different DEZn source flow rates grown at 630 °C. At this growth temperature, good quality of Zn doped InP epilayers have been received. The doping level profile of the sample was measured and the result is shown in Figure 4.18.

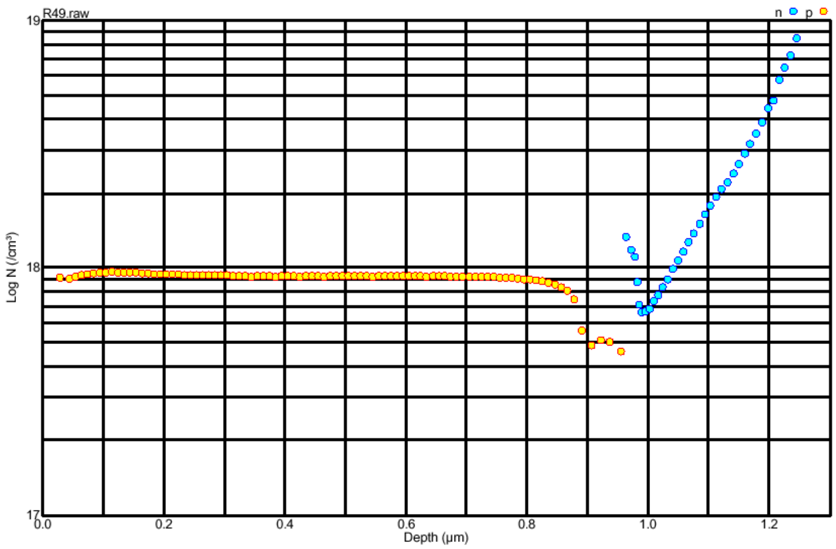

Figure 4.18: ECV profile of Zn:InP epilayer

Table 4.5 Experiment condition and results for DEZn doping in InP growth

Sample ID	Dopant/III	Dopant/V	Carrier Concentration (cm-3)
R47	0.016	3.02E-04	3.00E+17
R48	0.049	9.46E-04	7.70E+17
R49	0.062	1.21E-03	1.00E+18

Based on the measurement data of Table 4.5, the hole carrier concentrations in the Zn-doped InP epilayer versus the DEZn source flow rate in MOCVD growth is plotted in Figure 4.19. It shows that the hole carrier concentration in the Zn-doped InP epilayer increase linearly with the DEZn source flow rate. However, from the DEZn/III ratio versus the measured hole concentration, it seems only a small fraction of Zn activated in the epilayer layer. This could be caused by the re-evaporation of Zn from the surface at high temperatures.

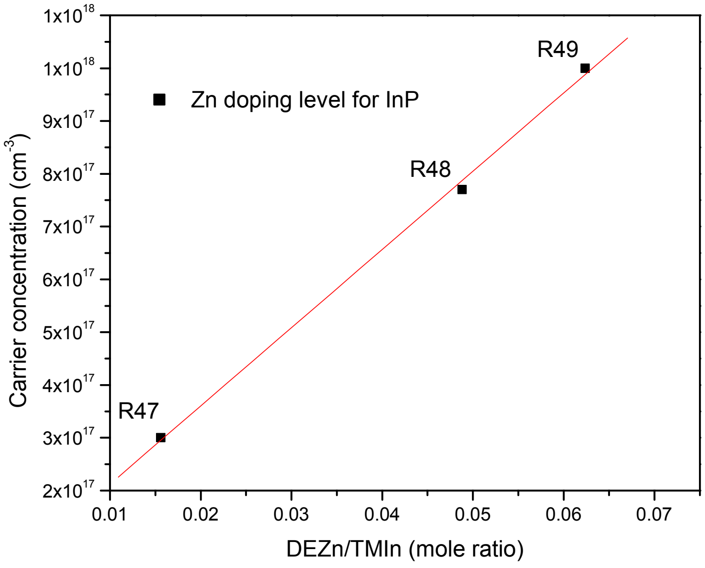

Figure 4.19: Relationship of Zn doping level in InP growth and vapor ratio of DEZn/TMIn

The optical emission properties of the Zn doped InP epilayer was investigated by Photoluminescence measurement. Figure 4.20 shows the PL emission spectra of the sample measured at room temperature. Compared with that measured from the undoped InP epilayer, the full-width at half-maximum (FWHM) of the PL spectrum of the Zn-doped InP epilayer is much wider. In the high Zn doping case, except for the substitutional site Zn atoms (active Zn), there are also a lot of the interstial site Zn atoms (inactive Zn) in the lattice. All these defects will distort the perfection of the lattice and therefore some additional electron states will be created near the bandedge. These states may expand to large range, which widen the FWHM of the PL emission.

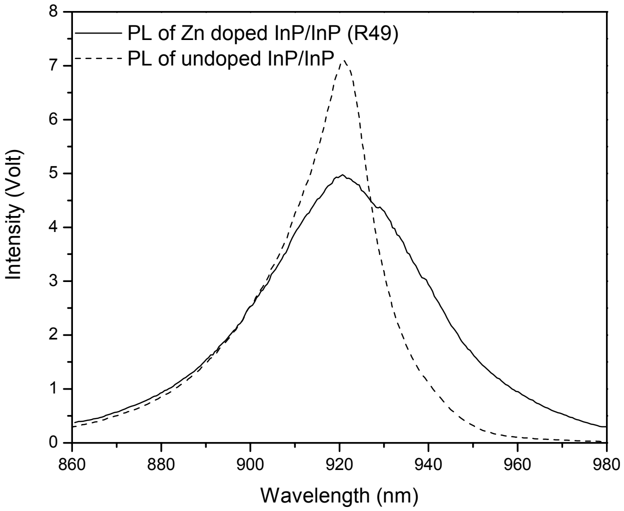

Figure 4.20: Comparison of room-temperature PL spectra from Zn-doped InP epilayer and undoped InP epilayer

The crystalline quality of the Zn-doped epilayer was checked by using XRD measurement. Figure 4.21 shows the XRD rocking curve of the Zn-doped InP epitaxy sample. The narrow XRD rocking curve shows very good crystal quality of the grown Zn-doped InP epilayer. The FWHM of XRD rocking curve for the Zn-doped epilayer is almost same as that of the Fe-doped InP substrate. There is no broadening of the FWHM as what happened in high level Si-doped InP epilayer, which shows that the Zn concentration level does not affect the InP epilayer's alloy composition.

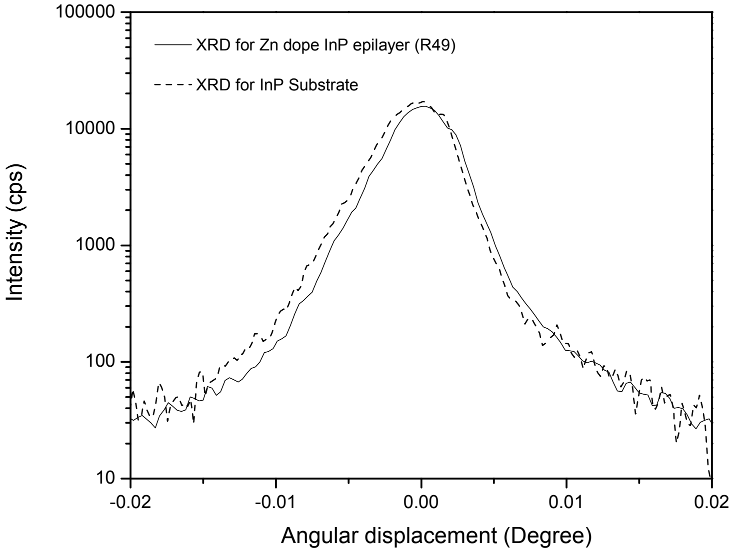

Figure 4.21: Comparison of XRD rocking curve of Zn-doped InP epilayer and Fe-doped InP substrate

4.5 Summary

The growth conditions for InP epilayer growth on InP substrate with MOCVD have been developed and optimized. Under properly distribution of the source flow in the reactor and purge liner, InP epilayer with good uniformity has been grown. XRD and PL results show good quality of the grown InP epilayer.

It has been found that the growth rate of InP increases linearly with the group III (TMIn) source input at the growth temperature of 630 ^{o}C. It shows that at this growth temperature the growth rate is dominated by mass transport in the MOCVD reactor.

The Hall measurement shows the background doping in an undoped InP epilayer decreases while Hall mobility increases with increasing the V/III ratio.

The N-type InP epilayers grown on InP substrate have been studied by using SiH_4 as Si dopant at different growth temperatures. It was found that the surface morphology of the epilayer degraded when SiH_4 was introduced at higher growth temperature. It may be attributed to the formed adduct by TBP and SiH_4 at high growth temperature (>650 ^{o}C). When the adducts diffuse onto the sample surface, it blocks the further nucleate reaction, which causes the surface morphology degradation. The XRD measurements also show that for the high-level Si doped InP epilayer, the lattice of Si-doped InP distorted and the composition of the epilayer may be changed. The correlation between electron carrier concentration in the Si-doped InP epilayer and the vapor phase input of SiH_4 in MOCVD growth has been explored. The low doping incorporation efficiency at high SiH_4 flow rate in MOCVD growth may be due to the auto-compensated doping of Si.

The relationship between DEZn source input and the measured hole carrier concentration in Zn-doped InP epilayer has been explored. The FWHM of PL spectrum from Zn-doped epilayer is broader than that of undoped InP epilayer. This may be due to Zn doping generating additional electron states, which expand to large range causing spectrum broader. The XRD measurement was carried on Zn doped InP epilayer, high Zn concentration does not affect the crystal quality.

Chapter 5 MOCVD growths of InGaAs bulk materials

5.1 Introduction

Epitaxy growth of InGaAs on InP substrate is very important for optoelectronic and electrical device fabrications. The room-temperature emission wavelength of InGaAs/InP quantum well structures can be designed to change from 1.6 μm to 1.1 μm, which is important in low loss optical fiber communications. Lattice mismatch between InGaAs and InP is a critical issue in MOCVD growth of InGaAs/InP system.

In this chapter, MOCVD growth of InGaAs on InP by using TBAs in N_2 ambient is investigated and the growth conditions are optimized. With XRD and PL measurement, crystal quality and optical properties of the InGaAs/InP epilayers has been evaluated.

5.2 MOCVD growth of InGaAs/InP

In the MOCVD growths, the InGaAs layers were grown on epi-ready semi-insulating (Fe-doped) InP (100) substrates. The reactor pressure was kept at 100mbar. Total gas flow rate in the liner and liner purge was set at 3500 SCCM and 500 SCCM, respectively. The V/III ratio of the source flow was chosen around 20 (for InGaAs epilayer). The growth temperature profile during the process is schematically shown in Figure 5.1.

To prevent thermal decomposition of InP substrates during heating up process in the MOCVD growths, TBP source was introduced into the reactor when the substrate temperature raised above 300^{o}C.

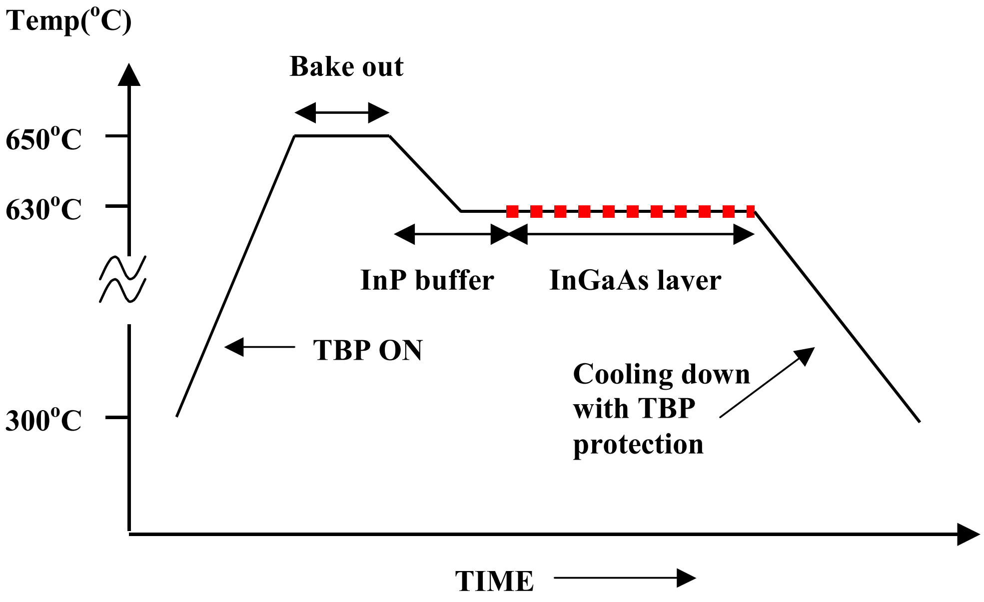

Figure 5.1: Scheme of temperature profile for growth of InGaAs in the MOCVD process

Prior to epitaxy growth, the wafer was annealed in TBP ambient for 5 minutes at 650°C to remove the residue oxidize layer on InP substrate surface. A 200 nm InP buffer layer was grown on the substrate with the temperature ramping down from 650°C to 630°C before growing the InGaAs layer. The V/III ratio was set as 60 for the growth of the buffer layer. During the buffer layer growth, most of the impurities from the ambient would be absorbed and the buffer layer covered the defects or damages on the surface of the substrate, creating a very good surface for succeeding epilayer structures growth. Another 100 nm InP layer was then grown on the previous InP buffer layer to improve the surface quality at temperature of 630°C. The TMIn source flow to the reactor was switched off when the InP buffer growth completed. Then, TBP was switched off and TMIn, TMGa and TBAs were introduced in the reactor at same time to start growing the InGaAs epilayer. Under these growth conditions, approximately a 450 nm thick InGaAs layer was grown for 20 minutes. The TMIn and TMGa source flows to reactor were switched off simultaneously to terminate the InGaAs layer growth. During the cooling down process, TBAs source was kept to flow into the reactor until the substrate temperature below 300°C.

5.3 Characterization of InGaAs/InP

Lattice mismatch between InGaAs epilayer and the InP substrate is the main concern in InGaAs/InP growth. Following Vegard's rule, lattice constant of $In_{1-x}Ga_xAs$ ternary alloy can be calculated based on that of GaAs and InAs [1][2], as Eq. 3.6 described:

$$a_{Ga_xIn_{1-x}As} = x \times a_{GaAs} + (1-x) \times a_{InAs} \ , \qquad (5.1)$$

where $a_{Ga_xIn_{1-x}As}$, a_{GaAs} , a_{InAs} are the lattice constants of InGaAs, GaAs, InAs respectively.

The lattice constant of $In_{1-x}Ga_xAs$ ternary alloy depends linearly on it's composition, x, as shown in Figure 5.2.

Based on Figure 5.2, it is found that when the Ga composition of the alloy, x, is 0.47 the lattice constant of $In_{1-x}Ga_xAs$ matches to that of InP substrate. If the lattice constant of the epilayer does not match to that of the substrate, strain will be generated in the epilayer. The strain due to the lattice mismatch between the epilayer and substrate leads to a tetragonal distortion of the epilayer's lattice in two directions: parallel to the interface and in the growth direction, and eventually incline the growth of the layer relative to the substrate surface with a misorientation angle α. Large mismatch causes the epilayer crystal lattice distortion and results in the strain relaxation in the epilayer. The crystal distortion will also affect electrical and optical properties of the epilayer [3].

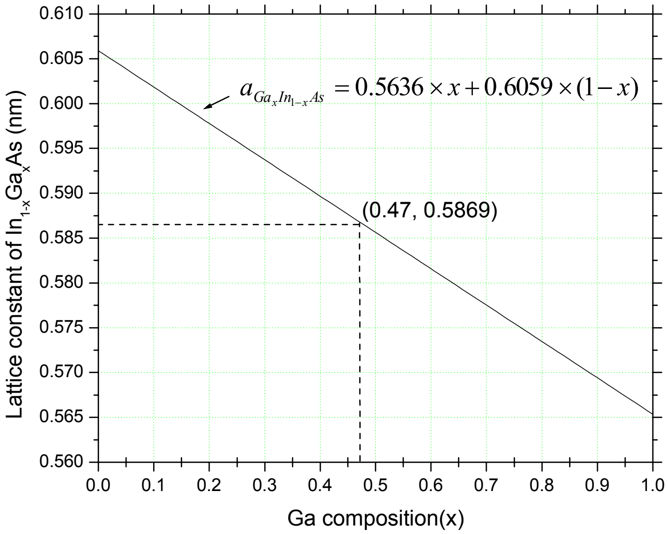

Figure 5.2: Ga composition dependence of InGaAs lattice constant.

To achieve lattice matched InGaAs/InP epilayer growth, the composition of InGaAs epilayer was controlled by adjusting the flow rate of TMGa while TBAs and TMIn flow rates were kept constant and the growth temperature unchanged. The lattice mismatch between the InGaAs epilayer and InP substrate of the samples was measured by using high resolution X-ray diffractometer (XRD). The XRD measurement yields the strain value of the lattice mismatch (for determination of lattice mismatch of pseudomorphic layers)

$$\frac{\Delta a}{a} = \frac{(a_{InGaAs} - a_{InP})}{a_{InP}} \tag{5.2}$$

by means of Eq. (3.10)

By measuring angular difference between the X-ray diffraction peak of the substrate and that of the epitaxial layer, *Δθ*, together with Eq. (3.10), the lattice mismatch can be determined. The experiment condition and XRD results are summarized in Table 5.1

Table 5.1 Sources' flow rate in MOCVD growth and the measured lattice mismatch of the samples

Run ID	TBA flow (mol/min)	TMGa/ TMGa+TMIn	Total III (mol/min)	V/III	Mismatch (ppm)
R88	2.23E-03	3.99E-01	9.99E-04	22	-4045
R99	2.23E-03	2.90E-01	8.47E-05	26	2669
R104	2.23E-03	3.55E-01	9.33E-05	24	-897
R105	2.23E-03	3.47E-01	9.20E-05	24	-539
R107	2.23E-03	3.33E-01	9.04E-05	24.7	98

The variation of lattice mismatch between the grown InGaAs epilayer and InP substrate versus the TMGa/(TMGa+TMIn) source flow ratio in the MOCVD growths is plotted in Figure 5.3.

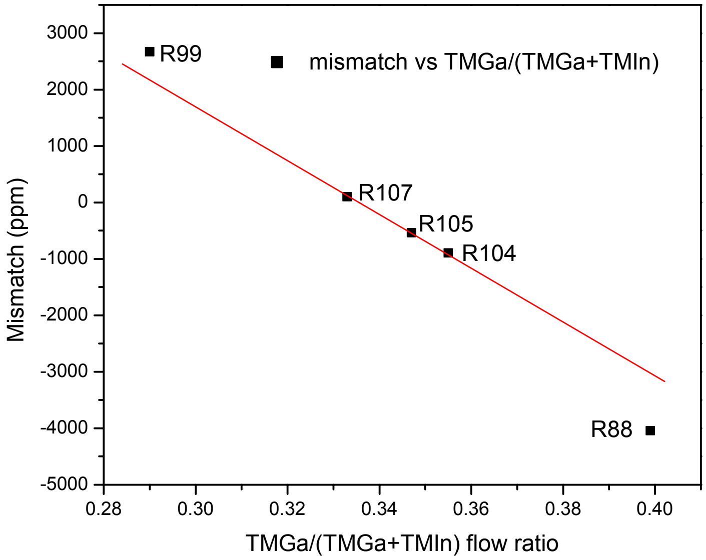

Figure 5.3: Variation of mismatch by changing TMGa/(TMGa+TMIn) flow ratio

It is found that the lattice mismatch changes linearly with the input source flow ratio TMGa/(TMGa+TMIn) in small mismatch range (less than 1000 ppm). This agrees with Vegard's rule. As discussed in Chapter 3, XRD measurement and the calculation are only for determining the lattice mismatch of pseudomorphic layers. So the calculation results for relaxed layers from XRD software are not accurate due to the lattice constant difference between the epilayer and substrate in the parallel direction of the interface.

Figure 5.4 shows the correlation between the critical thickness of the InGaAs epilayer grown on InP substrate and the lattice mismatch. It shows that sample R99 and R88 are not in strained status but partially or fully relaxed at 450 nm thickness.

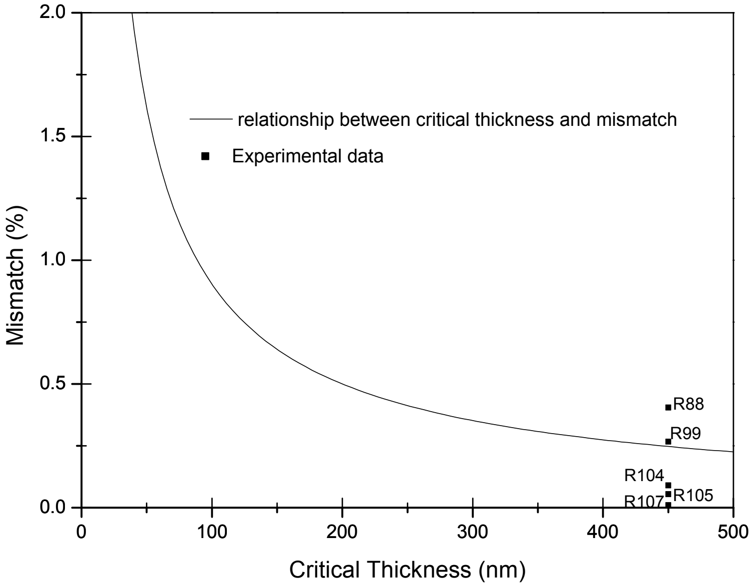

Figure 5.4: Critical thickness varies with lattice mismatch

According to this calculation and experiment data, a 450 nm InGaAs epilayer grown on InP substrates, the lattice mismatch between the epilayer and substrate must be less than 0.25% to ensure a perfect crystalline of the grown epilayer.

Based on the XRD measurement results, the correlation between the Ga composition in InGaAs films and the input vapor source flow ratio TMGa/(TMGa+TMIn) was evaluated. The results are plotted in Figure 5.5. It is found that Ga composition of the epilayers increases linearly with the vapour input ratio of TMGa/(TMGa+TMIn). This result shows that at this growth temperature TMIn and TMGa are decomposed completely.

The growth process was in the mass transport limited region as described in chapter 3, when In and Ga incorporation rate is constant. This explains Ga incorporation increases linearly with the TMGa flow rate as TMIn flow rate kept constant.

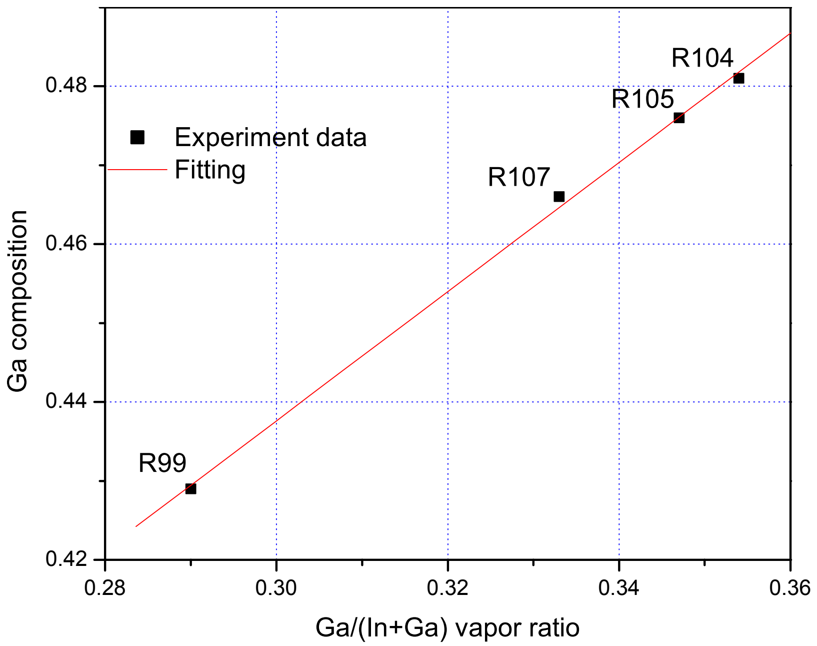

Figure 5.5: Correlation between Ga composition in InGaAs and vapor input ratio of TMGa/(TMGa+TMIn)

A linear relationship between the Ga composition in InGaAs films and the input vapor source flow ratio of TMGa/(TMGa+TMIn) makes it easy to control the Ga composition in MOCVD growth of InGaAs on InP substrate.

XRD measurement of the sample R88 shows large tensile strain (Ga-rich) in the epilayer as shown in Figure 5.6. The surface of the sample is very rough as shown Figure 5.7. For sample R99, the measurement shows compressive strain (In-rich) of the epilayer. The sample surface is smooth but is with dislocation lines parallel and perpendicular to wafer orientation flat as shown in Figure 5.9.

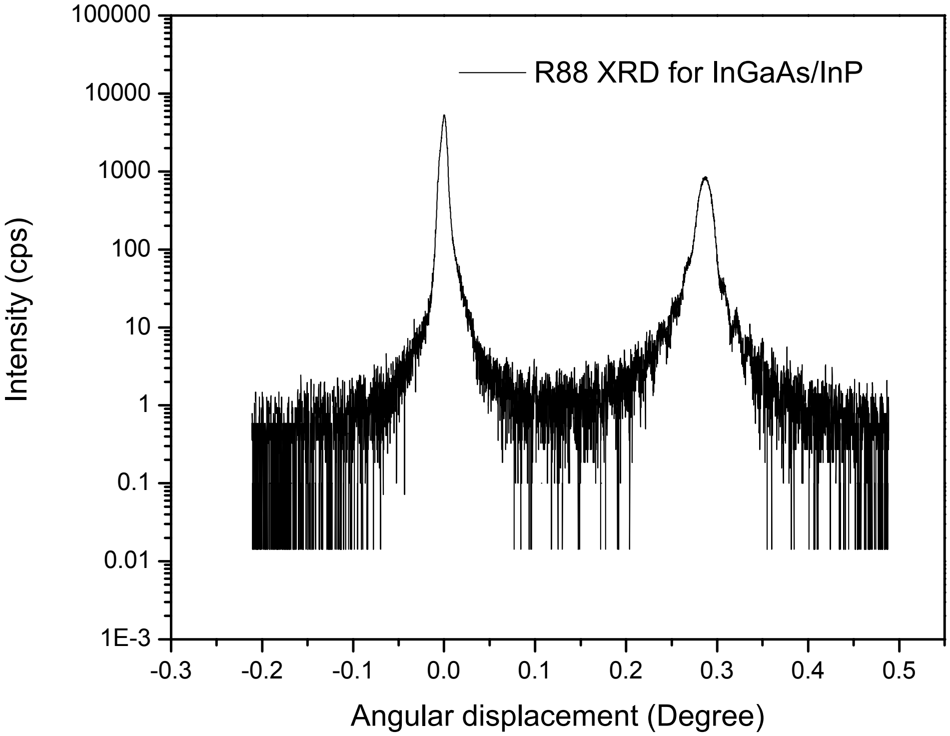

Figure 5.6: XRD rocking curve of InGaAs/InP with large tensile strain

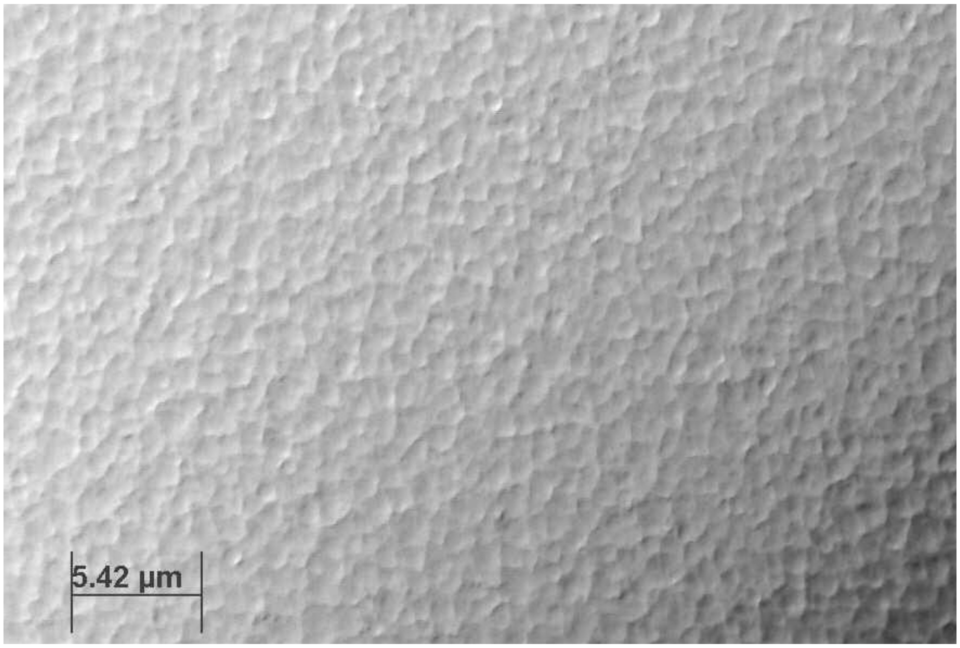

Figure 5.7: Surface photograph of InGaAs/InP (R88) with large tensile strain (Ga-rich)

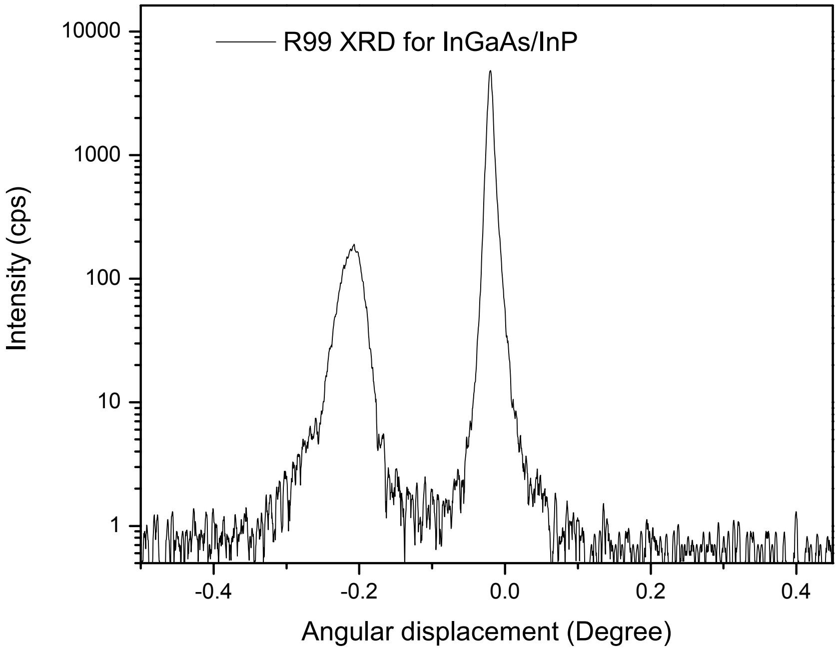

Figure 5.8:XRD rocking curve of InGaAs/InP sample (R99) with large compressive strain (In-rich)

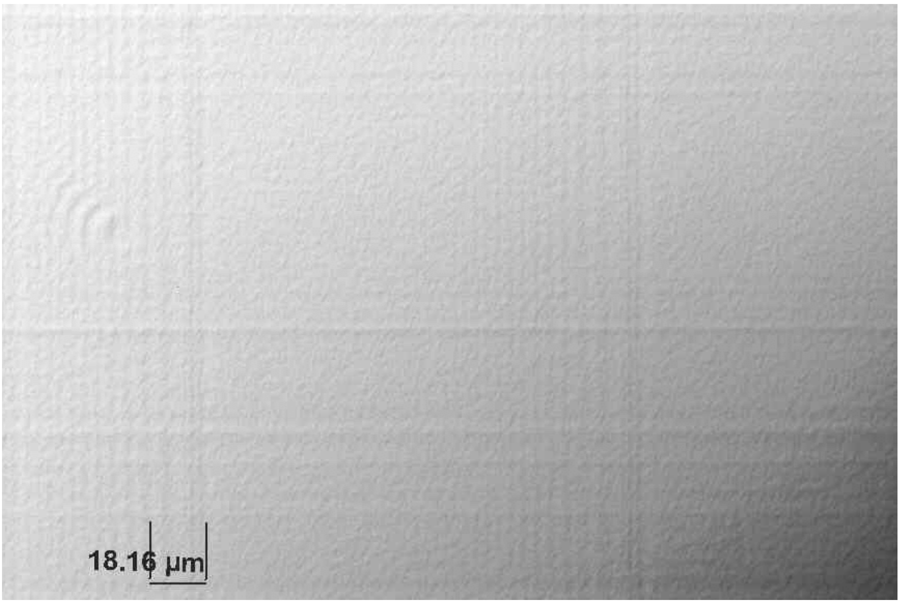

Figure 5.9: Surface photograph of InGaAs/InP (R99) with large compressive strain (In-rich)

Cross-hatching is observed on R99 (Figure 5.9), it is indicative of the formation of misfit dislocations. For sample R88 listed in table 5.1, the lattice mismatch is determined to be about 0.4% from the XRD measurement. The lattice mismatch introduces a large amount of strain in the films. Since the thickness of epilayer grown is much beyond the critical thickness, the large mismatch causes the strain built in the epilayer to totally relax, which means that the large amount of dislocations generated in InGaAs. With the poor surface condition, following three-dimensional (3D) islands start to form when the InGaAs layer growth continued, very rough surface morphology is attained.

The optical property of the samples was investigated by using PL measurement. Figure 5.10 shows the PL spectrum of the two samples, R88 (Ga-rich sample with high tensile strain 4045 ppm) and R99 (In-rich with high compressive stain 2669 ppm). Sample R88 shows a broad FWHM of 151 nm. The main reason is due to poor crystal quality revealed from the rough surface image and strong strain relaxation. This surface undulation is to be accompanied by strong composition modulation inside epilayer to reduce the total strain energy [3]. These nonunifomity in terms of local composition and strain will cause different emission energy, reflected by the broadening PL spectrum, even structured spectrum shape as seen in Figure 5.10.

Comparably, sample R99 was smaller mismatch with InP substrate. It has smoother surface and better crystal quality. Partially relaxation only occurs dislocation line of the film. No composition variation caused in the epilayer. Therefore, the FWHM of the PL spectrum of the sample is 15 nm narrower than that of R88.

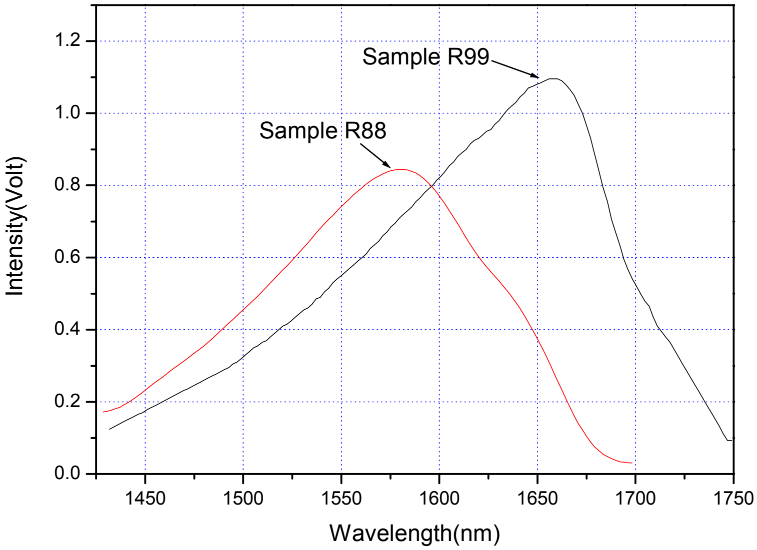

Figure 5.10: Room-temperature PL spectrum of InGaAs/InP (R88 with Ga-rich composition and R99 In-rich composition)

Because of the linear relationship between the epilayer lattice mismatch and the TMGa/TMIn flow ratio (Figure 5.3), it is not difficult to achieve lattice matched InGaAs epilayer grown on InP substrate by tuning the TMGa/TMIn flow ratio in MOCVD growth. Figure 5.11 shows the XRD results of a well lattice matched InGaAs epilayer (R107) grown on InP substrate.

The lattice mismatch between the grown InGaAs epilayer and InP substrate of the sample is only ~98 ppm, which can be considered as perfect lattice matched. The strong fringes of the XRD rocking curve of the sample show very good interface of the epilayer, and the narrow FWHM (86 arcsec) of the curve reflects high quality of epilayer. Room temperature PL spectrum of the sample is shown in Figure 5.12. The emission peak is at 1651 nm, which is almost equal to the theoretical calculation value (1650 nm) according to the epilayer's composition. The long "tail" toward shorter wavelengths of PL spectrum is due to the distribution of electrons and holes in the conduction and valence bands.

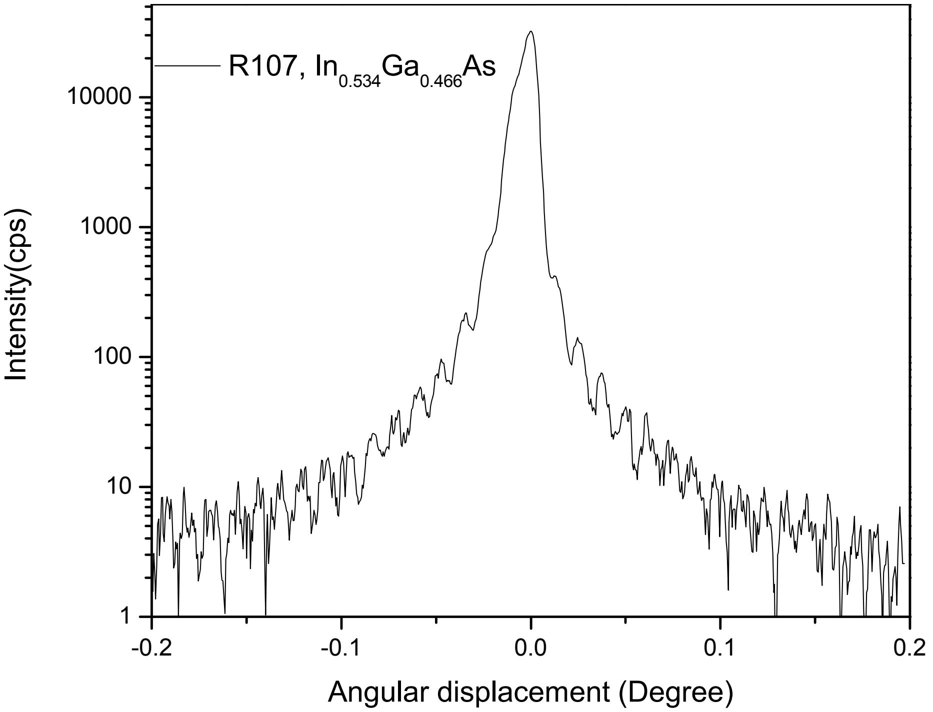

Figure 5.11: XRD rocking curve of sample R107

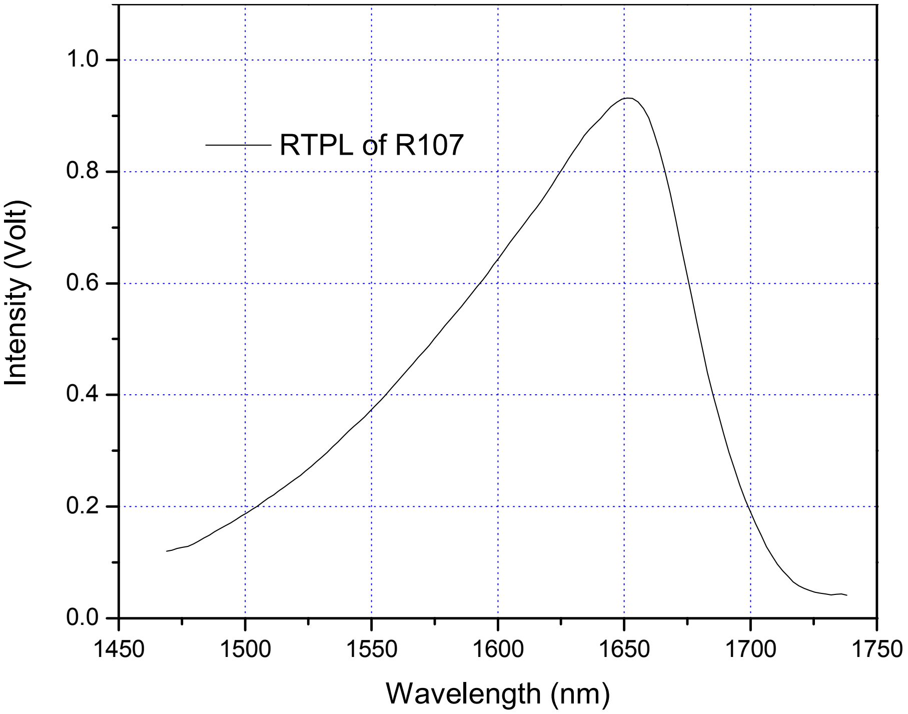

Figure 5.12: Room temperature PL spectrum of sample R107

Several $In_{1-x}Ga_xAs$ samples with small lattice mismatch have been grown. The room temperature PL and XRD results of samples are shown in Table 5.2. The composition of Ga calculated by Eq 5.2 and the composition dependence in Figure 5.2. It can be seen that less mismatch $In_{1-x}Ga_xAs$ film reflect better crystal quality, which has narrower PL FWHM.

Table 5.2 RTPL and XRD results of small lattice matched InGaAs on InP substrate

Sample ID	TMGa/ (TMGa+TMIn)	Mismatch (ppm)	Ga(x) Composition	RTPL (nm)	PL-FWHM (nm)
R104	0.354	-897	0.480	1640	131
R105	0.347	-539	0.476	1645	125
R107	0.335	98	0.466	1651	115

5.4 Summary

Using the optimized growth conditions, $In_{1-x}Ga_xAs$ films with different composition, *x*, were grown on InP substrates by MOCVD. Ga composition of the $In_{1-x}Ga_xAs$ epilayer grown was measured using XRD. The relationship between the solid composition of the epilayer versus input source flow ratio TMGa/(TMG+TMIn) in MOCVD growth has been investigated. For the lattice mismatch below 1000 ppm, the lattice mismatch between the epilayer and InP substrate changes linearly with the vapor phase input ratio TMGa/(TMGa+TMIn) in MOCVD growths. By reducing the mismatch of the epilayer, the crystal quality of epilayer could be improved.

Chapter 6 MOCVD growth of InGaAsP bulk materials

6.1 Introduction

The energy bangap of InGaAsP alloy with lattice matched to InP covers the range of 1.35 eV to 0.75eV. InP lattice matched InGaAsP alloys used as confinement layer as well as active layer makes the lasers emitting at 1.3 μm and 1.55 μm wavelength, which is very important in optical fiber communication. To grow high crystal quality $In_{1-x}Ga_xAs_yP_{1-y}$ epilayers on InP substrate, it is particularly crucial to control the compositions of the $In_{1-x}Ga_xAs_yP_{1-y}$ alloys precisely. The composition variations of $In_{1-x}Ga_xAs_yP_{1-y}$ alloys cause deviations in its lattice constant and energy bandgap, which will result in the mismatch dislocations in the $In_{1-x}Ga_xAs_yP_{1-y}$ epilayers grown on InP substrate. These dislocations in a laser's active layer will reduce the device's lifetime. Ideally, the lattice mismatch of the epilayers $\Delta a/a$ should be within $\pm$ 0.02%[1].

There are two important factors in LP-MOCVD growth of semiconductor quaternary alloy determine the epilayer's compositions: growth temperature and the effect of source chemistry on the wafer surface during the growth. In MOCVD growth of $In_{1-x}Ga_xAs_yP_{1-y}$, group III precursors, TMGa and TMIn, control the stoichiometry on the group III sites in a grown layer with tight bounds, even though only a portion (10%-50%) of the group III reactants are incorporated into the grown film. The thermal decomposition temperatures for group V precursors, e.g. TBAs and TBP, are normally lower than that for their group III hydride counterparts. This is beneficial to control the composition of quaternary epilayer grown. In this work, the MOCVD growth of the $In_{1-x}Ga_xAs_yP_{1-y}$ quaternary alloys were focused on their composition control.

For the $In_{1-x}Ga_xAs_yP_{1-y}$ quaternary alloy, its composition is determined by x, y. The composition dependence of the lattice constant and energy bandgap of the alloy satisfy the following equations [3][4][7]:

$$a_{In_{1-x}Ga_xAs_yP_{1-y}} = xya_{GaAs} + x(1-y)a_{GaP} + (1-x)ya_{InAs} + (1-x)(1-y)a_{InP} \tag{6.1}$$

$$\begin{aligned} E_g(In_{1-x}Ga_xAs_yP_{1-y}) &= 1.35 + 1.09x - y + 0.33x(1-y) \\ &+ (0.73 - 0.28y)x(1-x) - (0.101 + 1.109x)y + 0.05\sqrt{xy(1-x)(1-y)} \end{aligned} \tag{6.2}$$

where $a_{InGaAsP}$, a_{GaAs}, a_{GaP}, a_{InAs} and a_{InP} are the lattice constant of *InGaAsP*, *GaAs, GaP* , *InAs* and *InP* respectively.

In this project, MOCVD growth of the lattice matched to InP substrate $In_{1-x}Ga_xAs_yP_{1-y}$ alloys with the emission wavelengths from 1000 nm to 1400 nm were investigated by using TBP and TBAs as group V precursors in N_2 ambient. The relationship between the grown layer's composition and source flow during the MOCVD growth has been evaluated. XRD and PL were employed to characterize the grown $In_{1-x}Ga_xAs_yP_{1-y}$ layers' crystal and optical properties.

6.2 InGaAsP/InP Growth conditions

All the samples were grown on Fe-doped semi-insulating InP (100) substrate. The total gas flow rate in the reactor was set at 3500 SCCM which was optimized in InP MOCVD growth described before. The reactor pressure was fixed at 100 mbar. TBP was introduced in the reactor when the substrate temperature was raised above 300^{o}C and TBP source flow flux was kept at 250 SCCM. To completely remove the residue-oxidized layer on top of substrate before the epilayer growth, temperature was raised to 650 ^{o}C and kept at this temperature for 5 minutes. Temperature was then lowered to 630 ^{o}C to start the epitaxial growth. A 200 nm undoped InP buffer layer was grown on top of substrate to improve the surface quality. Following the buffer layer, a 500 nm $In_{1-x}Ga_xAs_yP_{1-y}$ layer was grown and then a thin InP cap layer was grown on top to prevent the epilayer surface degradation during cooling down after the growth.

The lattice constant control of the $In_{1-x}Ga_xAs_yP_{1-y}$ epilayer was studied by adjusting the TMGa/(TMGa+TMIn) flow ratio during the MOCVD growth, while the energy bandgap (e.g. emission wavelength) of the alloy was adjusted by changing the TBAs/(TBAs+TBP) flow ratio. In order to minimizing the variables in the growths conditions, $In_{1-x}Ga_xAs_yP_{1-y}$ layers were grown at 630^{o}C by keeping the TMIn and TBP source flow rate at 400 SCCM and 250 SCCM, respectively. TMGa and TBA source flow rates were adjusted to reach the composition target of the $In_{1-x}Ga_xAs_yP_{1-y}$ grown layers.

6.3 Composition control of $In_{1-x}Ga_xAs_yP_{1-y}$ epilayer

6.3.1 Ga composition of $In_{1-x}Ga_xAs_yP_{1-y}$ alloy

In this investigation, group V input ratio of the vapor phase TBAs/(TBAs+TBP) was kept at 0.066 unchanged while group III ratio TMGa/(TMGa+TMIn) was adjusted to change the Ga composition of the samples during the MOCVD growths. The grown samples were analyzed by using XRD and PL measurements. The growth conditions and XRD measurement results of the samples are shown in Table 6.1. Ga and As compositions of the samples were calculated based on XRD and PL results with Eq. (6.1) and (6.2).

Table 6.1 Growth conditions and Ga, As compositions of $In_{1-x}Ga_xAs_yP_{1-y}$ alloy grown from XRD measurement

Run No	TMGa/ (TMIn+TMGa)	TBA/ (TBA+TBP)	Mismatch (ppm)	Ga(x) Composition	As(y) Composition
R440	0.201	0.066	-1054.48	0.276	0.566
R441	0.177	0.066	940.8	0.215	0.495
R443	0.191	0.066	-239.12	0.250	0.577

Figure 6.1 shows the correlation between Ga composition and the vapour phase input ratio of TMGa/(TMGa+TMIn) in MOCVD growth. It was found that, Ga/In incorporation in the $In_{1-x}Ga_xAs_yP_{1-y}$ alloy changes linearly with the input TMGa/(TMIn+TMGa) vapor phase ratio at slope of 2.55, which means that the incorporation efficiency of TMGa is approximate 2.55 times higher than that of TMIn at this growth condition. In the MOCVD growth process, it is expected that both TMGa and TMIn have been decomposed completely, the lower incorporation efficiency of In may due to In atom has lower affinity and higher surface atomic mobility comparing Ga in the epitaxial growth at this growth temperature [9].

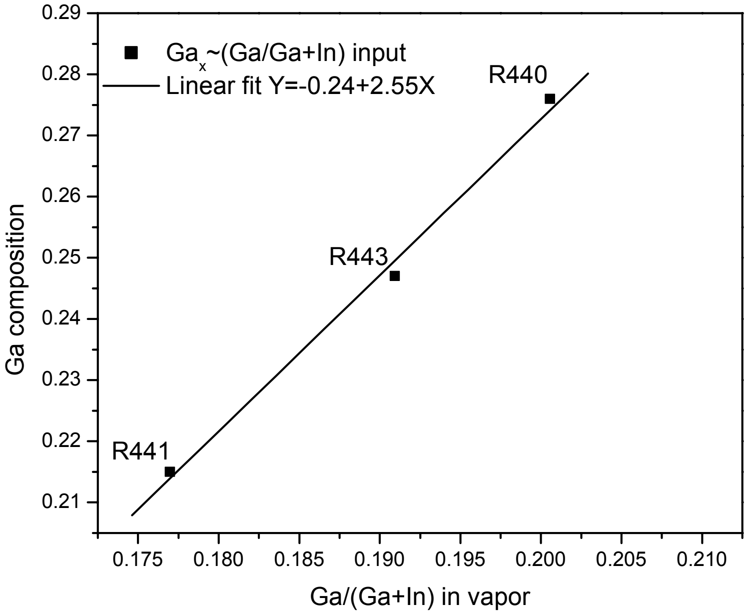

Figure 6.1: Ga composition of grown $In_{1-x}Ga_xAs_yP_{1-y}$ layers as the function of TMGa/(TMIn+TMGa) input vapor phase ratio in MOCVD growths (solid composition derive from XRD simulation), while TBAs/(TBAs+TBP) kept unchanged

To reveal the role of Ga composition in lattice mismatch, Eq. 6.1 is rewritten with parameter input ($a_{GaAs} = 5.6536\overset{0}{\mathrm{A}}, a_{GaP} = 5.4512\overset{0}{\mathrm{A}}, a_{InAs} = 6.0590\overset{0}{\mathrm{A}}, a_{InP} = 5.8696\overset{0}{\mathrm{A}}$):

$$\frac{\Delta a}{a} = \frac{0.1894y - 0.4184x + 0.0130xy}{5.8696} \qquad (6.3)$$

where Δa is the lattice constant difference between epilayer and substrate, a is the lattice constant of InP.

In Eq. (6.3), compared to x and y terms on the right hand side, the xy term can be neglected. The equation is mainly determined by the x and y terms. The equation also shows that the Ga composition (x) of $In_{1-x}Ga_xAs_yP_{1-y}$ epilayer is 2 times more sensitive than As composition (y) of $In_{1-x}Ga_xAs_yP_{1-y}$ layers grown. Therefore, Ga composition in $In_{1-x}Ga_xAs_yP_{1-y}$ film plays the major role in determining its lattice constant.

The experimental results also show that when TBAs/(TBAs+TBP) ratio was fixed in the growth, the lattice mismatch between InP substrate and the grown $In_{1-x}Ga_xAs_yP_{1-y}$ quaternary films changes linearly with TMGa/(TMIn+TMGa) ratio.

The XRD rocking curve results of the samples (Figure 6.2) show that when the group III vapor phase input ratio TMGa/(TMGa+TMIn) decreases from 0.276 to 0.215, the strain of the $In_{1-x}Ga_xAs_yP_{1-y}$ epilayers changes from tensile to compressive, which has been explored in Figure 6.3. It is because GaAs and GaP have smaller lattice constants compares with those of InAs and InP. When Ga composition decreases, the lattice constant of the quaternary alloy will increase. When the lattice constant of $In_{1-x}Ga_xAs_yP_{1-y}$ epilayer is larger than that of InP substrate, the strain of the film becomes compressive.

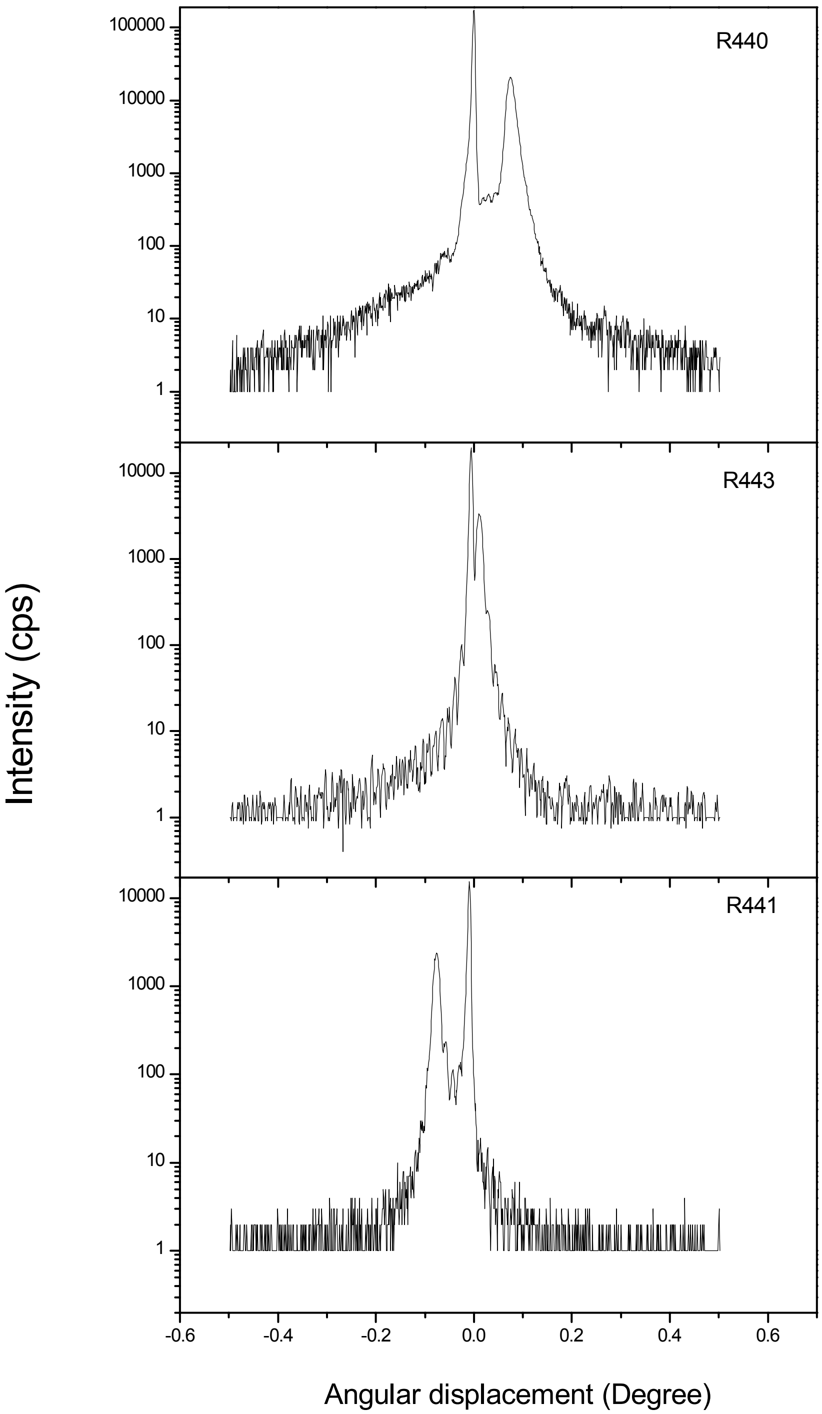

Figure 6.2: XRD rocking curve of sample R440, R441, R443

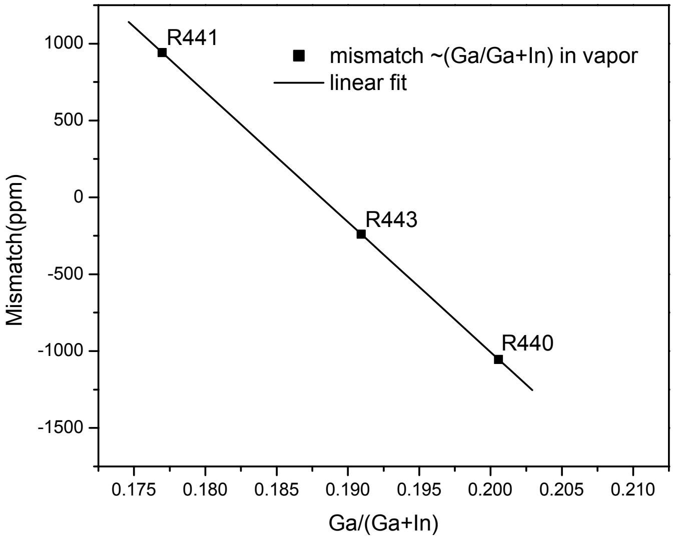

Figure 6.3: Lattice mismatch of $In_{1-x}Ga_xAs_yP_{1-y}$ layers grown as function of TMGa/(TMIn+TMGa) input vapor flow ratio while TBAs/(TBAs+TBP) keeps unchanged

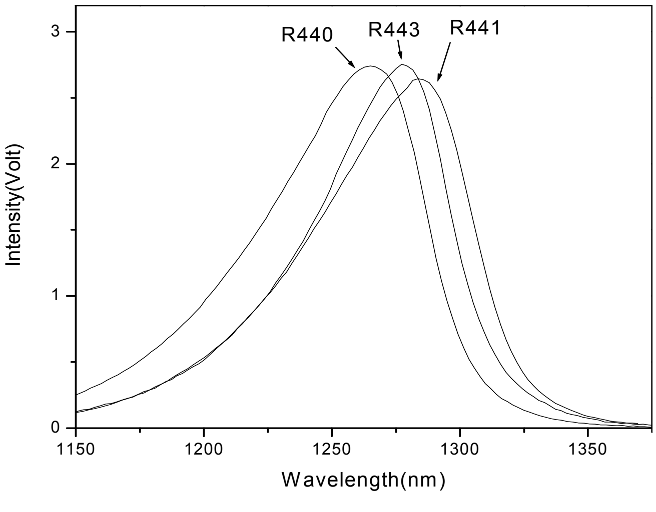

Figure 6.4: Room temperature PL spectra of sample R440, R443 and R441

It is observed (Figure 6.3) that when TMGa/(TMGa+TMIn) decreases from 0.200 to 0.175 during MOCVD growth, the lattice mismatch of the InGaAsP films changes linearly from –1054 ppm to 940 ppm. However, the PL peak wavelengths of the films (Table 6.2) do not change much (19 nm) as shown in Figure 6.4. This indicates that TMGa/(TMGa+TMIn) does not play a major role in determining the bandgap of $In_{1-x}Ga_xAs_yP_{1-y}$ films grown, which will be explained in the next part.

Table 6.2 Growth condition and room temperature PL measurement of $In_{1-x}Ga_xAs_yP_{1-y}$ alloy grown

Run No	TMGa/ (TMIn+TMGa)	TBAs/ (TBAs+TBP)	RTPL (nm)	FWHM (nm)
R440	0.201	0.066	1265	73
R441	0.177	0.066	1284	71
R443	0.191	0.066	1278	64

When the lattice mismatch between the $In_{1-x}Ga_xAs_yP_{1-y}$ epilayer and the substrate reduces, the interface between the epilayers and substrate is improved. This can be seen from the XRD rocking curves in Figure 6.2. Sample R443, which is the best lattice matched to InP substrate, shows clear fringes in its XRD rocking curve. And it has narrow FWHM (44 arcsec) compared to R440 (59 arcsec) and R441 (46 arcsec), which represent better crystal quality.

The PL results also show that large lattice mismatch of the $In_{1-x}Ga_xAs_yP_{1-y}$ epilayers leads to a broadening of the PL emission spectrum (table 6.2). Considering that the mismatch of all the samples are small enough and the epilayers are well controlled below the critical thickness, this slightly PL broadening does not suggest poor quality of strained samples.

6.3.2 As composition of $In_{1-x}Ga_xAs_yP_{1-y}$ alloy

Based on the previous study, it has been found that the TMGa/(TMGa+TMIn) ratio in MOCVD growth mainly affects the lattice constant of InGaAsP films grown, it does not affect the grown films' PL emission wavelength much. In this section, effect of TBAs/(TBAs+TBP) ratio on the grown $In_{1-x}Ga_xAs_yP_{1-y}$ epilayer's composition will be investigated. Two runs were carried out with fixed TMGa/(TMGa+TMIn) ratio, near the lattice-matched condition, to investigate the effect of the group V sources' effect on the bandgap of $In_{1-x}Ga_xAs_yP_{1-y}$ epilayer in MOCVD growths . Table 6.3 summarizes the measured results.

Table 6.3 PL and XRD results of grown $In_{1-x}Ga_xAs_yP_{1-y}$ epilayer versus TBAs flow

Run No	TMGa/ TMGa+TMIn	TBAs/ TBAs+TBP	RTPL (nm)	FWHM (nm)	Mismatch (ppm)	Ga(x) composition	As(y) composition
R447	0.242	0.11	1353	84	-321	0.319	0.679
R448	0.242	0.12	1382	86	314	0.321	0.702

It shows that with small changes of input group V vapor phase ratio TBAs/(TBAs+TBP) about 0.010, the PL emission wavelength of the film grown shifts about 29 nm. Compared with the result obtained by changing the group III source flow in MOCVD growth, the wavelength only changes 19 nm when TMGa/(TMGa+TMIn) ratio changes 0.024. This suggests that the energy band-gap of $In_{1-x}Ga_xAs_yP_{1-y}$ is more sensitive to its As composition y. This result agrees with the empirical expression of bandgap for $In_{1-x}Ga_xAs_yP_{1-y}$ that is matched on InP [8]:

$$E_g(InGaAsP) = 1.35 - 0.72y + 0.12y^2 \tag{6.4}$$

Figure 6.5 and Figure 6.6 show the PL measurement results and XRD rocking curves of these two samples grown by changing the input vapor phase ratio TBAs/(TBAs+TBP).

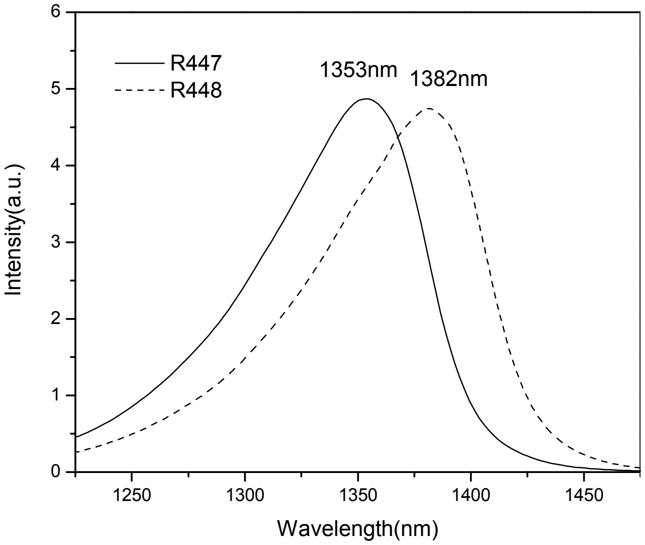

Figure 6.5: Room-temperature PL spectra of sample R447 and R448

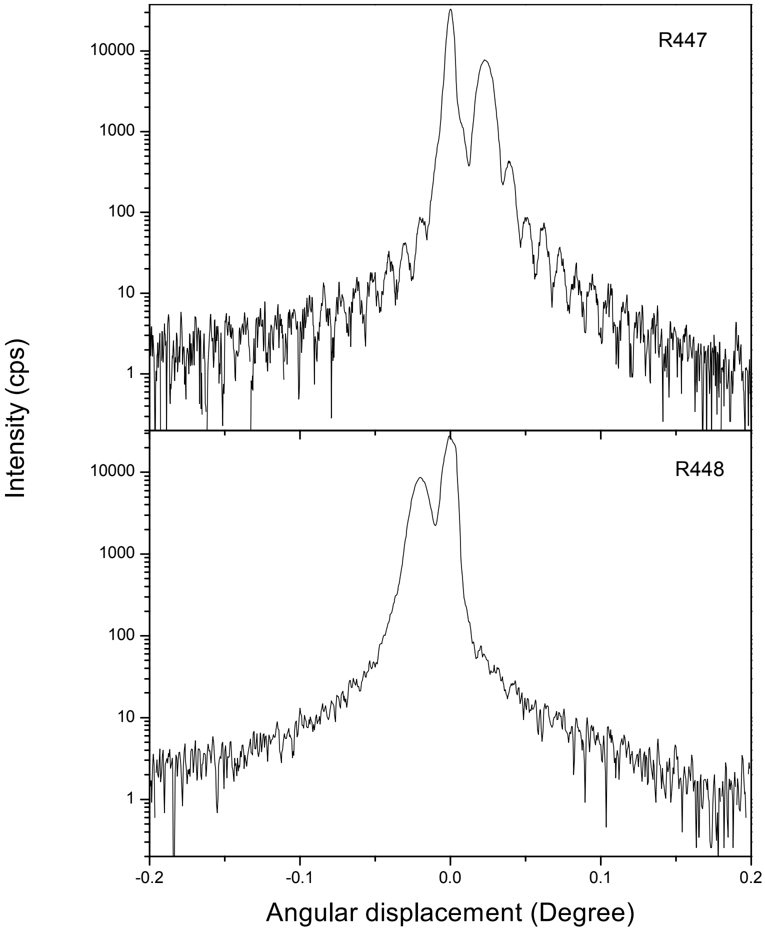

Figure 6.6: XRD rocking curves of sample R447 and R448 for the (004) reflection

The PL results of samples show little change for the intensity as well as FWHM while changing the TBAs/(TBAs+TBP) ratio. FWHM are quiet narrow for both samples at these wavelengths, which reflect good quality of the materials. Also, the XRD rocking curves (Figure 6.6) of the two samples show very strong interference fringes and very narrow FWHM (38 arcsec for R447 and 43 arcsec for R448). It indicates that the crystal quality of the InGaAsP/InP films and the interface between the layers of the samples are good.

Although TMGa/(TMGa+TMIn) ratio mainly contribute to the epilayer's lattice constant mismatch while TBAs/(TBAs+TBP) ratio mainly contribute to its emission wavelength, to achieve perfect lattice matched $In_{1-x}Ga_xAs_yP_{1-y}$ film, the effect of the input TBAs/(TBAs+TBP) ratio on the lattice constant can not be ignored [5][6]. Comparing the room temperature PL results of these samples, the emission wavelength of the sample shifts to longer wavelength when the gas flow ratio TBAs/(TBAs+TBP) increases during MOCVD growth. At the same time, XRD measurements also show that the lattice constant slightly changes when the TBAs/(TBAs+TBP) ratio changes. In this project, to grow good quality $In_{1-x}Ga_xAs_yP_{1-y}$ film with desired PL emission wavelength, TMGa/(TMGa+TMIn) ratio was adjusted to get lattice matched films on InP substrate to compensate the lattice mismatch caused by changing group V source input during the MOCVD growth.

Table 6.4 Experimental results focusing on changes of room temperature PL

Run No	Vapuor input of Ga/Ga+In	Vapour input of As/As+P	Wavelength (nm)	Mismatch (ppm)	Ga(x) composition	As(y) composition
R501	0.079	0.012	1055	58.95	0.110	0.243
R571	0.092	0.015	1078	-117.9	0.131	0.282
R582	0.108	0.019	1093	-837.09	0.153	0.308
R551	0.144	0.032	1164	-510.9	0.199	0.418
R521	0.191	0.056	1258	-149.34	0.257	0.551
R573	0.232	0.100	1353	361.56	0.304	0.668
R584	0.260	0.127	1397	-298.68	0.343	0.730

Figure 6.7 shows the As compositions y of $In_{1-x}Ga_xAs_yP_{1-y}$ films with lattice constants matched to InP substrate versus TBAs/(TBAs+TBP) flow ratio in MOCVD growth.

In contrast to the Ga incorporation (Figure 6.1) in the MOCVD growth of $In_{1-x}Ga_xAs_yP_{1-y}$ alloy, As incorporation does not change with the TBAs/(TBAs+TBP) flow ratio linearly. For both TBAs and TBP, they should be all decomposed at the growth temperature of around 630 °C. However, as the gas velocity in this reactor is very fast and thus, the gas sources can only stay in the reactor about 1~2 seconds. In such a short time, the TBAs and TBP may not be completely decomposed. Moreover, compares with TBAs, TBP has a lower decomposition rate [2]. The TBAs decomposition initiates a chain reaction process in the vapor phase, in which the t-butyl radicals released from a TBAs molecule facilitates the decomposition of another TBAs molecule which, in turn, generates another t-butyl radical and so on. The t-butyl radicals generated during the TBAs pyrolysis will also enhance the decomposition of TBP [2]. At lower TBAs/(TBAs+TBP) flow ratio, the segregation effect (distribution between solid phase and gas phase) of As in solid phase leads to the higher As incorporation compared to that of P. As the concentration of TBAs increases, the segregation coefficient of P in solid increases relative to that of As as observed in Figure 6.7. As a result, As composition increases with TBAs/(TBAs+TBP) ratio quadratically instead of linearly.

The correlation between As composition and energy bandgap of $In_{1-x}Ga_xAs_yP_{1-y}$ obtained from experimental results has been plotted in Figure 6.8. For comparison, the results from empirical Eq. (6.4) are also plotted in same graph.

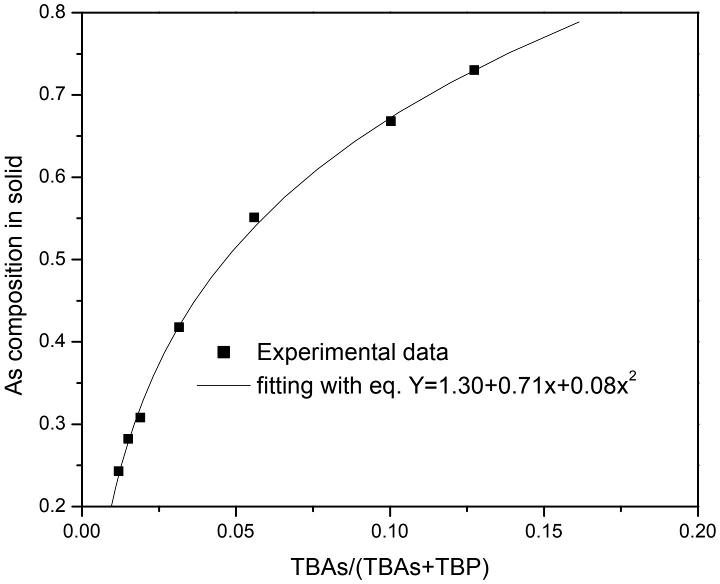

Figure 6.7: As incorporation characteristics for different flow ratio TBAs/(TBAs+TBP)

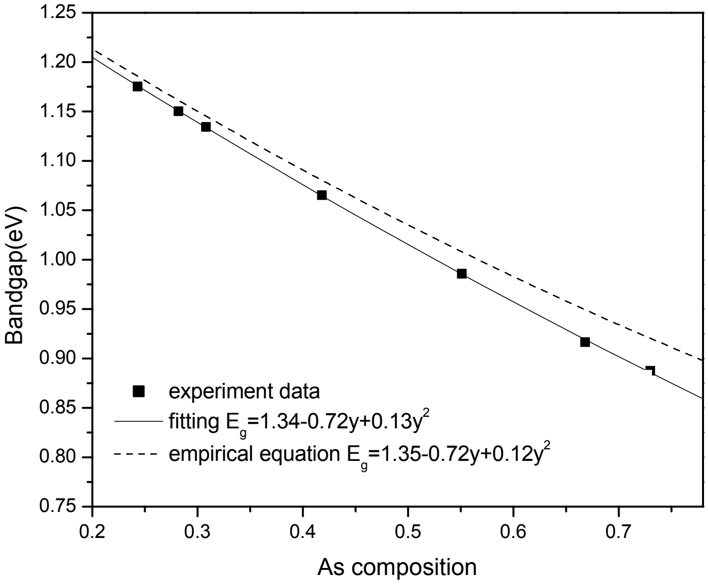

Figure 6.8: Bandgap energy E_g versus As composition y for $In_{1-x}Ga_xAs_yP_{1-y}$ nearly matched to InP, the full curve is a fit to the experimental data and the broken curve is from Eq. (6.4)

It shows that our experimental data agrees quite well with the results predicted by the empirical equation. The deviation between the experimental data and empirical equation results can be attributed to the contribution of group III composition variation. As mentioned before, to minimize the lattice mismatch, TMGa/(TMGa+TMIn) ratio was changed during the epilayer growth to achieve the desired wavelength. It is found that the deviation is more obvious at long PL emission wavelength (e.g. lower energy bandgap).

6.4 Summary

$In_{1-x}Ga_xAs_yP_{1-y}$ quaternary alloys with lattice matched to InP substrate covering the emission wavelength from 1 μm to 1.4 μm have been successfully grown in MOCVD system by using TBAs and TBP as group V precursors in N_2 ambient. Keeping the group V vapor phase input ratio of TBAs/(TBAs+TBP) unchanged, we have explored the correlation between the lattice constant of the grown epilayers and input vapor phase ratio of TMGa/(TMGa+TMIn) in MOCVD growth. The results show that the lattice mismatch of $In_{1-x}Ga_xAs_yP_{1-y}$ epilayer on InP substrate changes from tensile strain to compressive strain when the input vapor phase ratio of TMGa/(TMGa+TMIn) decreases from 0.276 to 0.215. The input group V gas flow ratio TBAs/(TBAs+TBP) also contributes to the variation of the lattice constant of the $In_{1-x}Ga_xAs_yP_{1-y}$ epilayer grown. The Ga incorporation efficiency is higher than that of In at growth temperature of 630 ^{o}C. The effect of group V input vapor phase ratio TBAs/(TBAs+TBP) in MOCVD growth on the epilayer's bandgap has also been investigated. It has been proved that the PL emission wavelength of the $In_{1-x}Ga_xAs_yP_{1-y}$ epilayer depends mainly on the vapor phase input ratio TBAs/(TBAs+TBP) instead of TMGa/(TMGa+TMIn) in MOCVD growth. The results show that at lower TBAs/(TBAs+TBP) flow ratio, the segregation coefficient of As is higher than that of P at the growth temperature of 630 ^{o}C .

Chapter 7 MOCVD growth of MQW structure

7.1 Introduction

InGaAs/InP Quantum wells (QW) are important structures for long wavelength optoelectronic devices in fiber optic applications. To grow high quality InGaAs/InP quantum well structures, it is very important to grow an abrupt interfaces between InGaAs and InP layers. For growing the lattice-matched QW, the solid composition of the epilayers must be carefully controlled to avoid lattice mismatch between the well layer and the barrier layer. Transients in the solid compositions between the different layer growths during switching in MOCVD growth may result in unintentionally strained region in the InGaAs/InP QW growth. Therefore, the incorporation of unintentional strain in heterostructure lasers during epitaxy growth is counterintuitive and was once considered a problem to be avoided.

Advances in MOCVD growth technology and the understanding of the physics and reliability of these materials have led to a remarkable increase in the commercial use of strained-layer structure in laser device structures. The laser diodes has benefited from the many favorable characteristics of these structures, including lower threshold current density, higher differential gain and efficiency, increased range of available emission wavelengths, and high reliability. The use of both tensile and compressive strained-layer heterostructures in semiconductor laser structures has become commonplace at all wavelengths and in other materials systems including visible [1], long-wavelength [2], and III–V nitride lasers [3].

In compositional switching between growth of InP and InGaAs in MOCVD, the carryover of gases during switching gives not only a non-abrupt interface but also the probability of strain at an imperfect interface. In addition, the volatile group V elements are lost during growth interruptions inserted to minimize carryover of gases during switching. This results in a graded interface, and solid-state diffusion across the interface may contribute a small effect to the interface grading. Therefore the presence of surfaces that are not atomically flat complicates the quantum-well growth. High-speed run/vent manifold and low-pressure MOCVD technology can reduce the above-mentioned side effects remarkably and an abrupt InGaAs/InP QW structure can be produced.

In this project, strained InGaAs/InP MQW structures have grown. The optical and structural properties of InP/InGaAs/InP multiple quantum wells structure grown have been studied.

7.2 MOCVD growth of InGaAs/InP MQW

InGaAs/InP MQW structure as shown in table 7.1 has been grown and studied. The MQW structure consists of a ten periods of 5nm thick InGaAs (compressive strain) well sandwiched by 12nm thick InP barriers. In order to introduce a compressive strain in the QW structure, Indium content in InGaAs was intentionally increased comparing to that of the ternary matched to InP to increase its lattice constant.

Table 7.1 Strained InGaAs/InP MQW structure

Material	Layer function	Doping (/cm3)	Composition	Thickness (nm)	Type
InP	cap	undoped		50	undoped
InP	InP barrier	undoped		12	undoped
10X$In_{1-x}Ga_{x}As$	Well	Strained	x=0.440	5	undoped
10XInP	InP barrier	undoped		12	undoped
InP	InP buffer	undoped		400	undoped
InP	InP substrate	3 x 10^18		-	n+

Sulfur-doped InP wafers with (100) orientation were used as substrates. The growth temperature was set as 630°C, while the reactor pressure was kept at 100mbar. A 400nm undoped buffer layer was grown and followed by 10 periods of InGaAs/InP quantum wells. Gas switching sequence for the barrier/well interface growth is shown in Figure 7.1. After growing the MQW, a 50nm InP cap layer was grown to terminate the structure growth. After the cap layer growth, the group III source (TMIn) and the reactor heater were switched off immediately while the TBP flow was kept to prevent the InP surface degradation during cooling down until the reactor temperature was below 300°C.

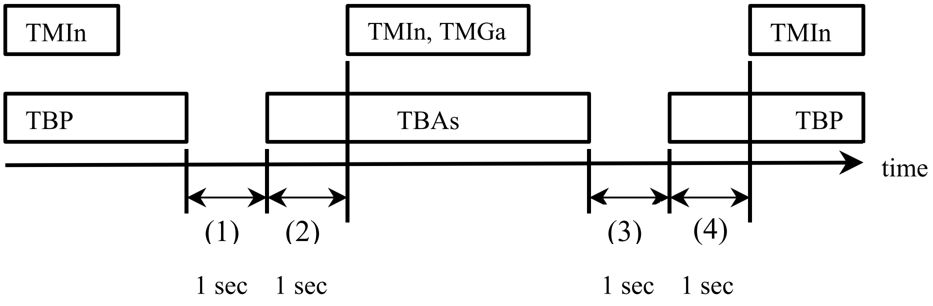

Figure 7.1: Sequence of source gas switching of InGaAs-InP MQW

It is very important to grow smooth and abrupt interfaces in the MQW structure. Steps (1) to (4) in Figure 7.1 are very critical for achieving smooth and abrupt interface in MOCVD growth. The length of these periods determines the degree of arsenic-phosphorus exchange. It will determine if its desorption of phosphorus out of InP or arsenic out of InGaAs. In this project, all these period were set with 1 second.

7.3 Characterization of the InGaAs-InP quantum wells

Mirror like smooth surface of the MQW structure was observed under Differential Interference Contrast (DIC) Microscope. To investigate the interface of the InP-InGaAs

QW, high resolution SEM was employed. Figure 7.2 shows the SEM image of cross section of the InGaAs/InP QW grown. The sample was stain-etched by H_3PO_4: H_2O_2: H_2O (1:1:100) prior to the measurement. The QW structure is very clear, which shows the good interface. The dark and bright lines represent the InGaAs well and InP barrier, respectively. And a QW period of around 16.9nm was obtained in this measurement.

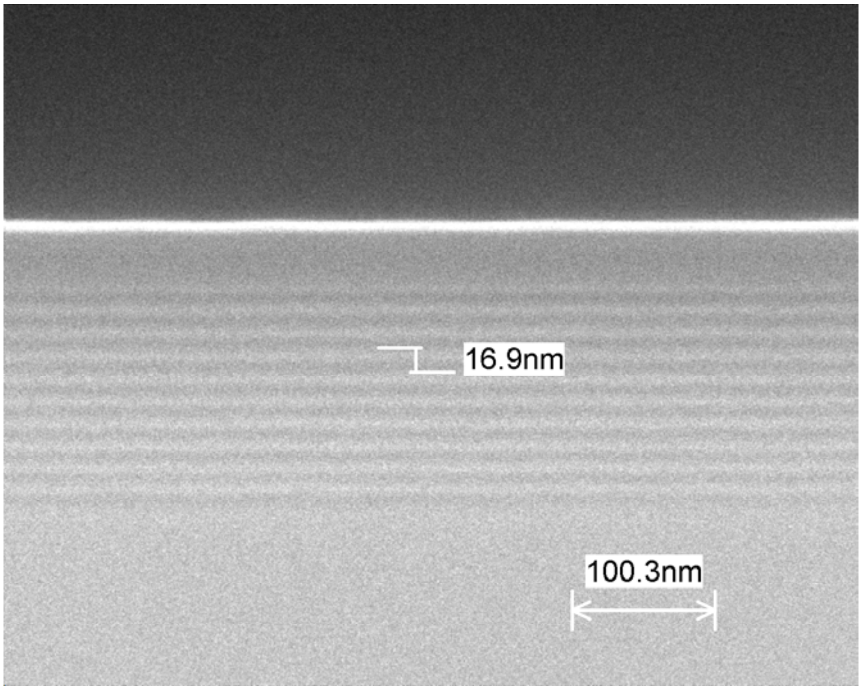

Figure 7.2: SEM image of QW

The good quality of QW structure was also indicated by the XRD measurement as shown Figure 7.3. Satellites peaks corresponding to the artificial crystalline periodical L_B+L_W have been resolved up to n= -8 (count). The n = 0 satellite peak is attributed to the (400) Bragg diffraction of the mean parameter of the quantum wells and barriers. It appears at the small angle side of the InP substrate peak, which implies that the InGaAs well is with a compressive strain.

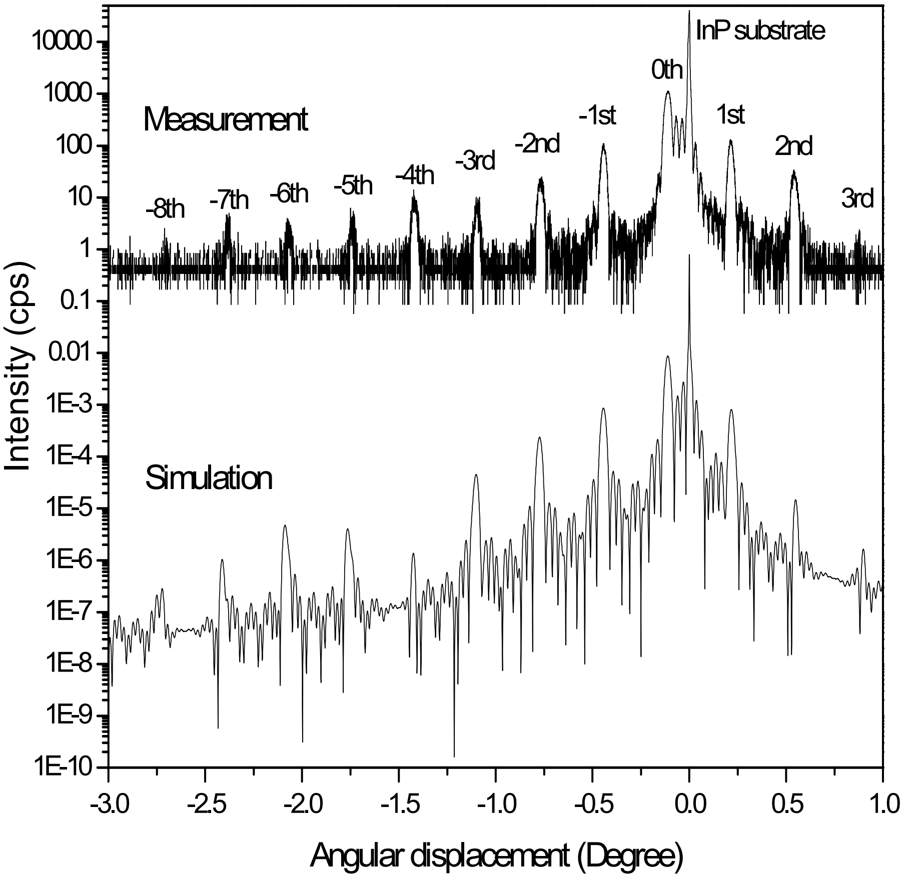

Figure 7.3: XRD rocking curve of the InGaAs-InP MQW structure grown

For InGaAs/InP quantum well, the strains in the InGaAs well ε_{Well}, and in the InP barrier $\varepsilon_{Barrier}$ are defined as

$$\varepsilon_{Well} = (a_{Well} - a)/a\,,\ \varepsilon_{Barrier} = (a_{Barrier} - a)/a\,, \tag{7.1}$$

where $a_{Well} = a_{InGaAs}$ and $a_{Barrier} = a_{InP}$, and a are unstrained lattice constants of the well, the barrier and the substrate, respectively. The average well-layer strain can be calculated by the following equation,

$$\varepsilon_{average} = \frac{\varepsilon_{well} \times L_{well} + \varepsilon_{barrier} \times L_{barrier}}{L_{well} + L_{barrier}} \tag{7.2}$$

where ε, L represent the strain and layer thickness, respectively.

In InGaAs-InP quantum well structure, the barrier is InP. Thus $\varepsilon_{barrier}$ is 0. Using Eq. (3.10) and (7.2), we can obtain that the strain of InGaAs well is 0.53% for this sample. Furthermore, we could deduce that the composition of the well layer in the QW grown is $In_{0.61}Ga_{0.39}As$.

The period ($L_{barrier}+L_{well}$) of the QW structure can be calculated from the XRD measurement results by using the Eq. (3.12). Using XRD software that based this equation, the periodic thickness of the QW is calculated to be 16.9nm, which is same as the SEM measurement result.

A XRD simulation was done for the grown QW structure as shown in Figure 7.3. Without considering the interface of QW, the simulation results fit the rocking curve measurement results very well. To reveal the interface quality, satellites intensity difference between the measurement result and simulation result are collected for comparison. The relative intensity ratio is set to 0^{th} order in Table 7.2.

Table 7.2 Satellite intensity ratio relative to 0^{th} order

	Relative ratio to 0^{th} order for measurement	Relative ratio to 0^{th} order for simulation
0^{th} order	1.000	1.000
1^{st} order	0.100	0.104
2^{nd} order	0.026	0.027
3^{rd} order	0.012	0.006
$2^{nd}/1^{st}$ order	0.260	0.255
$3^{rd}/1^{st}$ order	0.115	0.055

It is found that the simulation result agrees with the measurement data only down to the 2nd order. This may be due to the small deviation of well strain or thickness of well and barrier from the designed value. Interface variation may be another factor that affects the measured rocking curve. As we know, the interface quality is determined by precursors switching time of the interruption [4]. During these periods, group V sources (TBP, TBAs) act an important role during the interruption between InP barrier and InGaAs well growth.

The QW growth interruptions include four interrupt periods as indicated in Figure 7.1. Any improper timing of the interruption way significantly degrade the interface grown. If the timing for step (1) and step (3) is too short, the group V can not be purged completely. It will be incorporated into the next layer grown to form a graded composition interface in between. If these 2 periods are too long, depletion of phosphorus or arsenic may occur due to less group V pressure in the environment. The long period 2 will cause the diffusion of arsenic into the topmost InP layer to form InAsP. Because of the large lattice mismatch between InP and InAsP, the surface will become rough. Same as for period 4, the phosphorus may also incorporate into InGaAs to form an InGaAsP layer if the period is too long. And for period 4, if the preceding TBP injection time was too short, the InP barrier would be affected by the arsenic left over in the ambient, and forms an InPAs layer. To achieve better quality of interface, timing for group V switching should be investigated in detail according to the reactor configuration.

7.4 Optical properties of the InGaAs-InP quantum wells

Optical property of the InGaAs/InP QW structure (10 wells) grown was evaluated by using PL measurement. Figure 7.4 shows the room temperature PL of the QW with different excitation intensity. The PL spectra of the sample show an asymmetric feature measured at room temperature. This profile is similar to that of the single ternary layer or quaternary layer. The reason may still be related to the carrier distribution as described in the previous chapter.

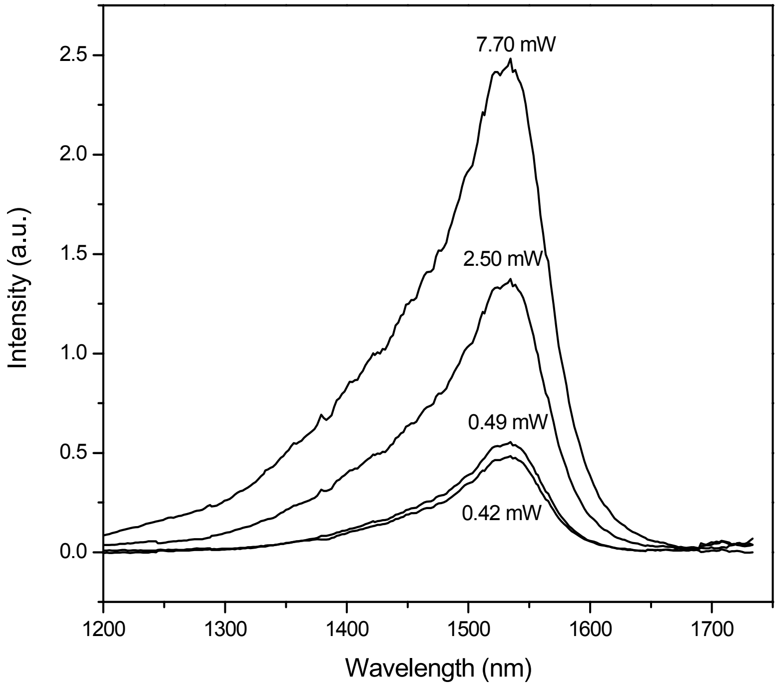

Figure 7.4: Comparison of room temperature PL spectra of the QW structure with different exciting laser source intensity (With CW YAG 1064nm laser excitation)

The PL peak wavelength of the QW is around 1530nm at room temperature. It is about 300nm shorter compared with that of the $In_{0.61}Ga_{0.39}As$ bulk layer. This large blue shift can be attributed to the quantum confinement effect, and the compressive strain effect in the QW structure. It is known that the energy band of the material in QW will split into subbands and the energy will increase. Meanwhile, the compressive strain will also increase the band energy, which is explained in the Figure 7.5.

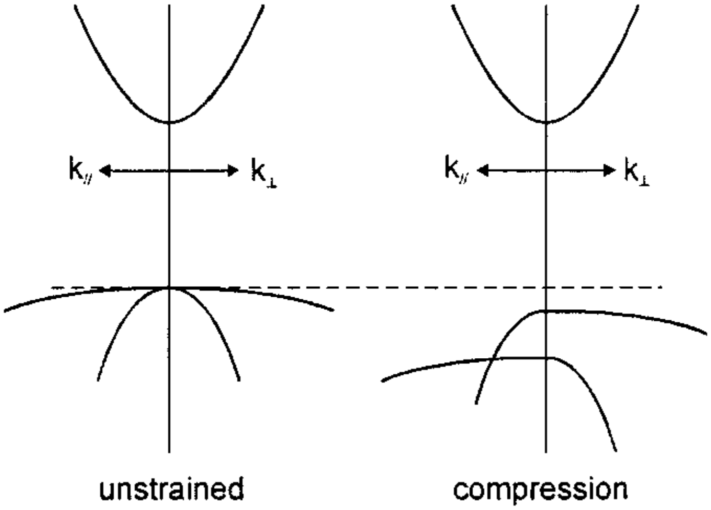

Figure 7.5: Schematic diagram of the conduction and valence band *E*-*k* diagrams for unstrained and compressively strained semiconductor layers.

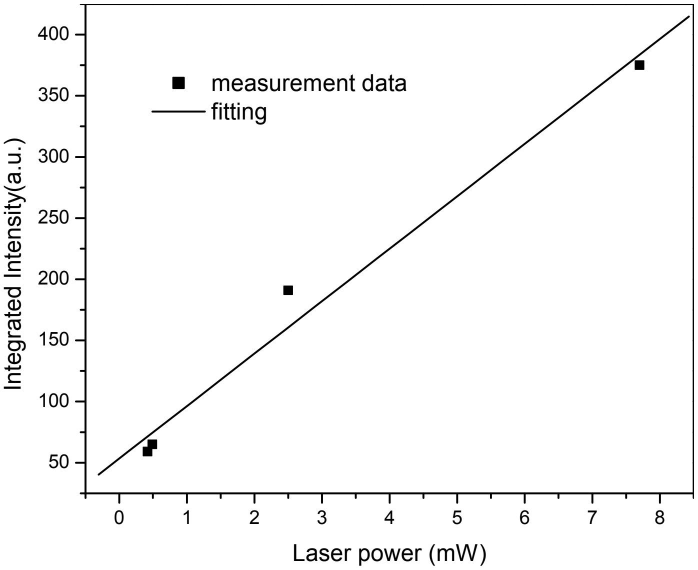

Figure 7.6: Excitation dependence of the PL emission intensity of the InGaAs/InP QW structure

Figure 7.6 shows the excitation intensity dependence of the PL integrated emission intensity. The integrated PL emission intensity of the QW increases with the excitation power linearly. Together with the fact that the emission peak wavelength (shown in Figure 7.4) didn't change with excitation level, it can be concluded that the excitation level is below the saturation, which means that the emission is within linear range and no band filling effect takes place. Figure 7.7 shows the PL spectra measured at different temperatures with same excitation power. We found that with increasing temperature, both the emission wavelength (within higher temperature range) and FWHM increase, while the peak intensity decreases. All these variations are common features of QW structure [5][6].

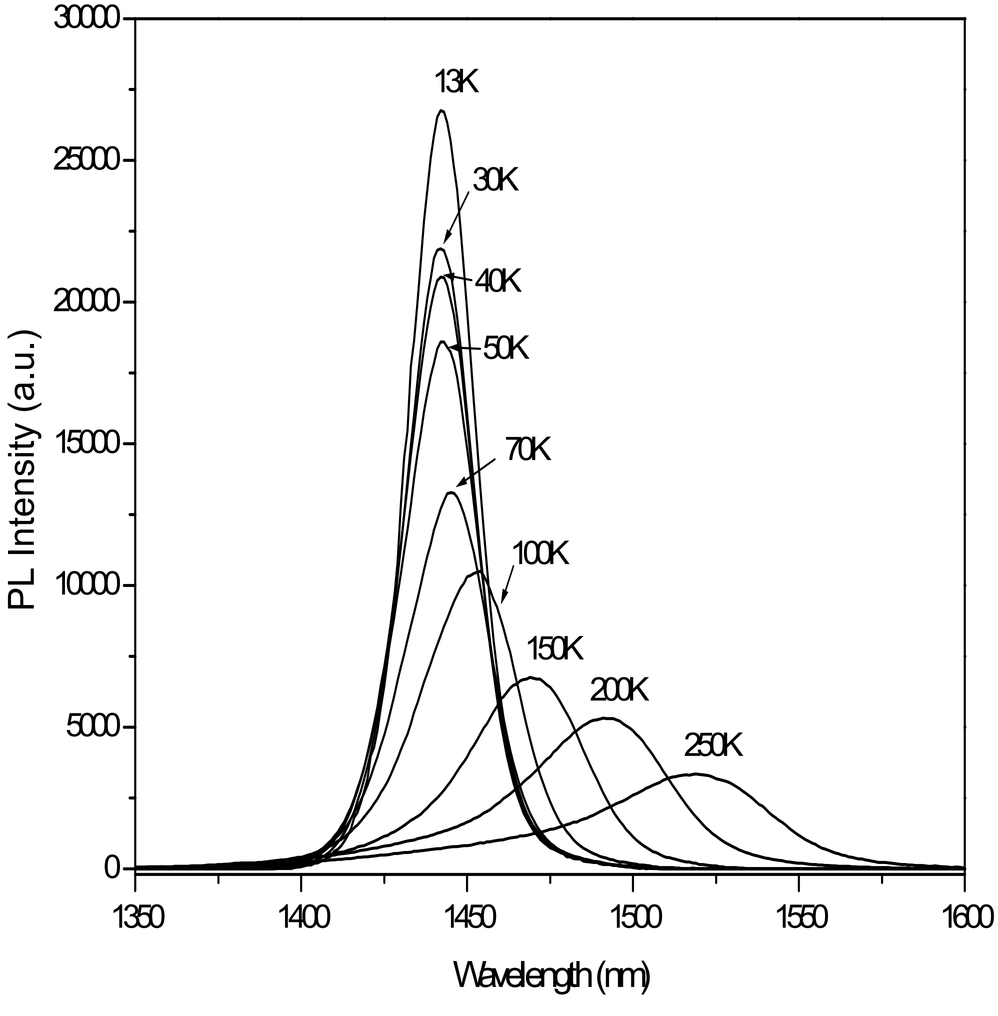

Figure 7.7: Temperature related PL spectra of MQW

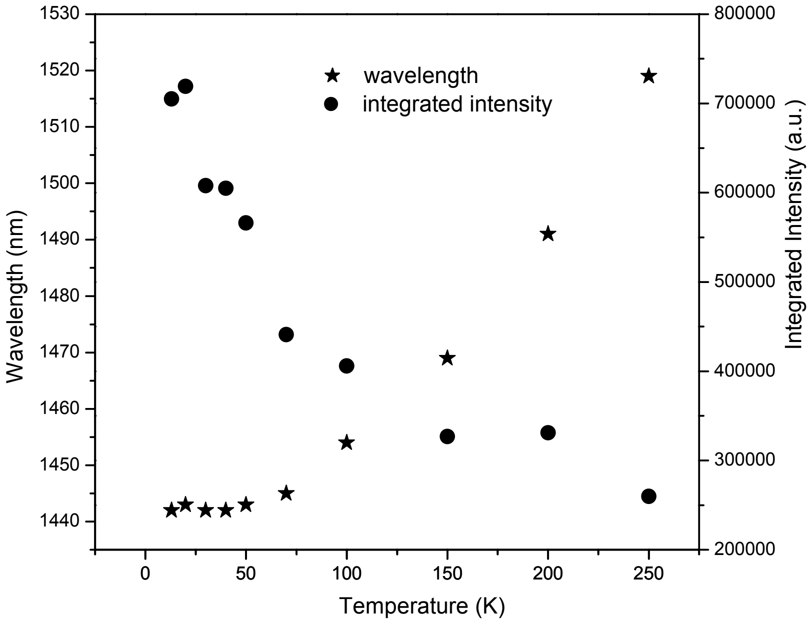

Figure 7.8: Temperature dependence of the peak wavelength and intensity.

Figure 7.8 shows the measured temperature dependence of the peak wavelength and integrated intensity of PL emission from the QW structure. At higher temperature region (>75K), the peak emission wavelength increases with the temperature almost linearly. At low temperature range (<70K), no much change in the peak wavelength as the temperature changes. At low temperature, exciton emission of the QW dominates the PL emission. When temperature increases, the exciton dissociation rate increases, and the density of free electrons and holes would increase. This leads to high possibility of the free electron-hole recombination in the higher temperature region. Because the exciton binding energy in InGaAs/InP is very small [7], higher temperature will thermally dissociate the excitons. In Figure 7.8, the wavelength threshold point is around 70K, which is corresponding to 6meV. This energy is comparable to the exciton binding energy. So, when the temperature is higher than 70 K, free electron-hole recombination will dominate in the PL emission. In the integrated intensity, there is also a sudden drop at 70 K, which means the emission mechanism may change at this point.

7.5 Summary

InGaAs-InP MQW structure has been grown. Alternative layers have been observed in the cross sectional SEM image. From the XRD measurement results, it also shows the high quality of the MQW. PL spectra of the QW at different temperatures have been measured. Within higher temperature range, the emission wavelength and FWHM increases with temperature. But at low temperature range, emission mechanism may be different from that the higher temperature range.

Chapter 8 Conclusion and recommendations

8.1 Conclusion

Using TBAs and TBP as group V precursors and N_2 as carrier gas, InP based binary, ternary and quaternary alloys and InGaAs/InP QW structure have been successfully grown by MOCVD technology.

To obtain uniform deposition on the wafer, gas flow rate between the total flow inside the reactor tube and out liner purge flow was carefully adjusted and balanced. With optimized flow rate, very uniform growth has been achieved.

With the optimized conditions, high quality of InP bulk material has been grown. The mobility of InP epilayer grown achieved 104,000 $cm^2/V \bullet s$ when measured at 77K by Hall measurement. Room temperature photoluminescence measurement on the InP epilayer shows a 22nm of FWHM, which is narrower than that of InP substrate. Si doping in InP epilayer has been investigated. With higher growth temperature, it was found the surface of the epilayer degraded. Relationship of electron carrier concentrations in Si-doped InP epilayer and the SiH_4 vapour input in MOCVD growth has been explored when grown at 630^{o}C.

The correlation between the hole carrier concentrations in the Zn-doped InP epilayer and the DEZn source flow rate was plotted. The hole carrier concentration in the Zn-doped InP epilayer increases linearly with the DEZn source flow rate in MOCVD growth. XRD and PL measurement of the samples were carried out.

Composition control of InGaAs ternary alloy in MOCVD growth has been investigated. Relationship between Ga composition in the grown InGaAs epilayers and TMGa/(TMGa+TMIn) vapor phase input ratio has been plotted. It has been found that within 1000ppm lattice mismatch with InP substrate, the lattice constant of InGaAs epilayer changes linearly with the TMGa/(TMGa+TMIn) vapor phase input ratio.

The surface morphologies of In-rich and Ga-rich grown InGaAs epilayers were found different at large mismatch when layer's thickness beyond the critical thickness. Reducing the lattice mismatch of the grown layer leads to an improvement of crystal quality of epilayer, and a narrower FWHM of RTPL. A better interface between the epilayer and substrate could also be received.

MOCVD growth of InGaAsP on InP substrate has been investigated. In this project, change of composition and bandgap of grown $In_{1-x}Ga_xAs_yP_{1-y}$ films by varying the vapor phase input ratio of TMGa/(TMGa+TMIn) and TBAs/(TBAs+TBP) in MOCVD has been evaluated. A linear correlation between Ga composition in grown $In_{1-x}Ga_xAs_yP_{1-y}$ film and vapor phase input ratio of TMGa/(TMGa+TMIn) in MOCVD growth has been observed. It has been found that the Ga incorporation is higher than that of In in $In_{1-x}Ga_xAs_yP_{1-y}$ MOCVD growth. The possible reason may due to In atom has lower affinity and higher surface atomic mobility comparing with Ga in the epitaxial growth at this growth temperature. It was also found that when TMGa/(TMGa+TMIn) vapor phase input ratio decreases, the epilayer's strain changes from tensile to compressive, while its PL emission wavelength shifts to longer wavelength. If reducing the lattice mismatch between the epilayer layer and substrate, the interface would be sharper. Variations of the As composition in $In_{1-x}Ga_xAs_yP_{1-y}$ epilayer with different vapor phase input ratio of TBAs/(TBAs+TBP) in MOCVD growth has also been studied. It has been found that the segregation coefficient of TBP becomes higher when TBAs/(TBAs+TBP) flow rate ratio increases. This may because that the chain reaction of TBAs causes the TBP decompose easier. The emission wavelength of $In_{1-x}Ga_xAs_yP_{1-y}$ epilayer is very sensitive to its As composition. The lattice constant of grown $In_{1-x}Ga_xAs_yP_{1-y}$ film does not only depend on

TMGa/(TMGa+TMIn) flow ratio in MOCVD growth, but also depends on the TBAs/(TBAs+TBP)) flow ratio.

High quality InGaAs/InP QW structures have been grown. A 10 strained InGaAs/InP MQW structure has been grown. The emission wavelength of the MQW structure was measured at 1530nm at room temperature. For room temperature PL measurement, the integrated intensity of PL of the MQW increases linearly with excitation power. The emission wavelength and FWHM increases, while the peak intensity decreases as the temperature increases. Composition variation between well and barrier interfaces of the QW was discussed. SEM image shows the good interface of the QW structure. XRD rocking curve result agrees well with simulation result, which represents good quality and good interface of the QW structure grown.

8.2 Recommendations for Further Research

In this project, MOCVD growth of indium phosphide based compounds, InP, InGaAs, InGaAsP bulk layers and InGaAs/InP QW structures have been investigated in detail. N-type and P-type doping in the epilayers have been explored. High quality of InP, InGaAs and InGaAsP epitaxy films and MQW structure have been successfully grown in MOCVD by using TBAs, TBP as group V precursors in N_2 ambient.

Based on the results obtained, the long wavelength (1.5μm and 1.3μm) laser diode structure can be grown for novel photonic device development. To achieve the better quality of the quantum well structure for laser applications, more experiments need to be done to optimize the interface of quantum wells, e.g. the interruption time between barrier and well during the growth. For further study, Transmission Electron Microscopy (TEM) might be employed to investigate the QW interface quality. Surface morphology dynamics of InGaAs epilayers with different kind of strain needs to be investigated. Zn diffusion properties must be considered in the device fabrication. To reach good Ω-contact on P-side, higher doping level ($>1\times10^{19}cm^{-3}$) Zn:InGaAs as P-contact layer need to be achieved. Due to the time limitation, no enough data have been collected to investigate the reproducibility and no laser device was fabricated from the samples grown in this project. For future study, more runs needed for MQW structure growth to verify the high quality of the structures. A full laser diode structure will be grown, the laser device will be fabricated and tested to verify the high quality of the structures grown for optoelectronics application.

Appendix A: Author's Publications

1. X. H. Tang, S. J. Chua, B. L. Zhang, **J. Y. Zhu**, G. S. Huang, "Optical Induced Blueshift of Photoluminescence Excitation spectrum in n-i-p-i Multiple Quantum Well Structures", *Superlattices and Microstructures,* Vol.32 (2-3) (2003) 135
2. B. L. Zhang, X. H. Tang, G. S. Huang and **J. Y. Zhu**, "MOCVD Growth of GaAs/InGaAsP SQW structures for 808 nm high power laser diode fabrication"*, International Conference on Materials for Advanced Technologies (ICMAT), Singapore, 7 Dec., 2003.*
3. X. H. Tang, S. J. Chua, B. L. Zhang, **J. Y. Zhu**, G. S. Huang, "Optical Induced Blueshift of PLE spectrum in n-i-p-i Multiple Quantum Well Structures" *2002 Conference on Optoelectronic and Microelectronic Materials and Devices (COMMAD2002)*, December 11-13, Sydney, (presented)
4. C. Chan, X. H. Tang and **J. Y. Zhu**, "LP-MOCVD growths of InP and InGaAsP by using TBA and TBP in N2 ambient", *International Conference on Materials for Advanced Technologies 2001*, Singapore, p.391
5. X.H. Tang**,** Y. C. Chan and **J. Y. Zhu**, "Photoluminescence of AlGaAs alloy grown by LP-MOCVD at different temperature using TBA in N2 ambient", *International Conference on Materials for Advanced Technologies 2001*, Singapore, p.400
6. B. L. Zhang, X. H. Tang, G. S. Huang, T. Mei, **J. Y. Zhu**, H.Li "Morphology and optical properties of GaAs layers grown on (1 1 1)A GaAs substrates in

N_2 ambient by metalorganic chemical vapor deposition" , *Journal of Materials Science: Materials in Electronics,* 15 (5): 283-286, May 2004

7. B. L. Zhang, X. H. Tang, G. S. Huang and **J. Y. Zhu**, "Study of InGaAsP and GaInP layers grown by MOCVD in pure N2 ambient for InGaAsP/GaAs single QW LD structures", *Journal of Crystal Growth, Volume 268, Issues 3-4, 1 August 2004, Pages 396-400*

Appendix B: Bibliography

Chapter 1

[1] M. Razeghi, "High-power laser diodes based on InGaAsP alloys," *Nature*, 369 (1994) 631.

[2] M. Razeghi, W. T. Tsang, "Lightwave Technology for Communication", *Ed*. New York: *Academic*, 1985.

[3] J. P. Duchemin, J. P. Hirtz, M. Razeghi, M. Bonnet, and S. D. Hersee,"GaInAs and GaInAsP materials grown by low pressure MOCVD for microwave and optoelectronic applications," *J. Cryst. Growth*, 55 (1981) 64.

[4] R.J. Manning, A.D. Ellis, A.J. Poustie, and K.J. Blow, "Semiconductor laser amplifiers for ultrafast alloptical signal processing," *J. Opt. Soc. Am. B* 14(11) (1997). 3204.

[5] R. J. Simes, E. G. Goarin, C. Labourie, D. Bonnevie, A. Perales, D. Lesterlin and L. Goldstein "GSMBE growth on patterned substrates for optoelectronic devices," *Proc. 4th Int. Conf. on InP and Related Materials* (Piscataway, NJ: IEEE Publications, 1992).

[6] B. T. Lee, R. A. Logan, R. F. Kalicek, Jr., A. M. Sergent, D. L. Coblentz, K. W. Wecht and T. Tanbun-Ek, "Fabrication of InGaAsP/InP buried heterostructure laser using reactive ion etching and metalorganic chemical vapor deposition, " *IEEE Photon. Technol. Lett*. 5: (1993) 279.

[7] L. D. Nguyen, L. E. Larson, and U. K. Mishra, "Ultra-high-speed modulation-doped field-effect transistors: A tutorial review," *Proc. IEEE,* 80 (1992) 494.

[8] J.-I. Song, B. W.-P. Hong, C. J. Palmston, B. P. V. Gaag, and K. B. Chough, "Ultra-high-speed InP/InGaAs heterojunction bipolar transistors," *IEEE Electron Device Lett.*, 15 (1994) 94.

[9] H. Nakajima, K. Kurushima, S. Yamahata, T. Kobayashi, and Y. Matsuoka, "High-speed InP/InGaAs HBT's operated at submilliampere collector currents," *Electron. Lett.*, 29 (1993) 1887.

[10] M. Razeghi, S. Slivken, A. Matlis, A. Rybaltowski, C. Jelen, and J. Diaz, "Low threshold quantum cascade lasers grown by GSMBE," *LEOS Newsletter*, 12 (6) (1998) 5.

[11] S. Ae, T. Terakado, T. Nakamura, T. Torikai, T. Uji, "Low threshold 1.3μm multi-quantum well laser diodes grown by metalorganic vapor phase epitaxy using tertialrybutylarsine and tertiarybutylphosphine precursors", *Journal of Crystal Growth* 145 (1994) 582.

[12] S. Leu, F. Hohnsdorf, W. Stolz, R. Becker, A. Salzmann, A.Greling, "C -and O-incorporation in (AlGa)As epitaxial layers grown by MOVPE using TBAs", *Journal of Crystal Growth* 195 (1998) 98 98-104.

Chapter 2

[1] S. Ryu and P. D. Dapkus, "Highly strained InGaAs QW VCSEL with lasing wavelength at 1.22μm," *Electron. Lett.*, 37 (2001) 177.

[2] M. Razeghi, Lightwave Technology for Communication, W. T. Tsang, Ed. New York: Academic, 1985.

[3] M. Razeghi, "CW phase-locked array GaInAsP–InP high power semiconductor laser grown by low-pressure metalorganic chemical vapor deposition," *Appl. Phys. Lett.*, 50 (1987) 230.

[4] M. Razeghi, R. Blondeau, M. Krakowski, B. de Cremoux, J. P. Duchemin, F. Lozes, M. Martinot, and M. A. Bensoussan**,** "cw phase-locked array $Ga_{0.25}In_{0.75}As_{0.5}P_{0.5}$-InP high power semiconductor laser grown by low-pressure metalorganic chemical vapor deposition" *Appl. Phys. Lett.*, 50 (1987) 230.

[5] J. P. Duchemin, J. P. Hirtz, M. Razeghi, M. Bonnet, and S. D. Hersee, "GaInAs and GaInAsP materials grown by low pressure MOCVD for microwave and optoelectronic applications," *J. Cryst. Growth*, vol. 55 (1981) 64.

[6] M. Kuznetsov, A. E. Willner, and I. P. Okaminow, "Frequency-modulation response of tunable 2-segment distributed feedback lasers," *Appl. Phys. Lett.*, 55, (18) (1989) 1826.

[7] M. Erdtmann, J. Jiang, A. Matlis, A. Tahraoui, C. Jelen, M. Razeghi, and G. J. Brown, "Growth and optimization of the GaInAsP/InP material system for quantum well infrared photodetector applications," *Proc. SPIE*, 3948 (2000) 227.

[8] C. Jelen, S. Slivken, V. Guzman, M. Razeghi, and G. Brown, "InGaAlAs/InP quantum well infrared photodetectors for 8–20μm wavelengths," *IEEE J. Quant. Electron.*, 34 (1998) 1873.

[9] J. Faist, F. Capasso, D. L. Sivco, C. Sirtori, A. L. Hutchinson, and A. Y. Cho, "Quantum cascade laser," *Science*, 264 (1994) 553.

[10] F. Capasso, J. Faist, C. Sirtori, and A. Y. Cho, "Infrared (4–11 μm) quantum cascade lasers," *Solid State Commun.*, 102 (1997) 231.

[11] T.P.Pearsall, "GaInAsP alloy semiconductors", New Jersey, USA, 1982

[12] S.Bass, and P.E. Oliver, "Growth of large indium phosphide crystals" *J.Cryst. Growth* 54 (1981) 32.

[13] M. Razeghi, "Very high purity InP epilayer grown by metal organic chemical vapour deposition," *Appl. Phys. Lett.*, 52 (2) (1988) 117.

[14] G.A.Antypas, R.L.Moon, L.W.James, J.Edgecumbe, and R.L.Bell, "III-V quaternary alloys", *Gallium Arsenide and Related compounds*, 1972, Conf. Ser.no. 17, Institute of Physics, London, (1973) 48.

[15] A.R.Clawson, W.Y Lum, G.E McWilliam, and H.H. Wieder, "quaternary alloy InGaAsP/InP photodetectors", *Appl. Phys. Lett*. 32 (1978) 549.

[16] Amnon Yarif, "Optical Electronics in Modern Communications", Oxford University Press, Fifth Edition, 1997.

[17] R.Sankaran, R.L. Moon, and G.A.Antypas, "Liquid phase epitaxial growth of InGaAs on InP", *J.Cryst. Grwoth*, 33 (1976) 271.

[18] H. M. Manasevit, and W.I. Simpson, "the use of metal-organic in the preparation of semiconductor materials", *J. Electrochem. Soc.,* 126 (1979) 2031.

[19] Dupuis, R. D. and Dapkus, P. D. **"**$Ga_{(1-x)}Al_xAs/Ga_{(1-y)}Al_yAs$ double-heterostructure room-temperature lasers grown by metalorganic chemical vapor deposition", *Appl. Phys. Lett*. 31(12) (1977) 839

[20] H.Roehle, H. Schereter-Jansen, R.Kaiser, Large- and selective-area LP-MOVPE growth of InGaAsP-based bulk and QW layers under nitrogen atmosphere", *J.Crystal Growth* 170 (1997) 109.

[21] A Krotkus, S Marcinkevicius, V Pasiskevicius and U Olin, "Ultrafast photoluminescence decay in low-temperature MOCVD-grown $In_xGa_{1-x}As$", *Semicond. Sci. Technol*. 9 (July 1994) 1382, Stockholm, Sweden.

[22] S. Ae, T. Terakado, T. Nakamura, T. Torikai, T. Uji, "Low threshold 1.3µm multi-quantum well laser diodes grown by metalorganic vapor phase epitaxy using tertialrybutylarsine and tertiarybutylphosphine precursors", *J. Crystal Growth* 145 (1994) 582.

Chapter 3

[1] M.S. Ravetz, L.M. Smith, etc., “Properties of Solution TMI as an OMVPE Source”, *J. Electronic Matereial*, 29, (2000) 156.

[2] Frigo D.M., Van Berkel W., Maassen W.A.H., “A method for dosing solid sources for MOVPE: excellent reproducibility of dosimetry from a saturated solution of trimethylindium”, *J. Cryst. Growth* 124 (1992) 99.

[3] 3 N. I. Buchan, C. A. Larsen, and G. B. Stringfellow, “Elucidation of the organometallic vapor phase epitaxial growth mechanism for InP”, *Appl.* Phys. Lett. 51 (1987) 1024.

[4] Jalil Ouazzani and Franz Rosenberger “Three-dimensional modelling of horizontal chemical vapor deposition: I. MOCVD at atmospheric pressure” *J. Crys.Growth*, 100 (1990) 545.

[5] G.B. Stringfellow, “Organometllic Vapour-Phase Epitaxy: Theory and Practice,” Second Edition. Chap. 6.

[6] S.H.Li, C.A.Larsen, and D.S.Cao, and G.B.Stringfellow, “OMVPE growth mechanism for GaP using tertiarybutylphosphine and trimethylgallium”**,** *J. Cryst. Growth*, 96 (1989) 906.

[7] Masakazu Sugiyama, Olivier Feron, Sinya Sudo, etal, “Kinetics of GaAs Metalorganic Chemical Vapor deposition Studied by Numerical Analysis Based on Experimental Reaction Data”, *Jpn. J. Appl. Phys*. 39 (2000) 1642.

[8] “Analytical software for X’Pert PRO MRD”, Philips Analytical.

Chapter 4

[1] S. Sugou, A. Kameyama, Y. Myamoto, K. Furuya and Y. Suematsu, "Conditions for OMVPE Growth of GaInAsP/InP Crystal," *Jpn. J. Appl. Phys*. 23 (1984) 1182.

[2] G.B. Stringfellow, Organometallic Vapor Phase Epitaxy (Academic Press, San Diego, CA, 1989.) Chap. 6.

[3] J.L. Zilko, P.S. Davisson, L. Luther, K. D. C. Trapp, "Improved compositional uniformity of InGaAsP grown by low pressure metalorganic vapor phase epitaxy using tertiary butyl phosphine as the phosphorus source"**,** *J. Crystal Growth*, 124 (1992) 112.

[4] S.N.G Chu, R.A. Logan, M.Geva, and N.T. Ha, "Concentration dependent Zn diffusion in InP during metalorganic vapor phase epitaxy", *J. Appl. Phys.*, 78 (1995) 3001.

[5] M. Razeghi, "The MOCVD Challenge: Volume 1: A Survey of GaInAsP-InP for Photonic and Electronic Applications", Northwestern University, Evanston, Illinois, USA Jan 1989

Chapter 5

[1] J. Birch, J. E. Sundgren, and P. F. Fewster, "Measurement of the lattice parameters in the individual layers of single-crystal superlattices" *J. Appl. Phys*. 78 (1995) 6562.

[2] Sadao Adachi, "Material parameters of $In_{1-x}Ga_xAs_yP_{1-y}$ and related binaries" *J. Appl. Phys*. 53 (1982) 8775.

[3] T.Okada, G.C.Weatherly, and D.W.McComb, "Growth of strained InGaAs layers on InP substrates", *J.Appl.Phys*.,Vol.81,No.5,1 March 1997.

Chapter 6

[1] Mitsuo Fukuda, "Laser and LED Reliability Update," *Journal of Lightwave Technology*., 6 (1988) 1488.

[2] S.H. Li, N.I. Buchan, G.B string fellow, "The effect of supplemental *t*-butyl radicals on the pyrolysis of tertiarybutylarsine, tertiarybutylphosphine, and ditertiarybutylarsine", *J. Crystal Growth* 98 (1989) 309.

[3] Kim, K. Uppal, W. J. Choi, "Composition control of InGaAsP in metalorganic chemical vapor deposition using tertiarybutylphosphine and tertiarybutylarsine", *J. Crystal Growth,* 193 (1998) 293.

[4] J.R. Flemish, H. Shen, K.A. Jones, M.Dutta, V.S. Ban, "Determination of the composition of strained InGaAsP layers on InP substrates using photoreflectance and double-crystal x-ray diffractometry", *J. Appl. Phys*. 70 (1991) 2152.

[5] W.L Holstein, "Methods to improve the P/As compositional uniformity of InGaAsP thin films prepared by MOCVD", *J. Crystal Growth* 167 (1996) 525.

[6] G.B. Stringfellow, Organometallic Vapor Phase Epitaxy (Academic Press, San Diego, CA, 1989).

[7] R.E.Rahory, M.A.Oollack, W.D. Johnston, Jr, and R.L. Barns, "Band gap versus composition and demonstration of Vegard's law for $In_{1-x}Ga_xAs_yP_{1-y}$ lattice matched to InP", *Appl.Phys. Lett*., 33 (1978) 659.

[8] T.P.Pearsall, "GaInAsP alloy semiconductors", New Jersey, USA, 1982

[9] Jonathan E. Greenspan, "Alloy composition dependence in selective area epitaxy on InP substrates", J. Crystal growth, 236 (2002) 273-280.

Chapter 7

[1] A. Valster, C. J. Van der Poel, M. N. Finke, and M. J. B. Boermans, "Low threshold current density (760 A/cm2) and high power (45 mW) operation of strained Ga In P multiquantum-well laser diodes emitting at 632 nm," *Electron. Lett.*, 28 (1992) 144.

[2] P. J. A. Thijs, L. F. Tiemeijer, J. M. Binsma, and T. Van Dongen, “Progress in long-wavelength strained-layer InGaAs(P) quantum-well semiconductor lasers and amplifiers,” *IEEE J. Quantum Electron.*, 30 (1994) 477.

[3] S. Nakamura and G. Fasol, *The Blue Laser Diode*. New York: Springer-Verlag, 1997.

[4] Shinya SudoU, Yoshiaki Nakano, Masakazu Sugiyama, Yukihiro Shimogaki, Hiroshi, Komiyama, Kunio Tada, “In-situ As-P exchange monitoring in metal-organic vapor phase epitaxy of InGaAsrInP heterostructure by spectroscopic and kinetic ellipsometry” *Thin Solid Films* 313-314 (1998) 604.

[5] R. W. Glew, M. L. Gray, M. S. Hybertsen, K. A. Grinm-Bogdan and N.N.Tzafaras, “Analysis of the photoreflectance spectra of GaInAsP/GaInAsP multi-quantum well structures”, *10th Intern. Conf. On Indium Phosphide and Related materials*, 11-15 May 1998, Tsukuba, Japan.

[6] Ms Hybersen, G.A.Baraff, S.K.Sspeutz, D.A.Ackerman, J.M Vanderverg, R.Lum, C.L.Reynolds, M.Leibovitch and F.H.pollanck, “Physics and Simulation of Optoelectronic Devices IV”, *Proc. SPIE*, (1996) 2693.

[7] M. S. Skolnick, J. M. Rorison, K. J. Nash, D. J. Mowbray, P. R. Tapster, S. J. Bass, and A. D. Pitt , “Observation of a Many-Body Edge Singularity in Quantum-Well Luminescence Spectra”, Phys. Rev. Lett. 58, 2130–2133 (1987).

Appendix C: Other metrology tools used in this project

C1 Electrochemical C-V (EC-V) profiling

Electrochemical C-V (EC-V) profiling of semiconductors is probably the most used and convenient method for accurate determination of thermal equilibrium majority carrier concentration depth profiles. By making use of a well-defined electrochemical dissolution reaction, the impurity doping concentration distribution in a semiconductor sample can be profiled to any depth at a controlled and calculated rate.

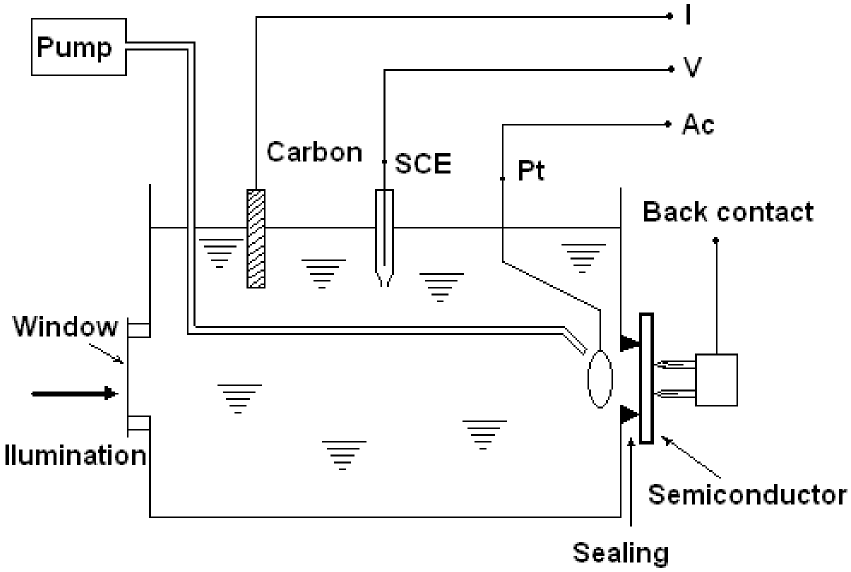

Figure C1.1: Schematic diagram of the electrochemical cell used in EC-V profiles

Figure C1.1 shows a schematic diagram of an electrochemical cell used in ECV profiles. The semiconductor sample is held against a sealing ring, which defines the contact area, by means of spring-loaded back-contacts. The etching and measuring conditions are controlled by the electrical potential across the cell. The potential is established by passing a DC current through the semiconductor and the carbon electrode to maintain the required over-potential. The potential is measured potentiometrically with reference to the saturated calomel electrode (SCE). The AC signals are measured with respect to a Pt electrode located near the semiconductor surface to reduce the series resistance of the electrolyte. The capacity associated with the charged depletion zone in the semiconductor is then determined.

When the contact is illuminated with photon energy greater than the bandgap of the semiconductor, the reverse current is increased due to the flow of hole and electrons from the semiconductor into the electrolyte in n- and p-type material, respectively. This causes a change in the voltage for zero current which is of opposite sign for n- and p-type material and can therefore be used to indicate the material type. Material is dissolved when an anodic current is drawn by a flow of hole from the InP, whereas a cathode current causes deposition of material from the electrolyte (which is 0.5M HCl solution for InP) onto the semiconductor surface. In order to etch n-type material, the holes are generated only by illumination under reverse bias. Smooth removal of n-type material is achieved with applied proper anodic current, which depends upon the illumination intensity but not upon the potential. For measuring a p-type material sample, the potential is switched from an anodic current to a cathode current. To avoid contaminating the sample surface by the cathode reaction promoted by electrons from the conduction band, it is important to make the cathode potential in such a condition that the reverse current is very small during the measurement.

The depth etched (X_e) is calculated by using Faraday's law of electrolysis:

$$X_e = (\frac{M}{qFDS})\int Idt, \tag{C1.1}$$

where M is the molecular weight, D is the density of the semiconductor material, F is the Faraday constant, S is the dissolution surface and q is the charge transferred per molecule dissolved. For InP, q = 6, the depletion depth (X_d) can then be obtained from:

$$X_d = \frac{\varepsilon\varepsilon_0 S}{C}, \tag{C1.2}$$

By measuring the capacitance of the sample, C, at 3 KHz (=0.14 V peak to peak), carrier concentration, $N(X_d)$ is derived from:

$$N(X_d) = \frac{C^3}{e\varepsilon\varepsilon_0 S^2}\left(\frac{\Delta C}{\Delta V}\right). \tag{C1.3}$$

where $\Delta C/\Delta V$ is measured with the modulation frequency at 30 Hz (≈0.28 V peak to peak) and at a low fixed DC reverse bias.

ACCENT PN4300PC EC-V profiling system was used in this project to get the background doping of InP and related epilayers. Combining the Photo Voltage Measurement in this system, bandgap of the ternary III-V semiconductors can be measured.

C2 Van der Pauw or Hall bar measurements

Hall measurement is a very common way to measure the carrier concentration and mobility of semiconductor material. Hall effect can be achieved by inducing a magnetic field perpendicular to the current flow direction in a semiconductor sample. Under such conditions, a voltage drop is developed in the sample perpendicular to both the current and magnetic field direction. This voltage is known as Hall voltage. The origin of Hall voltage is schematically shown in Figure C2.1. The force applied on the charges in the sample in the presence of an electric and magnetic field is:

$$\vec{F} = q\vec{E} + q\vec{V} \times \vec{B}. \tag{C2.1}$$

The first term on the right side of equation C2.1 is an electric force is due to the total electric field which drives the current through the sample. The second term is due to the Lorentz force on the moving charged carriers. It tends to deflect the carrier moving toward the side perpendicular to the carrier moving direction in the sample. The side direction of the carriers deflected depends on whether they are electron carriers or hole carriers.

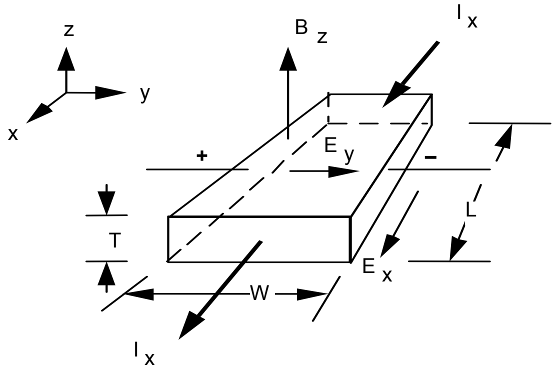

Figure C2.1: Hall effect on a sample. Current flows in positive x-direction. The applied magnetic field is along the positive z-direction. For a p-type sample an internal electric field developed along the positive y-direction because of the Hall effect.

Consider the example illustrated in Figure C2.1, and assume that a p-type doped semiconductor sample is applied with a magnetic field along z-direction. The applied electric field direction on the sample, so the current flow direction, is in the positive x-direction. The Lorentz force acting on the current flow is along -y direction, which is,

$$\vec{F}_y = -q\vec{E}_y + q\vec{V} \times \vec{B}_z \ . \qquad \text{(C2.2)}$$

In this case, the carriers moving in the sample will experience a force that drives them toward the negative y-direction.

When a number of holes are collected at the right side of the sample, an internal electric field in the +y-direction will be generated. This internal electric field prevents the positive charge from further accumulating on the y direction side of the sample caused by the Lorentz force. When these two forces balance, one has

$$E_y = V_x B_z \ . \qquad \text{(C2.3)}$$

The internal field can be measured by measuring the voltage drop, V_y, across the sample. Thus:

$$E_y = \frac{V_y}{w}, \qquad \text{(C2.4)}$$

where w is the width of the sample. V_y is known as the Hall voltage.

The hole carrier current in the sample can be written as:

$$\vec{I}_p = qp\vec{v}_d A, \qquad \text{(C2.5)}$$

where $+q$ is the hole charge, p is the hole density in the sample, $\vec{v}_d$ is the drift velocity of the carriers, and A is the cross sectional area of the sample. The current density:

$$\overrightarrow{J_p} = qp\overrightarrow{v_d}\ . \qquad \text{(C2.6)}$$

The drift velocity is:

$$\overrightarrow{v_d} = \mu_p \vec{E} \text{ for holes and } \overrightarrow{v_d} = -\mu_n \vec{E} \text{ for electrons.} \qquad \text{(C2.7)}$$

Substituting this into the current density equation 3.17

$$\overrightarrow{J_p} = qp\mu_p \vec{E} \quad \text{for holes and } \overrightarrow{J_n} = qn\mu_n \vec{E} \quad \text{for electrons,} \qquad \text{(C2.8)}$$

and:

$$E_y = v_x B_z = \frac{J_x}{qp} B_z = R_H J_x B_Z, \qquad \text{(C2.9)}$$

where $R_H = 1/qp$ is called the Hall coefficient. It can be shown that for n-doped samples, $R_H = -1/qn$.

When both electron and holes are present in the sample, the Hall coefficient will be:

$$R_H = \frac{1}{q}\frac{(p\mu_p^2 - n\mu_n^2)}{(p\mu_p + n\mu_n)^2}\ . \qquad \text{(C2.10)}$$

To acquire doping concentration, Equation (C2.9) can be rearranged as

$$R_H = \frac{E_y}{J_x B} = \frac{(V_y / W)}{(IB / WT)} = \frac{TV_y}{IB}. \qquad \text{(C2.11)}$$

It can be seen that using measurements of the Hall voltage, magnetic field, current, and sample thickness to determine the Hall coefficient for any sample. From the Hall coefficient one can derive the doping density, p or n. This measurement is a diagnostic tool for determining the doping level in the sample.

If a measurement of sample resistance R is made, one can calculate the resistivity

$$R = \frac{\rho}{A}, \text{ so } \rho = \frac{RWT}{L} = \frac{V_x / I_x}{L / WI}. \tag{C2.12}$$

Since the conductivity $\sigma = 1/\rho$ is equal to $q\mu_p p$, the mobility μ_p is just the ratio of the Hall coefficient and the resistivity. Measurements of the Hall coefficient and the resistivity over a range of temperatures yield plots of majority carrier concentration and mobility vs. temperature, very useful data to have for semiconductors.

ACCENT HL5500PC was used in this project for the samples' Hall measurement. It has a simple probe system and can do the measurement at both room temperature and 77K. It can carry on Van der Pauw and Hall Bar measurements to ASTM F-76 standard.